

Copyright
by
Guoliang Liu
2003

The Dissertation Committee for Guoliang Liu
certifies that this is the approved version of the following dissertation:

**Characterization of manganese-oxide perovskites,
exhibiting a colossal magnetoresistance**

Committee:

John B. Goodenough, Supervisor

Dean P. Neikirk

Michael F. Becker

Peter F. Green

Arumugam Manthiram

Jianshi Zhou

**Characterization of manganese-oxide perovskites,
exhibiting a colossal magnetoresistance**

by

GUOLIANG LIU, BS, MS, MSE

DISSERTATION

Presented to the Faculty of the Graduate School of

The University of Texas at Austin

in Partial Fulfillment

of the Requirements

for the Degree of

DOCTOR OF PHILOSOPHY

The University of Texas at Austin

May, 2003

Dedication

To my wife Ruqian

Acknowledgements

There are many people who have helped me to complete this work. I hereby thank all of them. I would like to express my heart-felt gratitude to my supervisor, Prof. John Goodenough, who has instilled the respect in me for the academic life, for his educational and financial support, for his selfless availability even during weekends, and for his wise guidance in my life. He is the source of great encouragement and motivation to me. I wish to extend my appreciation to Dr. Jianshi Zhou for his great help during the course of this work. His example of creative and diligent effort in research often inspires me. I am also indebted to my former supervisor, Prof. Shousheng Yan of Peking University, who initially guided me to conduct research activity. Many thanks also go to my colleagues and friends for their generous assistance. Special thanks are due to my family for their continuous support and patience over the six years to complete this work. I would have achieved nothing without them.

Characterization of manganese-oxide perovskites, exhibiting a colossal magnetoresistance

Publication No. _____

Guoliang Liu, Ph. D.

The University of Texas at Austin, 2003

Supervisor: John B. Goodenough

The complex phase diagrams of the $\text{La}_{1-x}\text{Sr}_x\text{MnO}_3$ ($0 \leq x \leq 0.35$), $\text{La}_{1-x}\text{Ca}_x\text{MnO}_3$ ($0 \leq x \leq 0.40$), and $R_{0.7}A_{0.3}\text{MnO}_3$ ($0.949 \leq t \leq 0.997$) systems, in which R is one or more the trivalent rare earth ions, A is one or two divalent alkaline earth, and t is tolerance factor, are presented; they were mapped out with measurements of resistivity $\rho(T)$, thermoelectric power $\alpha(T)$, specific-heat $C_p(T)$, and magnetization $M(T)$ on a series of melt-grown single-crystal samples. A transition from localized to itinerant behavior of electrons of e -orbital parentage in the presence of a localized t^3 configuration with spin $S = 3/2$ was shown to be characterized by an electronic phase segregation into orbitally ordered, electron-rich antiferromagnetic regions and orbitally disordered, conductive ferromagnetic regions that grow in an applied magnetic field. This two-phase electronic character in the crossover compositions gives rise to spin-glass behavior and a

colossal magnetoresistance. Particular emphasis was placed on the evolution of the specific-heat data $C_p(T)$ on crossing the transition from localized to itinerant electrons and the fact that $C_p(T)$ is suppressed at a spin-glass freezing temperature.

Table of Contents

List of Tables.....	xi
List of Figures	xii
Chapter 1: Introduction	1
1.1 Historical Review	3
1.2 Structural Consideration.....	5
1.2.1 The Tolerance Factor	5
1.2.2 Jahn-Teller Distortion	8
1.2.3 The Virial Theorem.....	9
1.3 Electronic Consideration	10
1.3.1 Ligand-Field	12
1.3.2 Jahn-Teller Distortion	13
1.3.3 Exchange Interactions	14
1.4 Orbital, Spin and charge ordering	18
1.5 CMR Phenomena	22
1.6 Motivation of the work.....	24
Chapter 2 Experimental Techniques	26
2.1 Crystal Growth	26
2.2 Specific-Heat Measurement	30
2.2.1 Specific-Heat Measurement Overview	30
2.2.2 Specific-Heat Measurement Principle.....	34
2.2.3 Specific-Heat Measurement Apparatus.....	37
2.2.4 Specific-Heat Measurement Operation	43
2.2.5 Specific-Heat Measurement Calibration	45
2.3 Resistivity Measurement	47
2.4 Thermoelectric Power Measurement	50
2.5 Magnetic Measurement.....	53

Chapter 3: The $\text{La}_{1-x}\text{Sr}_x\text{MnO}_3$ system	57
3.1 Introduction	59
3.2 Experimental Procedures.....	62
3.3 Resistivity and Thermoelectric Power	66
3.4 Saturation Magnetization at 5 K.....	67
3.5 Specific-Heat $C_p(T)$ and Magnetization $M(T)$	73
3.5.1 Suppressed Entropy Change at Magnetic Transition	74
3.5.2 O' Phase - O^* Phase Transition	75
3.5.3 Transition at T_{JT}	76
3.5.4 O^* Phase - O'' Phase Transition	77
3.5.5 O^* Phase - R Phase Transition	78
3.5.6 Calculated Entropy Change at T_N and T_c	79
3.6 Summary and Conclusion	80
Chapter 4: The $\text{La}_{1-x}\text{Ca}_x\text{MnO}_3$ system	83
4.1 Experimental Procedures.....	83
4.2 Phase Diagram.....	85
4.3 Resistivity, Thermoelectric Power, and Saturation Magnetization	89
4.4 Specific-Heat $C_p(T)$ and Magnetization $M(T)$	94
4.5 Summary	96
Chapter 5: The $\text{R}_{0.7}\text{A}_{0.3}\text{MnO}_3$ system.....	98
5.1 Introduction	98
5.2 Experimental Procedures.....	100
5.3 Phase Diagram.....	104
5.4 Resistivity and Saturation Magnetization	107
5.5 Specific-Heat $C_p(T)$ and Magnetization $M(T)$	113
5.6 Summary	115

Chapter 6: Summary of the Work	116
References	120
Vita	126

List of Tables

Table 5.1:	$\text{R}_{0.7}\text{A}_{0.3}\text{MnO}_3$ Sample Composition and Stoichiometric Mixture ..	100
Table 5.2:	Magnetization at 5 K and 50 kOe in $\text{R}_{0.7}\text{A}_{0.3}\text{MnO}_3$	109

List of Figures

Figure 1.1: CMR at 5 T on cooling for different compositions $0 \leq x \leq 0.6$ in the system $\text{La}_{0.7-x}\text{Pr}_x\text{Ca}_{0.3}\text{MnO}_3$	2
Figure 1.2: Ideal AMO_3 cubic-perovskite structure.....	6
Figure 1.3: Oxygen displacements superimposed on MnO_3 rotations about [110] axis.....	8
Figure 1.4: Schematic energy levels of the octahedral-site Mn^{3+} ion.....	11
Figure 1.5: A schematic illustration of (a) type-A antiferromagnetic ordering, and (b) canted antiferromagnetic ordering.....	19
Figure 1.6: Orbital and magnetic ordering in the (001) planes of the CE phase in $\text{La}_{0.5}\text{Ca}_{0.5}\text{MnO}_3$	21
Figure 2.1: Outline of two ellipsoidal reflectors of the infrared-ray-heating image furnace	27
Figure 2.2: $\text{La}_{0.88}\text{Sr}_{0.12}\text{MnO}_3$ crystal grown by NEC image furnace	28
Figure 2.3: X-ray diffraction of $\text{La}_{0.88}\text{Sr}_{0.12}\text{MnO}_3$ crystal. The highest peak is from the (112) plane.....	29
Figure 2.4: (a) Illustration of ‘pulse’ heating technique (adiabatic calorimetry) (b) AC calorimetry	32
Figure 2.5: Relaxation calorimetry method: heat pulse response of specimen temperature vs time	35
Figure 2.6: Illustration of the core components of the calorimeter	37
Figure 2.7: Picture of the core components of the calorimeter.....	38
Figure 2.8: Illustration of specific-heat measurement head.....	40

Figure 2.9: Specific-heat measurement control block diagram	42
Figure 2.10: (a) Heat pulse response of Fe_3O_4 crystal temperature vs time. (b) Entropy change at Verway transition of Fe_3O_4 crystal	46
Figure 2.11: Specific-heat of Fe_3O_4 crystal	47
Figure 2.12: Current and voltage contacts on specimen in resistivity measurement.....	48
Figure 2.13: Diagram of thermoelectric power apparatus sample stage.....	51
Figure 2.14: Core components and geometry of the Quantum Design MPMS SQUID magnetometer.....	53
Figure 2.15: Samples supporting assembly, superconducting magnet and SQUID amplifier capsules of the MPMS.....	54
Figure 3.1: Phase diagram for $\text{La}_{1-x}\text{Sr}_x\text{MnO}_3$, $0 < x < 0.20$	58
Figure 3.2: Resistivity and thermoelectric power versus temperature for melt-grown samples of $\text{La}_{1-x}\text{Sr}_x\text{MnO}_3$	64
Figure 3.3: Magnetization at 5 K in 50 kOe for $\text{La}_{1-x}\text{Sr}_x\text{MnO}_3$, $0 \leq x \leq 0.35$	67
Figure 3.4: Magnetization $M(T)$ in $H = 20$ Oe and 5 kOe; specific-heat $C_p(T)$ for $\text{La}_{1-x}\text{Sr}_x\text{MnO}_3$	69
Figure 3.5: Entropy change ΔS at T_N , T_c and T_{oo} , or T_c obtained from area of $C_p(T)/T$ after subtraction of background	79
Figure 4.1: Phase diagram of $\text{La}_{1-x}\text{Ca}_x\text{MnO}_3$ system.....	85
Figure 4.2: Resistivity versus temperature for melt-grown samples of the $\text{La}_{1-x}\text{Ca}_x\text{MnO}_3$ system	87

Figure 4.3: Thermoelectric power versus temperature for melt-grown samples of the $\text{La}_{1-x}\text{Ca}_x\text{MnO}_3$ system	88
Figure 4.4: Magnetization at 5 K in 50 kOe for $\text{La}_{1-x}\text{Ca}_x\text{MnO}_3$, $0 \leq x \leq 0.4$	89
Figure 4.5: Magnetization $M(T)$ in $H = 20$ Oe and 5 kOe; specific-heat $C_p(T)$ for $\text{La}_{1-x}\text{Ca}_x\text{MnO}_3$	92
Figure 5.1: Phase diagram of Curie temperature T_c vs tolerance factor for the system $\text{R}_{0.7}\text{A}_{0.3}\text{MnO}_3$	103
Figure 5.2 Resistivity versus temperature for the $\text{R}_{0.7}\text{A}_{0.3}\text{MnO}_3$ system	106
Figure 5.3: Magnetization at 5 K versus applied field for melt-grown samples of the $\text{La}_{0.7}\text{Ca}_{0.3}\text{MnO}_3$, $\text{Pr}_{0.7}\text{Ca}_{0.3}\text{MnO}_3$ and $\text{La}_{0.2}\text{Y}_{0.5}\text{Ca}_{0.3}\text{MnO}_3$	107
Figure 5.4: Magnetization $M(T)$ in $H = 20$ Oe and 5 kOe; specific heat $C_p(T)$	110

Chapter 1: Introduction

Transition-metal oxides have long been research subjects as these materials exhibit a lot of exotic structural, magnetic, and electronic behaviors and demonstrate a wide range of application in industry. Where there is a crossover from localized to itinerant $3d$ electrons, the traditional one-electron band theory is not applicable to explain the properties of materials. The interactions between charge, spin, orbital and lattice play an important role to account for these unusual behaviors. Recently, attention has become focused on the manganese oxides with perovskite structure. Although these materials have been studied for many years, the current enthusiasm was stimulated by the observation of colossal magnetoresistance (CMR) in this family of compounds. The magnetoresistance phenomenon, a variation of the resistivity upon application of a magnetic field, is relevant to several technical areas, such as magnetic data storage, and much of the impetus for the present interest in the manganites comes from the material's potential for the application to electrically-readable magnetic-field sensors. However, the research of this thesis is directed at exploring the CMR phenomena, which occurs at too low a temperature and too high a magnetic field to be of practical interest. Fig. 1.1 from Hwang *et al*^{1,1} shows the remarkable change in ferromagnetic Curie temperature T_c and the intrinsic CMR obtained in an applied field of 5 T for the system $\text{La}_{0.7-x}\text{Pr}_x\text{Ca}_{0.3}\text{MnO}_3$; the maximum CMR occurs at T_c and increases dramatically with decreasing T_c . This intrinsic CMR in the

manganite perovskites is not to be confused with an extrinsic giant magnetoresistance (GMR) of technical interest that is also studied in these perovskites.

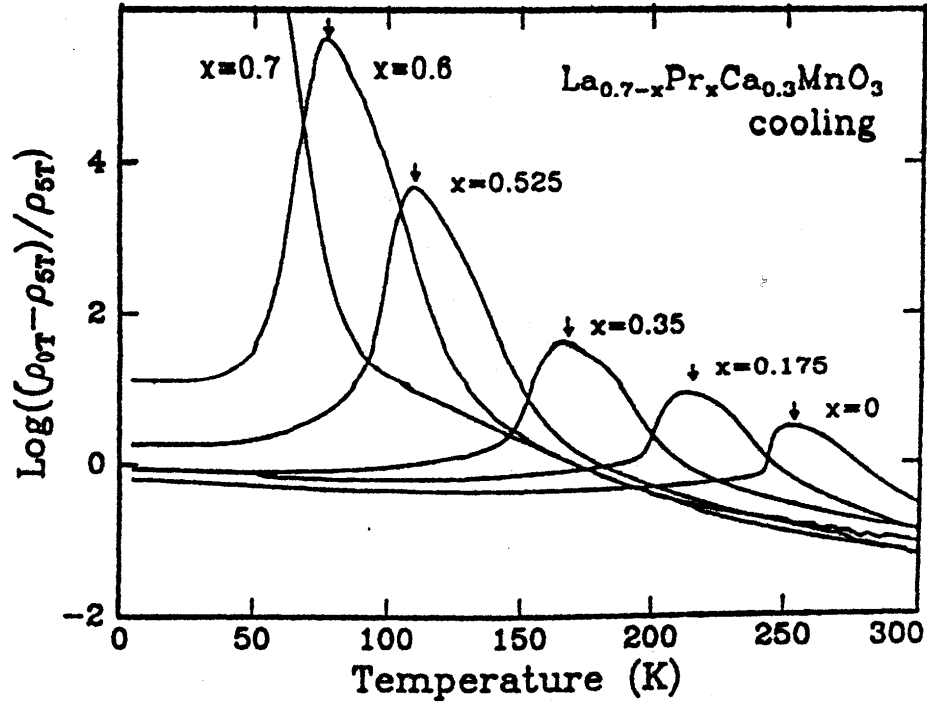


Fig. 1.1: CMR at 5 T on cooling for different compositions $0 \leq x \leq 0.6$ in the system $\text{La}_{0.7-x}\text{Pr}_x\text{Ca}_{0.3}\text{MnO}_3$. The arrows indicate the Curie temperature T_c . [After H. Y. Hwang *et al.*^{1,1} by permission. From Phys. Rev. Lett. **75**, 914-917 (1995). Copyright (1995) by the American Physical Society]]

Whether the manganese oxide perovskites will prove technologically useful is not quite clear at present. But the observation of a colossal magnetoresistance has stimulated a large amount of research work. In these materials, the interaction between the electrons and the lattice is unusually strong,

leading to a wide range of novel physical phenomena, and the interplay can be ‘tuned’ by variation of chemical composition, temperature and magnetic field. These materials therefore provide a good opportunity to study the poorly understood physics of systems with strong electron, magnetic, and lattice coupling.

1.1 HISTORICAL REVIEW

Interest in metallic transition-metal oxides with perovskite-related structures goes back to the 1950s when the sodium tungsten bronzes Na_xWO_3 were shown to be metallic^{1,2} and the system $\text{La}_{1-x}\text{Sr}_x\text{MnO}_3$ was found to contain a ferromagnetic conductive phase.^{1,3} $\text{La}_{0.5}\text{Sr}_{0.5}\text{CoO}_3$ was also reported to be a ferromagnetic metal, but with a peculiar magnetization of $1.5 \mu_B/\text{Co atom}$.^{1,4} In the early 1950s, it was assumed that in the transition-metal oxides, the *d*-state manifolds were localized and the interatomic spin-spin interactions could be described by superexchange perturbation theory.^{1,5} Early neutron-diffraction studies showed an anticipated antiferromagnetic order of the MO_3 array in the insulator LnCrO_3 and LnFeO_3 , where Ln is a lanthanide.^{1,6} However, the anisotropic magnetic order in the so-called A-type antiferromagnet LaMnO_3 and the complex magnetic order found^{1,7} in $\text{La}_{0.5}\text{Ca}_{0.5}\text{MnO}_3$ remained unreported until it was pointed out that cooperative orbital ordering could account for the magnetic order if the superexchange interactions were reexamined^{1,8}; this reexamination led to the first formulation of the rules for the sign of the superexchange interactions that are now known as the Goodenough-Kanamori Rules. These predictions have been fully verified.^{1,9}

The ferromagnetic coupling in conductive $\text{La}_{1-x}\text{Sr}_x\text{MnO}_3$ led to the concept of double exchange, but the original formulation by Zener^{1.10} was restricted to a two-manganese polaron that was assumed to move diffusively without activation energy to give a global ferromagnetism. P-G de Gennes,^{1.11} borrowing a spin-dependent transfer integral from Anderson and Hasegawa,^{1.12} made a more realistic double-exchange model for itinerant electrons in the presence of localized spins. But how itinerant electrons and localized spins from the same d manifold could coexist on an atom was not addressed until some years later,^{1.13} when it was also pointed out that the unusual magnetization of ferromagnetic, metallic $\text{La}_{0.5}\text{Sr}_{0.5}\text{CoO}_3$ could be understood as an intermediate spin state on the cobalt stabilized by itinerant electrons coexisting with a localized spin. Meanwhile, the origin of the metallic conductivity of the Na_xWO_3 bronzes remained puzzling until it was pointed out^{1.14} that strong W-O covalent bonding allowed the W-O-W interactions across a bridging oxygen atom to be strong enough to transform the π -bonding d states from localized configurations into itinerant-electron states. Recognition that the d electrons on the MO_3 array of an AMO_3 perovskite could be either localized or itinerant led to an early mapping of localized versus itinerant electronic behavior in the AMO_3 perovskites.^{1.15}

An extensive re-examination of the oxide perovskites was stimulated in 1986 by the discovery of high-temperature superconductivity in the perovskite-related system $\text{La}_{2-x}\text{Sr}_x\text{CuO}_4$ ^{1.16} and the subsequent observation of a colossal negative magneto-resistance (CMR)^{1.1} in the ferromagnetic system $(\text{La}_{1-y}\text{Pr}_y)_{0.7}\text{Ca}_{0.3}\text{MnO}_3$. High- T_c superconductivity in the layered copper oxides and the

CMR phenomenon in the manganese oxide perovskites both occur at a transition from localized to itinerant electronic behavior. The crossover from localized to itinerant electronic behavior cannot be described by the homogeneous theories of electronic states in solids that existed in 1986. Extensive experimental studies on these and related systems have revealed the presence of dynamic phase segregations at lower temperatures that are associated with strong electron coupling to locally cooperative oxygen displacements. Locally cooperative, dynamic oxygen displacements are not revealed by conventional diffraction experiments; faster, local probes are required to observe them directly. These probes include the pair-density-function analysis of neutron-diffraction data from a synchrotron source as well as Mössbauer, NMR, NQR, and XAFS spectroscopies. Indirect evidence for their existence is provided by transport and magnetic measurements. After the experience of the research fever for superconductive copper oxides (cuprates), there has been much progress in the preparative method of oxide specimens, e.g. growth of single crystals and fabrication of epitaxial thin films, as well as in a comprehensive understanding of the electronic and magnetic properties of such correlated-electron system. This situation has expedited recent research on the perovskite oxides.

1.2 STRUCTURAL CONSIDERATION

1.2.1 The Tolerance Factor

The ideal AMO_3 perovskite has the cubic structure of Fig. 1.2. The AMO_3 cubic-perovskite structure contains A cations in twelvefold and M cations in sixfold oxygen coordination. A measure of the mismatch between the equilibrium

A -O and M -O bond lengths is the deviation from unity of the so-called geometric tolerance factor:^{1,17}

$$t \equiv \langle A-O \rangle / \sqrt{2} \langle M-O \rangle, \quad (1.1)$$

where the average $\langle A-O \rangle$ and $\langle M-O \rangle$ bond lengths are calculated from the sums of ionic radii obtained from X-ray data.

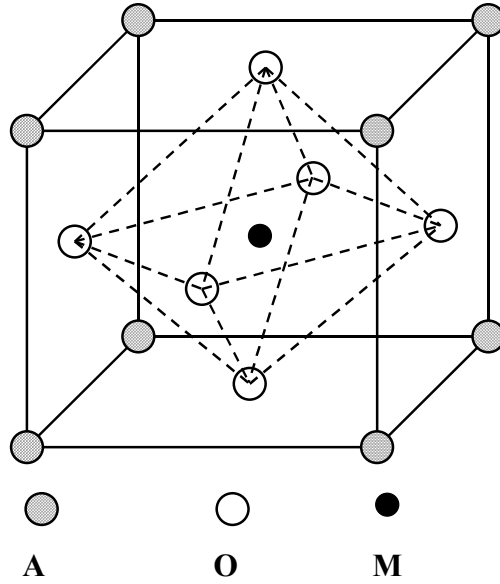


Fig. 1.2:

Ideal AMO_3 cubic-perovskite structure.

Of particular interest in this work are the perovskite-related oxides in which M is a $3d$ -block transition-metal atom and the A -sites are occupied by a lanthanide, yttrium, and/or alkaline earth. The ionic radii are usually obtained from room-temperature, ambient-pressure X-ray data. However, it must be pointed out that the tolerance factor is temperature and pressure dependent. The

thermal expansion of the $\langle A-O \rangle$ bond is greater than that of the $\langle M-O \rangle$ bond, and normally the $\langle A-O \rangle$ bond is also more compressible than the $M-O$ bond, which makes

$$dt/dT > 0 \text{ and } dt/dP < 0. \quad (1.2)$$

However, at a transition from localized to itinerant electronic behavior, an unusually high compressibility of the $\langle M-O \rangle$ bond results in a $dt/dP > 0$.

The AMO_3 structure accommodates a $t > 1$ by the formation of hexagonal polytypes. The principal interest of these structures for the present discussion is the demonstration^{1,18} they provide for $dt/dP < 0$ as the normal behavior where there is no transition from localized to itinerant electronic behavior. This type of structure is not in the scope of this work.

A $t < 1$ places the $\langle M-O \rangle$ bonds under compression and the $\langle A-O \rangle$ bonds under tension. The structure can alleviate the stress by a cooperative rotation of MO_6 octahedra that bends the $M-O-M$ bonds from 180° to $(180^\circ - \phi)$. Cooperative rotations about the cubic $[110]$ axis give orthorhombic symmetry (O phase) with $c/a > \sqrt{2}$, those about $[111]$ axis give rhombohedral symmetry (R phase), and those about the $[001]$ axis give tetragonal symmetry. As t decreases from $t = 1$, these distortions change from tetragonal to rhombohedral and then to orthorhombic. Orthorhombic and rhombohedral distortions are found in the $Ln_{1-x}A_xMnO_3$ perovskites where Ln is a lanthanide and A an alkaline-earth.

1.2.2 Jahn-Teller Distortion

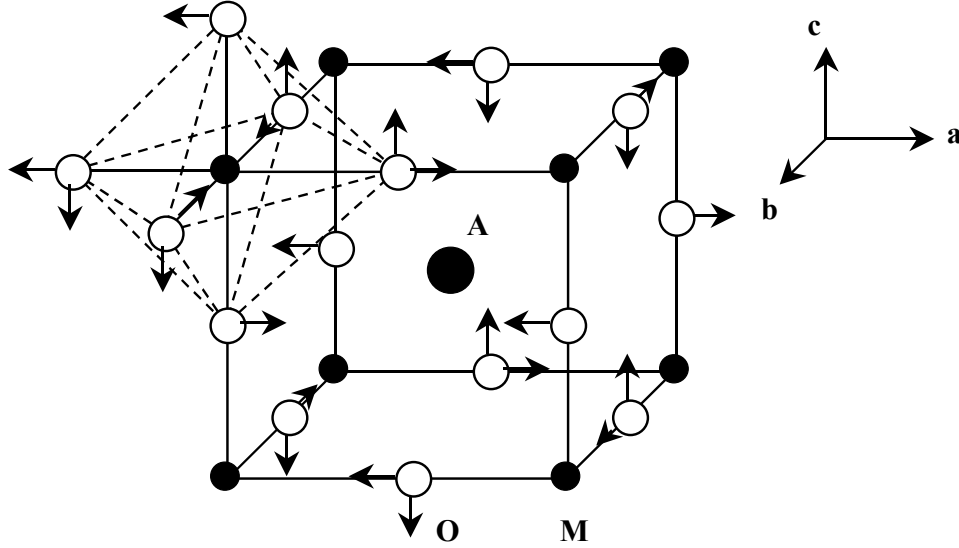


Fig. 1.3: Oxygen displacements superimposed on MnO₃ rotations about [110] axis.

Oxygen displacements away from one near-neighbor *M* atom toward the other may be superimposed on the cooperative rotations. This situation represents a cooperative Jahn-Teller distortion. In LaMnO₃, local, static Jahn-Teller distortions, which remove an orbital degeneracy (see electronic consideration), shift the oxygen in the (001) planes (Fig. 1.3) to change the orthorhombic axial ratio from $c/a > \sqrt{2}$ to $c/a < \sqrt{2}$. In order to distinguish between these two orthorhombic phases, we designate the one with $c/a > \sqrt{2}$ *O*-orthorhombic and the other with $c/a < \sqrt{2}$ *O'*-orthorhombic. Dynamic (short range ordered) Jahn-Teller deformations give an *O** orthorhombic phase with $c/a \approx \sqrt{2}$.

Where cooperative oxygen displacements are static with long-range order, they may be observed directly with a diffraction experiment; but where they are dynamic and without long-range order, direct characterization requires a fast probe. Strong electron coupling due to cooperative oxygen displacements in the $\text{Ln}_{1-x}\text{A}_x\text{MnO}_3$ perovskites is manifest in a competition between three situations: (1) static displacements with long-range charge and orbital order, (2) dynamic displacements with only short-range order, and (3) itinerant-electron behavior with Boltzman scattering of electrons from phonons. We will see below the factors that shift this competition with changes in temperature, doping, and tolerance factor at fixed doping concentration.

1.2.3 The Virial Theorem

If the volume occupied by the electrons increases discontinuously on passing from localized to itinerant behavior, then the mean kinetic energy $\langle T \rangle$ of the electrons decreases discontinuously. According to the virial theorem for central-force fields, which states

$$2\langle T \rangle + \langle V \rangle = 0 \quad (1.3),$$

the magnitude of the mean potential energy $|\langle V \rangle|$ must then also decrease discontinuously. For anti-bonding electrons, a decrease in $|\langle V \rangle|$ is achieved by a decrease in the mean equilibrium $\langle M-O \rangle$ bond length; and if the change in $\langle T \rangle$ and $\langle M-O \rangle$ is discontinuous, the transition is first-order. At such a first order phase change, the equilibrium $\langle M-O \rangle$ bond length is described by a double-well

potential and the localized-electron equilibrium bond length is larger than that for the itinerant electrons. A double-well bond potential has two consequences: (1) the coexistence of two phases gives an anomalously large compressibility of the $\langle M-O \rangle$ bond that is manifest in a $dt/dP > 0$ and (2) a segregation into an itinerant-electron phase and a localized-electron phase can be expected at crossover. A $dt/dP > 0$ value is found at the $O'-O$ transition and phase segregation into a Mn^{4+} -rich, conductive, and orbitally disordered phase imbedded in a Mn^{4+} -poor phase is associated with the CMR phenomenon. The Mn^{4+} -rich phase has a higher T_c than the Néel temperature T_N of the orbitally ordered Mn^{4+} -poor phase. In an applied magnetic field at temperatures below T_c of the ferromagnetic phase, the ferromagnetic phase grows at the expense of the paramagnetic phase, which becomes ferromagnetic and conductive when the $Mn^{3+} e$ orbitals become disordered.

1.3 ELECTRONIC CONSIDERATION

The Mn atoms occupy octahedral sites in the $Ln_{1-x}A_xMnO_3$ perovskites. They are surrounded by 6-oxygen ions O^{2-} . The $3d$ orbitals on the Mn-site placed in such an octahedral coordination are subject to the lifting of the degeneracy by the crystal field. The crystal field splits the five $3d$ orbitals into a t_{2g} triplet and an e_g doublet (Fig. 1.4). The t_{2g} levels lie 2~4 eV below the e_g levels. If the e_g level is singly occupied ($x = 0$), a Jahn-Teller distortion may occur, which would split the e_g doublet by an energy of Δ_{JT} . All the $3d$ electrons are subject to Coulomb repulsive electron-electron interactions. The on-site Coulomb repulsion at a manganese atom in an oxide is strong enough that no d orbital is occupied by

more than one electron and all the electron spins on a given Mn are ferromagnetically aligned by a large Hunds-rule coupling. Thus in the Mn^{3+} - based compounds such as LaMnO_3 , 3 of the 4 d electrons fill up the t_{2g} levels, forming a localized electron core with spin S_t of magnitude $3/2$, while the remaining 1 electron goes into a two fold degenerate pair of e_g orbitals, showing the electronic configuration of $t_{2g}^3 e_g^1$ (total spin number $S = 2$). The e_g orbital electron, although hybridized strongly with O-2 p orbitals, is localized in the parent all- Mn^{3+} -based compound LaMnO_3 , which is a so-called Mott insulator. However, the e_g electrons can be made itinerant by oxidation of the MnO_3 array. Substitution of an alkaline earth atom A^{2+} for La^{3+} in $\text{La}_{1-x}\text{A}_x\text{MnO}_3$ oxidizes the MnO_3 array. The t_{2g} electrons, less hybridized with the O-2 p orbitals, remains localized even in metallic state.

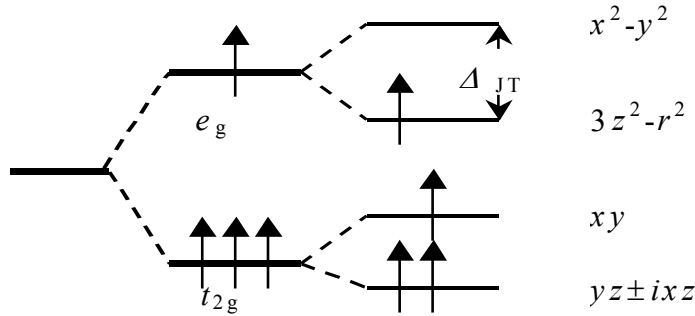


Fig. 1.4: Schematic energy levels of the octahedral-site Mn^{3+} ion. It shows the low-lying t_{2g} levels occupied by three parallel-spin electrons forming a $S_t = 3/2$ core, and high-lying e_g doublet. The right portion of the figure shows that if the e_g level is singly occupied, a Jahn-Teller distortion may occur, which would split the e_g doublet by an energy of Δ_{JT} , thereby stabilizing the electronic energy.

In order to understand the transition from localized to itinerant electronic behavior, we begin with the construction of ligand-field $3d$ orbitals and then consider the nature of the interactions between localized ligand field configurations on neighboring Mn cations.

1.3.1 Ligand-Field

In $\text{Ln}_{1-x}\text{A}_x\text{MnO}_3$ perovskites, the Mn-O covalent bonding is introduced into localized d -electron wavefunctions in second-order perturbation theory. In cubic symmetry, the resulting ligand-field wavefunctions are

$$\psi_t = N_\pi(f_t - \lambda_\pi \phi_\pi), \quad (1.4)$$

$$\psi_e = N_\sigma(f_e - \lambda_s \phi_s - \lambda_\sigma \phi_\sigma), \quad (1.5)$$

where the covalent-mixing parameters $\lambda_\sigma \equiv (f_e, H'\phi_\sigma)/\Delta E_p$, $\lambda_\pi \equiv (f_t, H'\phi_\pi)/\Delta E_p$, and $\lambda_s \equiv (f_e, H'\phi_s)/\Delta E_s$, where ΔE_p and ΔE_s are the energies between empty d state and the p or s states, respectively, of the oxygen ions. The threefold-degenerate xy , $yz \pm izx$ atomic orbitals f_t only bond with oxygen $2p_\pi$ orbitals, and ϕ_π is a linear combination of nearest-neighbor oxygen $2p_\pi$ orbitals having the same symmetry as f_t . The ΔE_π in λ_π is the energy required to excite a $2p_\pi$ electron from the oxide ion to an empty f_t orbital. The twofold-degenerate x^2-y^2 , $3z^2-r^2$ atomic orbitals f_e bond with the oxygen $2p_\sigma$ and $2s$ orbitals. An overlap integral $(f_e, \phi_\sigma) > (f_t, \phi_\pi)$ makes $\lambda_\sigma > \lambda_\pi$. Covalent bonding gives the principal contribution to the cubic-field splitting of the ψ_t and ψ_e energy, which is

$$\Delta_c = \Delta \varepsilon_\sigma - \Delta \varepsilon_\pi = \Delta_M + (\lambda_\sigma^2 - \lambda_\pi^2) \Delta E_p + \lambda_s^2 \Delta E_s \quad (1.6)$$

where Δ_M is a purely electrostatic energy that is small and of uncertain sign due to the penetration of the O^{2-} ion electron cloud by the cation wavefunctions. The difference in the strengths of the covalent mixing raises the energy of the antibonding e orbitals more than that of the t orbitals. Historically, the electrons of the corresponding threefold-degenerate state are designed t_{2g} and the electrons of the corresponding twofold degenerate state are designed e_g (Mulliken).

For a Mn^{3+} ion in an oxide, Hund's highest multiplicity rule is preserved. With four d -electrons, Mn^{3+} adopts a high-spin configuration with three unpaired electrons in the t_{2g} orbitals and a single electron in the degenerate, antibonding e_g orbitals. The localized $3d^4$ configuration at a high-spin Mn^{3+} ion is $t_{2g}^3 e_g^1$ and that at Mn^{4+} ion is $t_{2g}^3 e_g^0$.

1.3.2 Jahn-Teller Distortion

In $LaMnO_3$, the e_g electrons of the $Mn^{3+}: t_{2g}^3 e_g^1$ configurations are localized. An undistorted octahedral site would leave the single e electron with a twofold orbital degeneracy, which is unstable to a distortion by O^{2-} displacement along a vibronic coordinate that lifts the orbital degeneracy, a Jahn-Teller distortion. Mn^{4+} is Jahn-teller inactive as it has no such unpaired e_g electron. A local distortion of the octahedral site to tetragonal or orthorhombic symmetry removes the orbital degeneracy by the energy Δ_{JT} while preserving the total orbital energy; the e_g -electron energy is stabilized linearly with the cooperative

oxygen displacement. The local site distortion costs an elastic energy that varies as the square of the oxygen displacement. The cost in elastic energy is minimized if the local distortions of the individual MnO_6 octahedra are long-range cooperative, which makes possible a distortion from the O -orthorhombic to the O' -orthorhombic structure as mentioned in the section on structural considerations. In the O' phase, a ratio $c/a < \sqrt{2}$ signals a cooperative ordering of the antibonding e_g electrons into orbitals of the long O-Mn-O bonds in the (001) planes; the e_g orbitals of the short O-Mn-O bonds are empty. The Jahn-Teller distortion plays a key role in determining the magnetic order in LaMnO_3 .

1.3.3 Exchange Interactions

The ligand-field wavefunctions ψ_t and ψ_e include only the Mn-O interactions; to these we must add the interactions between ligand-field states on neighboring cations. Of particular interest are the spin-spin interactions between localized spins on neighboring cations; and in the MnO_3 array, the strongest of these are the Mn-O-Mn interactions. We neglect the much weaker next near-neighbor Mn-Mn interactions across a cube face.

There are four types of spin-spin interaction: (1) ferromagnetic direct exchange between electrons in orthogonal orbitals; (2) a bonding superexchange interaction involving a virtual electron transfer; (3) a bonding double-exchange interaction involving a real electron transfer; and (4) an indirect exchange between localized spins via a direct exchange with itinerant electrons.

Direct exchange is ferromagnetic; it occurs between spins in orthogonal orbitals. It is a potential exchange as it does not involve electron transfer. For

example, the lifting of the atomic spin degeneracy by an energy Δ_{ex} is due to an intraatomic direct exchange interaction that produces the effective Hund atomic magnetic-exchange field. The five $3d$ orbitals of a free Mn atom are degenerate, but with five electrons or holes in the $3d$ manifold, the spin degeneracy is removed by the ferromagnetic direct-exchange interactions between electron spins in orthogonal atomic orbitals. These exchange interactions produce the Hund intraatomic exchange field H_{ex} . The energy splitting between a high and lower localized spin state will be designated Δ_{ex} . The intraatomic direct exchange responsible for Hund's highest multiplicity rule is ferromagnetic.

Superexchange is a kinetic exchange that involves a virtual charge transfer. Superexchange specifically applied to manganite perovskites describes not only the spin-spin interactions between the orbitally non-degenerate, localized t_{2g}^3 configuration, but also the interactions via localized e_g electrons. In both Mn^{3+} and Mn^{4+} , 3 electrons fill the t_{2g} orbitals, forming an inert core spin S_t with magnitude of $3/2$. The t_{2g}^3 configurations are localized and half-filled for all values of x in $\text{Ln}_{1-x}\text{A}_x\text{MnO}_3$ perovskites, so the electron transfer of the t_{2g} electron at R_i is to an empty t_{2g} orbital at R_j having a spin opposite to the localized spin R_i , forming a virtual charge transfer $t_{2g}^3\text{-O:}2p_{\pi}\text{-}t_{2g}^3 = t_{2g}^2\text{-O:}2p_{\pi}\text{-}t_{2g}^4$. The spin of the electron transferred from Mn_i is in the same direction as the localized spin \mathbf{S}_i at Mn_i , and the spin angular momentum is preserved in the transfer. Since the Pauli exclusion principle requires that the empty orbitals at Mn_j are anti-parallel to \mathbf{S}_j , only electrons having a component of their spin anti-parallel to \mathbf{S}_j are transferred to Mn_j . In this case, the super-exchange interaction is anti-ferromagnetic. It

applies to $\text{Mn}^{3+}\text{-O-Mn}^{3+}$, $\text{Mn}^{4+}\text{-O-Mn}^{4+}$, and $\text{Mn}^{3+}\text{-O-Mn}^{4+}$ $t_{2g}^3\text{-O-}t_{2g}^3$ interactions. The e_g -orbital degeneracy at a $\text{Mn}^{3+}:t_{2g}^3e_g^1$ ion allows transfer of an e_g electron from a Mn^{3+} ion at R_i to an empty e_g orbital of Mn^{3+} ion at R_j having either spin direction, but the one with the same spin direction is more stable due to the intraatomic direct exchange. However, such a ferromagnetic electron transfer requires that the e_g orbital at Mn_i be occupied and that at Mn_j be empty, which implies a displacement of the oxygen atom away from Mn_i toward Mn_j . As is illustrated in Fig. 1.3, the cooperative Jahn-Teller distortion in LaMnO_3 provides such a static displacement within every Mn-O-Mn bond of a (001) plane. In this case, electron transfer is not constrained by the Pauli exclusion principle, but the Hund field favors transfer of spin parallel to \mathbf{S}_j , which means the interaction is ferromagnetic.

Double-exchange, on the other hand, involves a real electron transfer from a filled e_g orbital on a Mn^{3+} ion to an empty one in a Mn^{4+} ion and thus is not constrained by the Pauli exclusion principle. Therefore, it is ferromagnetic because a strong intraatomic exchange favors an electron transfer where the spin of the transferred electron is parallel to the core spin ($S_t = 3/2$) of both the donor and the acceptor atoms. Electron transfer is from an occupied e_g state at a Mn^{3+} ion at position R_i to an overlapping empty orbital at an Mn^{4+} ions at R_j . The electron transfer is described by the electron transfer integral. In the presence of localized spins $S_t = 3/2$ from the t_{2g}^3 , the electron transfer integral of the tight-binding band theory is spin-dependent (Anderson and Hasegawa 1955):^{1,12}

$$t_{ij} = b_{ij} \cos(\theta_{ij}/2), \quad (1.7)$$

where θ_{ij} is the angle between spins on Mn_i and Mn_j and $b_{ij} \equiv (\psi_i, H' \psi_j)$ is the spin-independent electron-transfer energy integral. ψ_i and ψ_j are ligand-field wavefunctions and H' describes the perturbation of the potential at R_j caused by the presence of a Mn atom at R_i . Namely, the amplitude of the electron transfer integral depends on the angle θ_{ij} between the neighboring Mn spins. The ferromagnetic interaction via the exchange of the conduction electron whose spin shows the on-site coupling with the local spin is called “double-exchange interaction”. This terminology comes from the fact that the double-exchange process first proposed by Zener, who introduced a double electron transfer, one electron from the bridging oxygen to the Mn^{4+} ion and one electron from the Mn^{3+} ion to the bridging oxygen.

Double-exchange looks similar to the ferromagnetic superexchange case. However, the double-exchange involves a real charge transfer while superexchange involves a virtual charge transfer. If the electron transfer requires an excitation energy, the transfer is virtual. If no energy is required for transfer, the electron transfer is real. Real charge transfer may occur in a mixed-valence system or where the electrons are itinerant. The transition from localized to itinerant electronic behavior occurs where the inter-atomic interactions become greater than the intraatomic interactions. A measure of the strength of the inter-atomic interactions is the bandwidth W and of the strength of the intraatomic interactions is the U_{eff} , which is the effective energy required to add an electron to

a d^n manifold to make it d^{n+1} . The transition from localized to itinerant electronic behavior occurs where $W \approx U_{\text{eff}}$. In the Mn^{3+} compound LaMnO_3 , only superexchange interaction exists between e_g orbitals at neighboring cations; by chemically doping charge carriers into LaMnO_3 (e.g. replacing La with Sr or Ca), one can change the bandwidth W as well as the intraatomic interaction U_{eff} . The stronger the covalent mixing, the weaker the intraatomic interactions. Thus the localized electrons progressively become itinerant electrons. The interactions change from superexchange to an admixture of superexchange and double-exchange, the double-exchange changing from Zener exchange within two-manganese clusters to de Gennes double-exchange between itinerant electrons of e -orbital parentage and localized $S_i = 3/2$ spins.

1.4 ORBITAL, SPIN AND CHARGE ORDERING

So far we have discussed the crystal structure, electronic structure, and rules of the spin-spin interactions in the manganese oxide $\text{Ln}_{1-x}\text{A}_x\text{MnO}_3$ perovskites. The strong coupling of charge, spin, and lattice in this system leads to a wide range of novel magnetic, transport, and charge ordering phenomena. In this section, we discuss the orbital, charge, and spin ordering phenomena, giving examples of undoped LaMnO_3 and $\text{La}_{0.5}\text{Ca}_{0.5}\text{MnO}_3$, which illustrate the broad features caused by the coupling and provide clues as to what might occur at other doping levels.

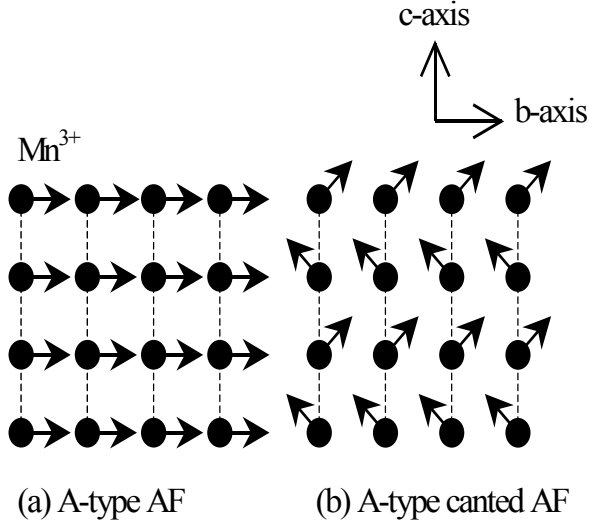


Fig. 1.5: A schematic illustration of (a) type-A antiferromagnetic ordering, and (b) canted antiferromagnetic ordering.

In 1955, on the basis of neutron data by Wollan and Koehler showing ferromagnetic a - b planes coupled anti-parallel to one another along the c -axis (Type A anti-ferromagnetic order, Fig. 1.5(a)) and an orthorhombic axial ratio $c/a < \sqrt{2}$ in LaMnO_3 , Goodenough predicted an orbital ordering by cooperative oxygen-atom displacements within the a - b planes that create long $\text{O}\dots\text{Mn}\dots\text{O}$ bonds alternating with short O-Mn-O bonds (Jahn-Teller distortion, Fig. 1.3). Such a distortion would create $e_g^1 \dots \text{O}:2p_\sigma - e_g^0$ superexchange interactions that are ferromagnetic within the (001) planes. Since the σ -bond interactions are stronger than the π -bond interactions, the ferromagnetic coupling dominates the anti-ferromagnetic $t_{2g}^3 - \text{O}:2p_\pi - t_{2g}^3$ interactions in the a - b planes; but there is no ferromagnetic interaction along the c -axis. This observation resulted in the first formulation of the Goodenough-Kanamori rules for the sign of the superexchange interaction. In that paper, Goodenough^{1,8} also pointed out that an axial ratio $c/a < \sqrt{2}$ was a signature of the presence of static Jahn-Teller orbital

ordering; the O' -orthorhombic $c/a < \sqrt{2}$ was therefore distinguished from the O -orthorhombic $c/a > \sqrt{2}$ distortion. Since the c -axis oxygen atoms share covalent bonding equally on opposite sides whereas the basal-plane oxygens do not, the c -axis Mn-O bond length is intermediate between the short and long bond lengths in the a - b planes; however, it remains closer in length to the short bond to give the O' axial ratio $c/a < \sqrt{2}$. Recent neutron^{1,19} and X-ray^{1,20} diffraction experiments on LaMnO_3 have fully corroborated these predictions. However, a Dzialoshinskii antisymmetric exchange interaction^{1,21} cants the spins by a few degree to give a small ferromagnetic component parallel to the c -axis.

Upon doping charge carriers into the system, the mechanism of spin-ordering changes from anti-ferromagnetic to ferromagnetic as double-exchange plays a more prominent role in the coupling between ferromagnetic MnO_2 sheets. Goodenough and deGennes predicted that, with increasing doping, double exchange would first give rise to canted-spin magnetic structures. In fact, Kawano *et al*.²² have recently shown that the doping of e_g charge carriers into the $\text{La}_{1-x}\text{Sr}_x\text{MnO}_3$ system results in a progressive increase in the spin canting illustrated in Fig. 1.5(b). However, the transition from canted-spin antiferromagnetic order to ferromagnetism is not second order because the transition from localized e_g to itinerant electrons is first order.

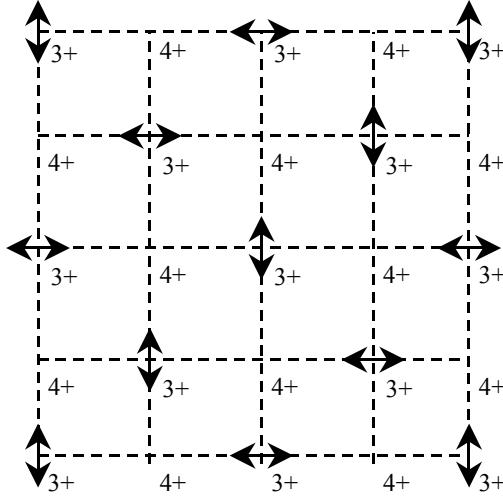


Fig. 1.6:

Orbital and magnetic ordering in the (001) planes in $\text{La}_{0.5}\text{Ca}_{0.5}\text{MnO}_3$. 3+ denotes Mn^{3+} and 4+ denotes Mn^{4+} . Double-end arrows show the direction of e_g orbitals of Mn^{3+} .

The fifty percent doping concentration in the perovskites $\text{La}_{0.5}\text{Ca}_{0.5}\text{MnO}_3$ is particularly interesting because there are formally equal numbers of Mn^{3+} and Mn^{4+} ions in the lattice. This situation can give rise to charge ordering along with a coincident orbital ordering. It is important to point out that other compositions can also exhibit charge and/or orbital ordering, e.g. $\text{Pr}_{0.7}\text{Ca}_{0.3}\text{MnO}_3$, depending on A -site radius, so that these phenomena are not dependent on a ratio of $\text{Mn}^{3+}/\text{Mn}^{4+} = 1$. However, this composition offers the most straightforward picture of orbital ordering and charge ordering. With an equal number of Mn^{3+} and Mn^{4+} ions, the lattice is made up of equal numbers of Jahn-Teller active (Mn^{3+}) and Jahn-Teller inactive (Mn^{4+}) ions. Goodenough hypothesized that such a situation would lead to an ordering of the e_g orbitals on Mn^{3+} to form zig-zag ferromagnetic chains antiparallel to one another in the (001) plane (Fig. 1.6). This structure has been confirmed recently for $\text{La}_{0.5}\text{Ca}_{0.5}\text{MnO}_3$ by Radaelli *et al*^{1,23} using combined neutron and synchrotron x-ray diffraction.

Mixed-valent manganites with localized e_g electrons are typically disordered compounds with Mn^{3+} and Mn^{4+} cations randomly distributed over the lattice. However, under certain chemical and temperature conditions, and especially when Mn^{3+} and Mn^{4+} cations are present in equal amounts, these cations order coherently over long distances to form a charge-ordered (CO) lattice. The Jahn-Teller distortion associated with Mn^{3+} cations also results in orbital ordering in these compounds and the Mn-spins order to form an anti-ferromagnet. It is found that the CO-state can readily be “melted”: the application of a magnetic field, or exposure to X-ray photons can destroy the CO state in favor of a ferromagnetic conductive state. The first direct evidence of charge ordering in $\text{La}_{0.5}\text{Ca}_{0.5}\text{MnO}_3$ was provided by electron diffraction studies reported by Chen and Cheong.^{1,24, 1.25}

1.5 CMR PHENOMENA

The manganese-oxide perovskites $\text{Ln}_{1-x}\text{A}_x\text{MnO}_3$ have been studied extensively and intensively because they exhibit an intrinsic colossal magneto-resistance (CMR) at and above a ferromagnetic Curie temperature T_c (Fig. 1.1) as well as an extrinsic giant magneto-resistance (GMR) associated with tunneling of electron spins across grain boundaries below T_c . Here we consider only the intrinsic phenomenon.

The double-exchange interaction supports the CMR phenomenon. As discussed above, the electron transfer integral $t_{ij} = b_{ij} \cos(\theta_{ij}/2)$ of the tight-binding band theory is spin-dependent. Namely, the amplitude of the electron transfer integral depends on the angle θ_{ij} between the neighboring Mn spins. The

ferromagnetic conductive state below T_c as well as the large magnetoresistance effect near T_c emerges from this fact. Holes in the $\text{Mn}^{4+}/\text{Mn}^{3+}$ complex allow the e_g electron to hop or tunnel depending on the relative angle θ_{ij} between the local spins. The ferromagnetic metallic state is stabilized by maximizing the kinetic energy of the conduction electrons ($\theta_{ij} = 0$). When the temperature is raised up to above T_c , the spin configuration is dynamically disordered and accordingly the effective hopping interaction is reduced on average. Therefore, a MR can be expected around T_c since the local spins are relatively easily aligned by an external field and hence the randomness of the e_g hopping interaction is reduced. This simplest explanation of the MR observed for the manganite above T_c in terms of the double-exchange (DE) is not adequate to describe a CMR.

The physics of the colossal magneto-resistance (CMR) is obviously more complex. Some other important factors than the above simplest DE scenario must be introduced to interpret important features observed experimentally; an antiferromagnetic to ferromagnetic transition at an orbital order-disorder transition in a magnetic field and phase segregation at a crossover from localized to itinerant e_g electrons improve on the simpler version of the double-exchange ideas. A large body of experimental evidence has accumulated that suggests the existence of charge inhomogeneities in manganese oxides either in macroscopic form or, more often, in the form of small clusters of one phase embedded into another.^{1,26} Where a hole-rich, conductive, and orbitally disordered ferromagnetic phase is surrounded by an orbitally ordered, paramagnetic insulator matrix, the

ferromagnetic clusters grow in a magnetic field to beyond percolation, to give the CMR phenomenon.

1.6 MOTIVATION OF THE WORK

The motivation of the work of this thesis comes from a former post-doc researcher in our group Neil Overend's early specific-heat (C_p) measurement on $(\text{La}_{1-x}\text{Nd}_x)_{0.7}\text{Ca}_{0.3}\text{MnO}_3$; he found that the lambda anomaly associating with the ferromagnetic transition disappears at $x = 0.55$.^{1,17} The magnetization measurement made in a modest magnetic field shows that there is a paramagnetic to ferromagnetic phase transition at a Curie temperature T_c in the compound $(\text{La}_{0.45}\text{Nd}_{0.55})_{0.7}\text{Ca}_{0.3}\text{MnO}_3$, so the C_p vs. temperature curve should show a hump at T_c that reflects the entropy change, as was found for the other compositions. However, the specific-heat, measured in zero magnetic field, shows there is no hump at T_c . Why is that? To address this question, it was first necessary to confirm this phenomenon experimentally. Neil measured ceramic samples. It is possible that poor thermal conductivity across the grain boundaries of the ceramic samples could affect the specific-heat measurement. Since the image furnace facility was available, it was possible to grow a series of single crystals to sweep the interested region on the phase diagram with small doping steps. Secondly, does this phenomenon also occur in other manganite compounds? Since high quality $\text{La}_{1-x}\text{Sr}_x\text{MnO}_3$ single crystals could be grown and a lot of research work on $\text{La}_{1-x}\text{Sr}_x\text{MnO}_3$ was available to correlate with specific-heat measurements, the system $\text{La}_{1-x}\text{Sr}_x\text{MnO}_3$ ($0 \leq x \leq 0.35$) was chosen. Crystals of $\text{La}_{1-x}\text{Sr}_x\text{MnO}_3$ ($0 \leq x \leq 0.35$) were grown by the floating-zone method in an IR-radiation image furnace.

The single crystals usually have smaller size and mass compared with ceramic compounds. To measure the specific-heat of a single crystal, the measurement system was re-designed. The resistivity, thermoelectric power, and magnetization were also measured. In order to see if the suppressed $Cp(T)$ at Curie temperature T_c is universal in CMR materials and to further understand the origin of this phenomena, we also studied the similar $\text{La}_{1-x}\text{Ca}_x\text{MnO}_3$ system and a system with fixed doping, but different tolerance factors.

Chapter 2: Experimental Techniques

In this chapter, a description of the experimental method used in the course of this work will be given. We start from crystal growth; after that we focus on the detailed description of the specific-heat measurement, which is the main part of this chapter. Finally, we present a cursory review of the standard methods for measuring resistivity, thermoelectric power, and magnetization with a SQUID magnet meter.

2.1 CRYSTAL GROWTH

In this work, crystals were grown by the floating-zone method in a NEC infrared-ray-heating image furnace. The furnace has two ellipsoidal reflectors that share a common focal point (Fig. 2.1). At the other focal point of each ellipsoidal reflector, there is a Halogen lamp. The light from the Halogen lamp is reflected by the inner surface of the ellipsoidal sphere and then focused at the common focal point. A seed material rod and a feed material rod are placed in a quartz tube. The gap between the two rods is just placed at the common focal point where the temperature can be as high as 3000 °C, depending on the voltage level applied on the two Halogen lamps. When growing, the two material rods rotate in opposite direction and move synchronously downwards. The material (usually a ceramic) melts at the focal point; the melt becomes solid after moving out of the high-temperature zone. The whole molten zone is shielded by a quartz tube; thus crystals can grow in different atmospheres. The crystal-growth status can be

monitored on a small screen through a lens. This floating-zone method, which makes crucibles unnecessary and prevents contamination from impurities, ensures production of highly pure single crystals.

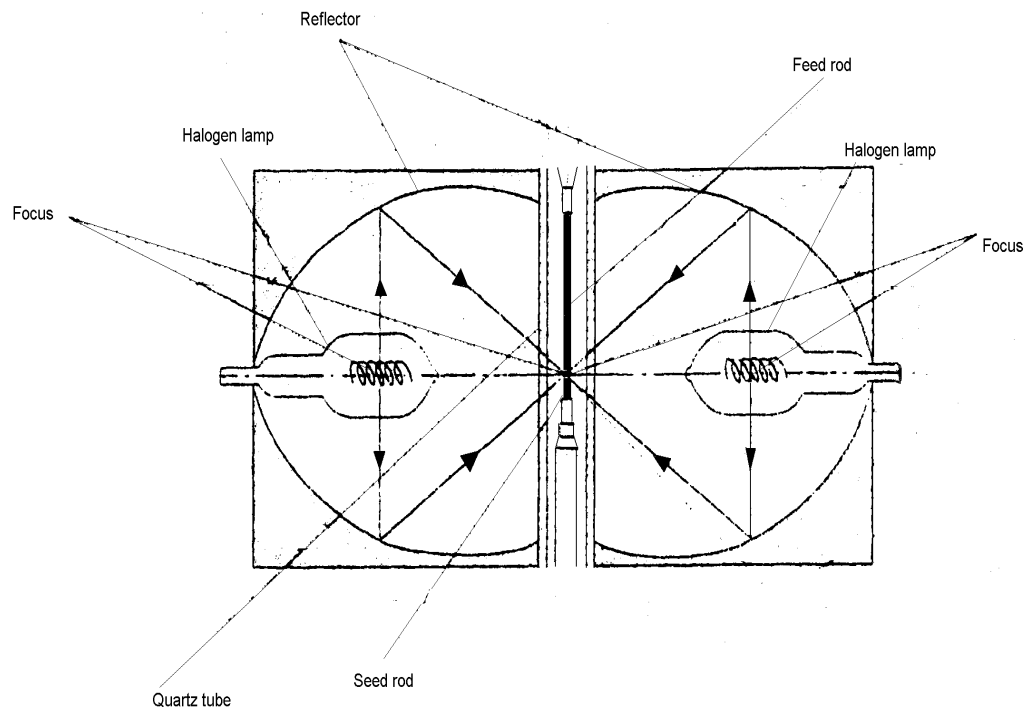


Fig. 2.1: Outline of two ellipsoidal reflectors of the infrared-ray-heating image furnace.

The main parts of the furnace (the two ellipsoidal reflectors, the quartz tube, and the material rod holders) are in a frame. Besides this frame, there is another frame that holds the control system, including a personal computer. The position, the rotation speed, and the feeding speed of the material rods are all

adjustable. The intensity of the Halogen lamp can be programmed in order to control the temperature of the molten zone. A water pump and reservoir are needed to circulate water for cooling the furnace.

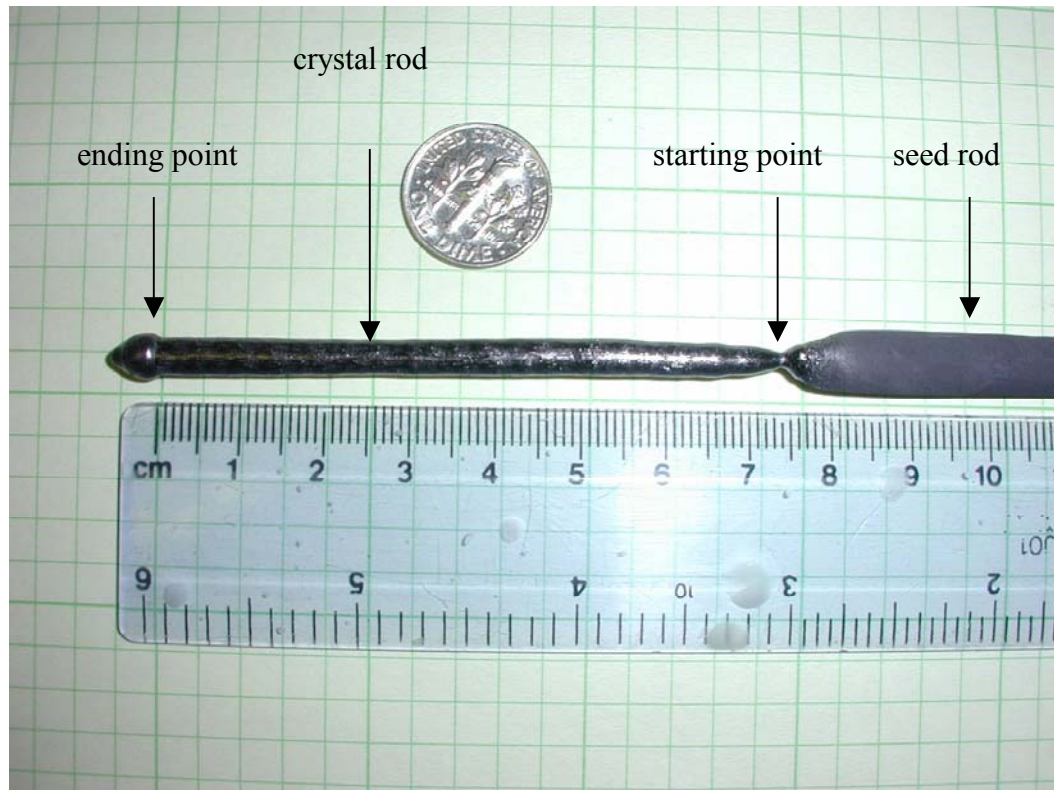


Fig. 2.2: $\text{La}_{0.88}\text{Sr}_{0.12}\text{MnO}_3$ crystal grown by NEC image furnace.

Polycrystalline feed/seed rods of $\text{La}_{1-x}\text{Sr}_x\text{MnO}_3$ (LSMO) were prepared from a stoichiometric mixture of La_2O_3 , SrCO_3 , and Mn_2O_3 that had been calcined three times at 1050°C with inter-anneal grinding. The resulting powder was pressed into a rod and sintered at 1350°C for 24 hours. During the growth, Argon (Ar), air, or oxygen is flowing in the quartz tube in which the crystals are

growing. The atmosphere depends on the composition of the materials. For the LSMO system, crystals with $0 < x < 0.1$ were grown in Ar; those with $x > 0.1$ were grown in flowing air. This process has been shown to yield oxygen-stoichiometric crystals close to the nominal composition. The melt-grown rods tend to contain numerous large crystals, but independent measurements on single-crystal specimens show no difference in the temperature dependence of the resistivity in different crystallographic directions, only a small difference in magnitude.

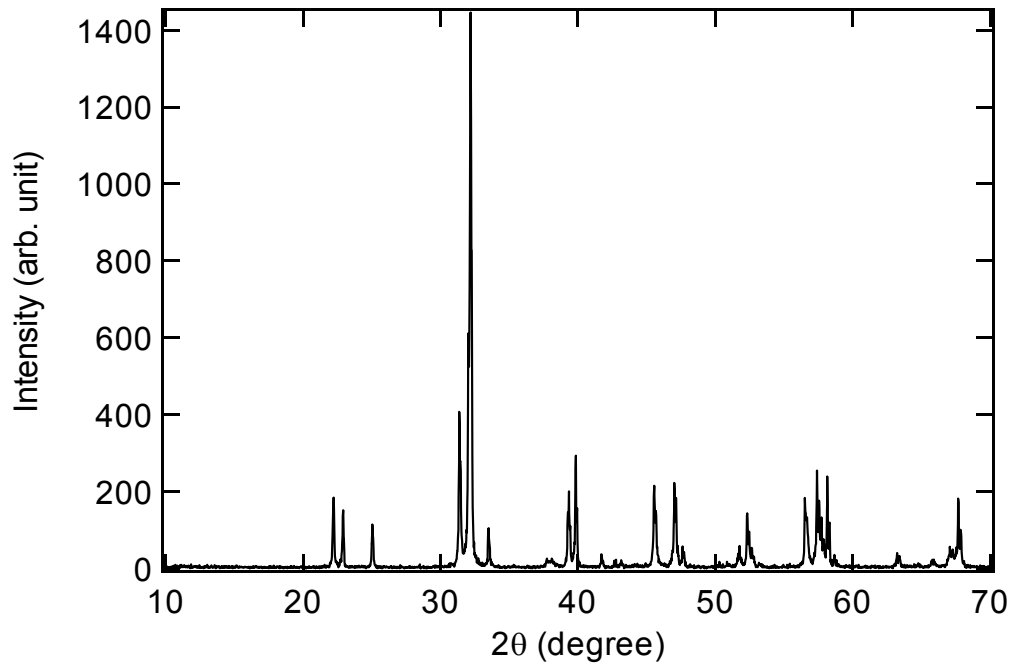


Fig. 2.3: X-ray diffraction of $\text{La}_{0.88}\text{Sr}_{0.12}\text{MnO}_3$ crystal. The highest peak is from the (112) plane.

The Fig. 2.2 shows a $\text{La}_{0.88}\text{Sr}_{0.12}\text{MnO}_3$ crystal bar. It is about 7 centimeter long with good quality. X-ray diffraction shows that the diffraction peak is very sharp (Fig. 2.3) and the crystal has the perovskite structure.

2.2 SPECIFIC-HEAT MEASUREMENT

2.2.1 Specific-Heat Measurement Overview

Before we start to describe details of the specific-heat C_p measurement system, let us have a review of the C_p measurement principles. Specific-heat measurements reveal much information about the electronic properties of materials, for example, the density of states at the Fermi level; about the lattice or vibronic properties of a solid; about phase transitions, in particular, the entropy change associated with that phase transition.^{2.1} A great strength of specific-heat measurements is that they give information on the bulk behavior of a solid, and as such are useful in determining whether an effect observed by some other technique, for example resistivity measurements, is a feature of the bulk material or due to grain boundaries, surface phases, or some other defect. However, it is not easy to get an accurate specific-heat measurement, especially if the specimen has as small a mass as a few tens of milligrams, which is usually the case for a single crystal. The small specific-heat of solids increases difficulties for researchers because small heat influxes from the surroundings, for example vacuum fluctuation, can lead to significant errors in the determination of the specific-heat of a solid. Thermal isolation is a big challenge to measure a small specific-heat when using a static measurement method. To obtain accurate specific-heat, it is necessary to measure the specimen temperature increment

without any heat loss. Theoretically, the specimen must be under adiabatic condition. In reality, there is no truly adiabatic condition. Even with a relaxation method, it is also important to reduce heat transfer between the specimen and the surroundings. Unlike electrical current, heat current can flow along the sample-holder support rod, electrical wire, or even in vacuum by radiation. To achieve good thermal isolation, these factors must be considered. We will talk about the thermal isolation techniques later in apparatus descriptions. In the following sections, we describe several commonly used specific-heat measurement methods and then introduce the method used in this work.

A convenient starting point for the measurement of specific-heat is the classical definition of the specific-heat, C_p

$$C_p(T) = (\Delta Q / \Delta T) / M \quad (2.1)$$

In a ‘step’ or ‘pulse’ heating technique (adiabatic calorimetry), ΔQ is a heat energy input that causes a small temperature rise ΔT in a specimen of mass M . This method can be traced back to Nernst,^{2,2} and it remains today one of the most accurate methods for obtaining specific-heat data. In practice, the specimen is thermally connected to an addenda, which consists of the specimen support system or container, thermometer, resistive heater, and any other wiring. The addenda/sample assembly is thermally insulated from the surroundings. Thermal equilibrium with the surroundings is established before and after the heat pulse ΔQ . The temperature is monitored as a function of time, and the temperature at

the beginning T_i and the temperature at the end T_f are corrected for any heat exchange with the environment by extrapolating T before and after the heat pulse to the time that corresponds to the midpoint of the pulse (Fig. 2.4(a)). The temperature increment is then $\Delta T = T_f - T_i$, from which C_p is obtained at the temperature $T_m = (T_i + T_f)/2$.

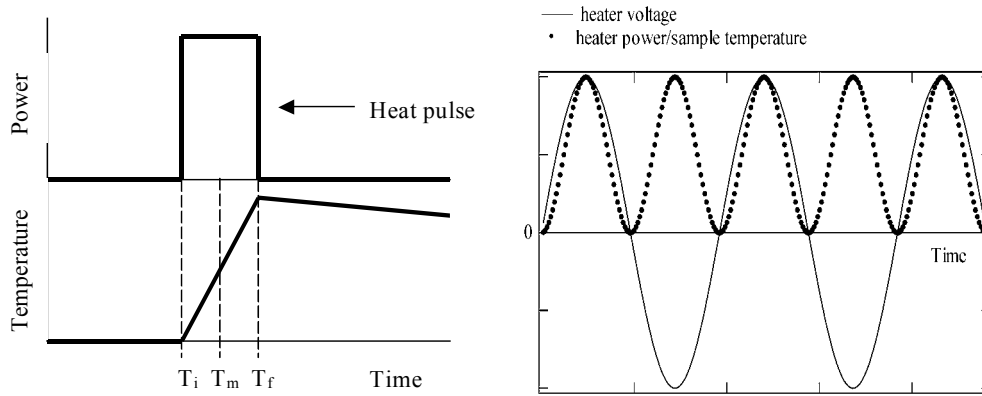


Fig. 2.4: (a) Illustration of 'pulse' heating technique (adiabatic calorimetry). The upper part is the heater power vs time and the lower part is sample temperature vs time. (b) AC calorimetry

The need for excellent thermal isolation and the minimization of stray heat leaks place a lower limit of about 200 mg on specimen mass for adiabatic calorimetry. The requirement for specific-heat measurement on smaller specimens has led to the development of a number of techniques. One of them is AC temperature calorimetry,^{2,3} which is a technique where the specimen is heated by an AC current of frequency $\omega/2$ passing through a resistance heater (Fig. 2.4(b)). Measurement of the peak-to-peak AC temperature response, T_{ac} at frequency $\omega/2$,

by synchronously detecting the voltage across a heater resistance at frequency ω , using a lock-in amplifier, enables the total specific-heat C_p to be calculated by:

$$T_{ac} = \frac{Q_0}{2\omega C_p} \left[1 + \frac{1}{\omega^2 \tau_1^2} + \omega^2 \tau_2^2 + \frac{2K_b}{3K_s} \right]^{-1/2} \quad (2.2)$$

where Q_0 is the amplitude of the sinusoidal heat flux, τ_1 is the specimen to bath relaxation time, τ_2 is the response time of the specimen, heater and thermometer to the heat input, K_b is the thermal conductance of the specimen to the bath, and K_s is the thermal conductance of the specimen. This equation can be simplified under some experimental conditions, namely $\tau_2 \ll 1/\omega$, $\tau_1 \gg 1/\omega$ and $K_s \gg K_b$, giving a simple expression for C_p ,

$$C_p \approx \frac{Q_0}{2\omega T_{ac}} \quad (2.3)$$

The ability of the AC-method to detect small changes in specific-heat has made it one of the favored methods for small sample calorimetry, or what has become known as microcalorimetry or nanocalorimetry.

Recently thermal relaxation calorimetry^{2,4} has become particularly popular as it is suitable for small samples, can be used over a wide temperature range (from 1K to 300K), cryostat design and specimen mounting are simple, and signal-to-noise can be improved with signal averaging as part of the computer-controlled system. In the thermal relaxation method, the specimen is connected by

a weak thermal link to a constant temperature bath at temperature T_0 . The temperature of the sample is increased by a small amount ΔT_0 ($\sim 1\text{K} - 0.5\text{K}$) and then allowed to decay exponentially down to the bath temperature. The temperature of the specimen, T_s , is described by:

$$T_s = T_0 + \Delta T_0 \exp(-t/\tau_1) \quad (2.4)$$

where t is the time from the onset of temperature decrease and τ_1 is the specimen to bath time constant, which can be calculated out by fitting the temperature vs. time decay curve. The specific-heat, C_p , is determined from the measurement of τ_1 and resistance of the weak thermal link, R ,

$$C_p = \tau_1/R \quad (2.5)$$

2.2.2 Specific-Heat Measurement Principle

The above is the transitional thermal relaxation method. But there is an R , which is unknown. Usually the resistance of the thermal link varies with temperature and it changes every time the specimen is loaded. In the following, we introduce a method that bypasses measuring the R .

Now let us consider the time during which the pulse is applied. What can be measured directly is the sample temperature increase ΔT_0 , pulse width t_0 , the heater current I_0 and voltage V_0 during the pulse time. Thus the heater power P_0 is $I_0 \times V_0$. During the pulse time, the sample temperature can be described as:

$$T_s = T_0 + R P_0 (1 - \exp(-t/\tau_1)) \quad (2.6)$$

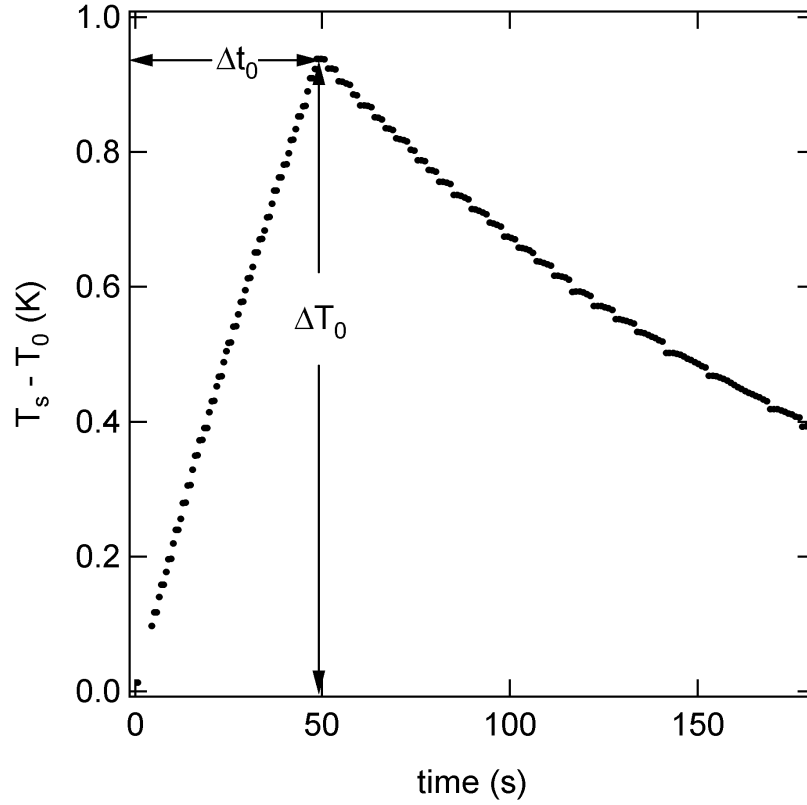


Fig. 2.5: Relaxation calorimetry method: heat pulse response of specimen temperature vs time.

The heat dissipation of the sample, heater, and holder to the surrounding during this period of time is:

$$Q_{dis} = \int_0^{t_0} \frac{T_s - T_0}{R} dt = P_0 t_0 + P_0 \tau_1 \exp(-t_0/\tau_1) - P_0 \tau_1 \quad (2.7)$$

And the total heat input is:

$$Q_{\text{in}} = P_0 t_0. \quad (2.8)$$

Thus the heat used to raise the sample and addenda temperature is:

$$\Delta Q = P_0 \tau_1 - P_0 \tau_1 \exp(-t_0/\tau_1) \quad (2.9)$$

According to the definition of specific-heat, the C_p is:

$$C_p = \frac{\Delta Q}{\Delta T_0} = \frac{I_0 \times V_0 \tau_1 (1 - \exp(-t_0/\tau_1))}{\Delta T_0} \quad (2.10)$$

ΔT_0 is the specimen temperature increase from the pulse starting point to the pulse ending point.

This is the principle used to measure specific-heat in this work. Compared with the traditional thermal relaxation measurement, this method bypasses directly measuring the weak thermal link resistance and it does not neglect the heat dissipation during pulse time (which is usually several tens of seconds), which gives a more accurate result.

On occasion, it may also be necessary to consider the behavior of τ_2 , the response time of the specimen, heater and thermometer. So-called τ_2 effects occur when τ_1 and τ_2 are comparable, occurring when specimen and thermometer are

not at the same temperature, i.e., for a specimen of very low thermal conductivity. The signature of this behavior is an overshoot in the thermometer and a non-exponential shape in the decay curve. In our work, specimens are single crystals, which have good conductivity; the holder and thermometer are also designed to eliminate τ_2 effects (we discuss this issue again later).

2.2.3 Specific-Heat Measurement Apparatus

Fig. 2.6 shows the core components of the calorimeter and Fig. 2.7 displays an associated electronic block diagram.

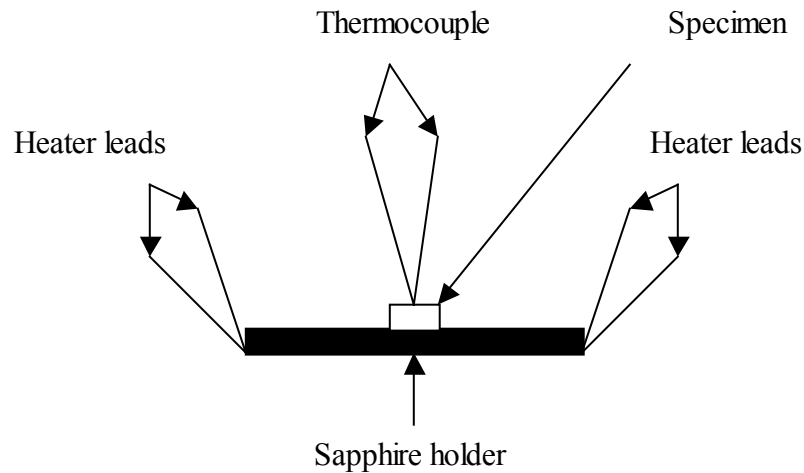


Fig. 2.6: Illustration of the core components of the calorimeter.



Fig. 2.7: Picture of the core components of the calorimeter (sapphire holder is removed).

The sample holder is a piece of sapphire with a size of $10\text{ mm} \times 5\text{ mm}$. A layer of metal is deposited on one surface of the sapphire to serve as a heater. To increase heater resistance, two lines are scratched on the metal film; thus the electric current flow follows a zigzag path. Two copper wires (0.001 inch) are adhered to the metal film heater via silver epoxy at the long ends of the sapphire. The other ends of the wires are soldered with another two copper wires, which are attached to a copper base (Fig. 2.7) at the ends. To calculate the heater power, both voltage across the heater and the electric current through the heater are measured. The copper wires serve not only as leads, but also as suspension for the holder. The measured crystal is mounted on the other surface of the sapphire with

a thermal compound. The contact surface is well polished to reduce τ_2 effects. The crystal is cut into a thin pallet with two parallel surfaces, which are polished on a Lapping & Polishing Machine (South Bay Technology (SBT) Model 920). The thickness of the specimen is about 0.5 mm. A copper-constantan thermocouple is attached to the upper side of the surface of the specimen. The other ends of the thermocouple wire are connected to the copper base. Thus the thermocouple can measure the temperature difference between the sample and the copper base. The copper base is shielded with a brass can on whose inner surface sits a diode temperature sensor. Because the base and the can are well contacted, the temperature of the can is very close to the temperature of the base. To increase thermal contact of the electrical wires to the base, the wires are wound on the base for several turns. Thus one end of the wire is at the specimen temperature and the other end is at the base temperature, which is quite stable.

We minimize the τ_2 effects in several ways. First, the sapphire holder and crystal specimen have good thermal conductivity. Their surfaces are well polished to achieve good contact. Secondly, the specimen is cut into a thin pallet, which allows a big heat-transfer area and short transfer distance. Third, we use a thermocouple instead of a diode or Cernox sensor as thermometer. The thermal mass of the thermometer is greatly reduced and its response is almost instant. The measured data show that the specimen temperature T_s decays exponentially with time, which means the τ_2 effects are very small. Besides, the time when T_s reaches the peak is just 0.5 second later than the time when the pulse stops. Usually the

measured τ_1 is several tens of seconds. Thus we can safely say our design meets the $\tau_1 \gg \tau_2$ requirement.

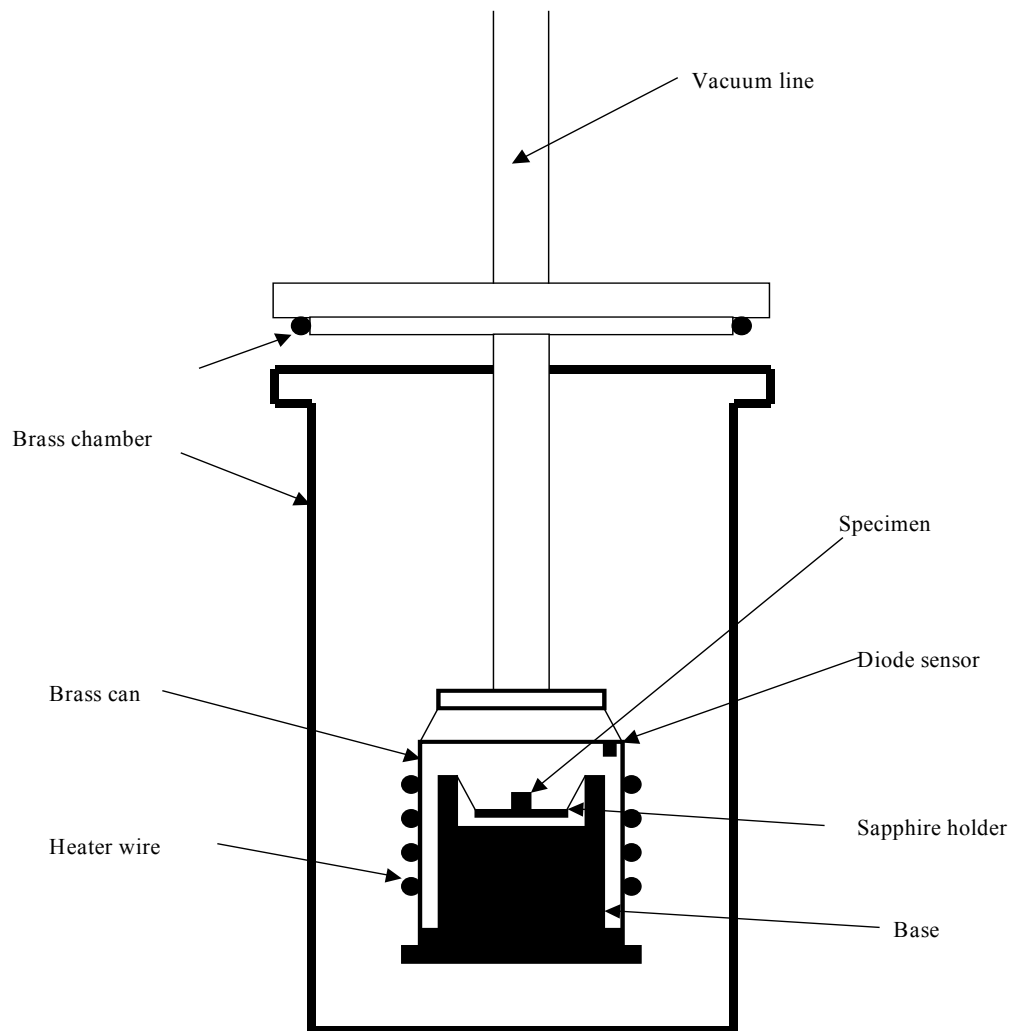


Fig. 2.8: Illustration of specific-heat measurement head.

Because the electrical wires become very fragile after one measurement cycle, we replace them every time we change a specimen. After the specimen is mounted on the holder and the electrical wires are attached to the base, the brass can is put on the base as a cap. Two screws are used to fix them. A constantan wire is wound around the can to serve as a heater to control the can temperature (Fig. 2.8). The can is hung on a Germany silver rod, which connects to a vacuum diffusion pump. A brass chamber is then put on. The chamber is sealed with indium. The vacuum level inside the chamber can reach as high as 10^{-8} Torr. A high vacuum is very important to measure the heat capacitance accurately. After a heat pulse, the temperature of the sample starts to decay exponentially. The rate can be calculated by fitting the decay curve. The voltage meter, however, has limited sampling rate to record the curve. The slower the decay, the more points for curve fitting and thus the more accurate the heat capacitance we can achieve. Because the sample temperature decay rate is proportional to the heat dissipation rate of the sample, a high vacuum is used to reduce the heat dissipation rate of the sample. The chamber is removable. It is bolted to a brass lid. The Germany silver pipe is connected to the chamber. It serves as a channel for vacuum. An electrical wire must go through the pipe. Because the electrical wire is covered with a plastic sheath, the sheath needed to be peeled off with a knife at the point where the wire comes out of the pipe. Glue is used to seal the opening. The chamber is put into a liquid nitrogen cryostat. It can be either dipped into liquid nitrogen or just cooled by cool nitrogen air.

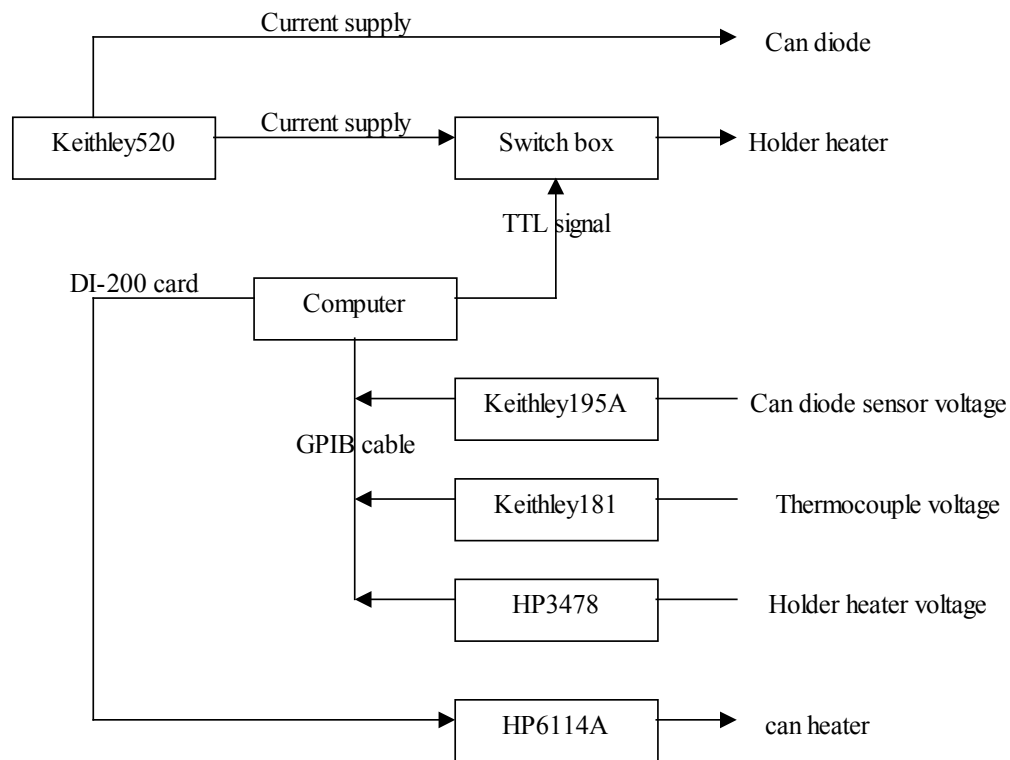


Fig. 2.9: Specific-heat measurement control and data collection block diagram.

The experimental control and data-collection system block diagram is showed in Fig. 2.9. The voltage across the specimen holder heater is measured with a HP3478 voltage meter and the voltage from the thermocouple is measured with a Keithley 181 nano-voltage meter. A Keithley 197 micro-voltage DMM is used to measure the voltage across the diode. The signals are put into an IBM PC via a GIPB cable. The Lakeshore 520 Temperature Controller is used for the diode current supply of 10 mA. It also supplies the current for the heater on the specimen holder. Because the heater current is only needed during pulse time, there is a switch box on the path of the current. A relay, which is controlled by an

NPN transistor, is in the switch box. A 5 V step from the computer DI-200 card triggers the transistor and the transistor then turns on the relay. To get an accurate heater current (although a rough value of the current can be read out from Lakeshore 520 Temperature Controller), a Keithly EM617 multimeter is utilized. As the current source drift is very small during the experiment, the heater current is only measured manually before and after the experiment. The analogue output of the DATAQ card controls the HP 6114 Precision Power supply. The DATAQ produces a 0-10 V output on the HP power supply. This power supply drives the can heater.

2.2.4 Specific-Heat Measurement Operation

After a sample of known mass is loaded into the calorimeter, the chamber is sealed with indium wire and a probe connects to a pumping manifold. Before the chamber is put into the cryostat Dewar, the chamber is pumped down with a diffusion pump (base pressure 10^{-7} Torr) for several hours. Then the chamber is loaded into a liquid-nitrogen Dewar for cooling down to 80 K – 100 K. As the temperature goes down, the gas inside the chamber is frozen; thus the vacuum in the chamber is very high and the cooling rate can be very slow, the temperature will never reach the target temperature. To solve this problem, we leave the pump valve just slightly open so that the pump power is weak enough to allow a reasonable cooling rate. After the temperature reaches the first set temperature point, the computer starts to control the can temperature. If the temperature point is higher than the can temperature, the HP power supply applies a voltage on the can heater. This voltage may vary after the computer gets feedback from the can

temperature response. A PID (Proportional, Integral, Derivative) control algorithm is used. After the can temperature is heated to above the set temperature, the can temperature drift rate is calculated. Once the drift rate is smaller than 0.05 mK/s, the target temperature point is reset to be the current can temperature. The reason we reset the target temperature point is to reduce the heater overshoot effect so that the can temperature becomes stable as soon as possible. Only after the can temperature is within a small range (50mK) of the new set point for a certain amount of time, is the can temperature considered stable. After 50 seconds of waiting time, the specimen temperature rate is calculated. We wait till the specimen temperature rate is below 0.1 mK/s for 20 counts. Then, a 5 V step is applied to the NPN transistor to trigger it. The current flow turns the relay on. A current pulse is applied through the specimen heater. The temperature of the specimen and holder increases, and then decreases exponentially after the pulse is done. At the same time, the voltage across the thermocouple is recorded as well as the voltage across the heater. By fitting the temperature vs. time decay curve, the time constant is also obtained. We just plug these numbers into the equation and the C_p can be obtained. This method is good if the specific-heat changes slowly with temperature or a transition is second-order. For first-order transitions, we must consider the other way. The signature of the first order transition is that at the transition point, the specimen temperature remains constant even after a heat pulse is applied. What we can do is to apply a heat pulse long enough to meet the latent heat. The temperature curve is recorded.

By analyzing the curve, we can obtain the latent heat and the entropy change at the transition point.

2.2.5 Specific-Heat Measurement Calibration

For calibration of the calorimeter, we performed a measurement on an Fe_3O_4 single crystal. The specific-heat of Fe_3O_4 has been studied by Honig *et al.*^{2,5} There is a first-order phase transition, called the Verway transition, at around 120K (the transition temperature depends on the oxygen content). By studying the phase transition, the latent heat associated with the transition can be obtained. The theoretical model calculation shows that the latent heat is around 5.8 J/mole.^{2,6}

An Fe_3O_4 crystal was grown in the Image Furnace by the floating zone method mentioned above. For comparison, the thermal conductivity of the Fe_3O_4 crystal was also measured. In the temperature region beyond the phase transition, we used the thermal relaxation method to measure the specific-heat; around the transition, we applied a long time pulse (more than one thousand seconds) and recorded the response temperature curve. Fig. 2.10(a) shows the temperature vs. time curve around the transition point. It can be seen that before the transition, the temperature increased as the heat pulse was applied; at the transition point, the temperature remained constant for several hundred seconds; when the transition was done, the temperature increased again. After the heat pulse stopped, the temperature started to decrease and remained constant again when the temperature dropped to the transition point. This curve can be converted to an entropy vs. temperature curve by knowing the heater power. (Fig. 2.10(b)) The entropy change at the transition point is 5.87 J/mole, which is very close to the theoretical

value. The measured C_p in the range of 100 K to 300 K is shown in Fig. 2.11 with dots. The solid curve is the result from Honig *et al.* It can be seen that these two curves overlap each other, which means our calorimeter is well calibrated.

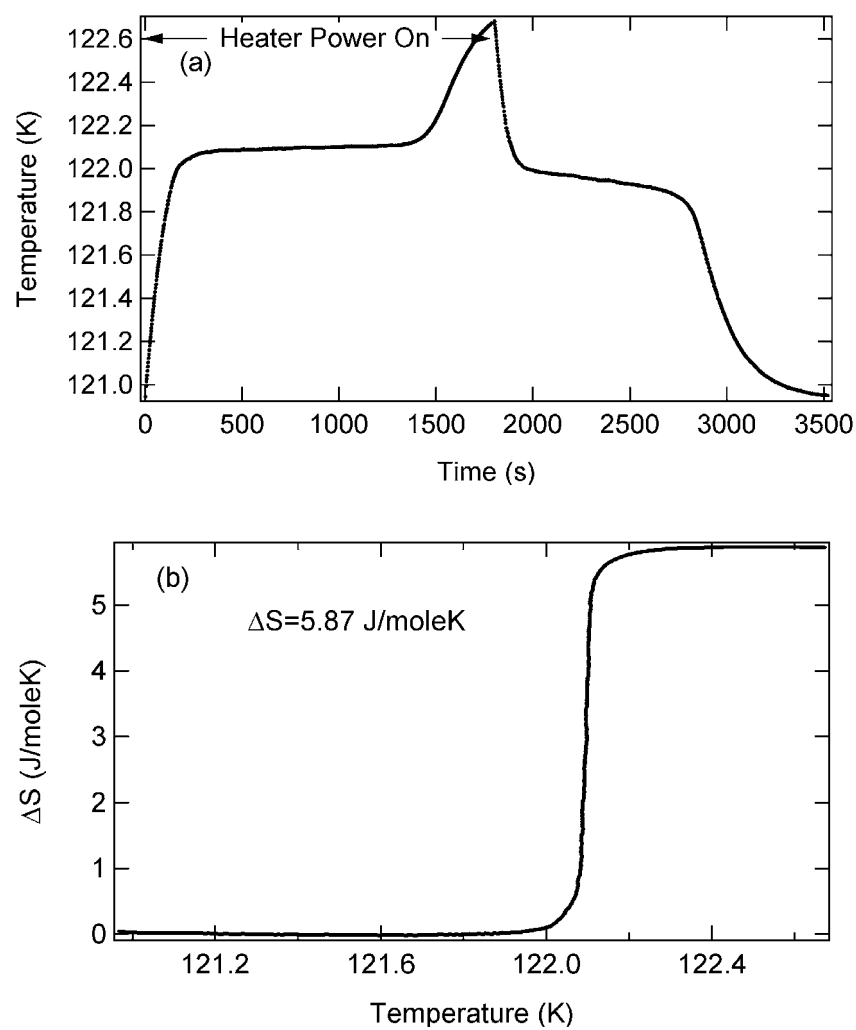


Fig. 2.10: (a) Heat pulse response of Fe_3O_4 crystal temperature vs time. (b) Entropy change at Verway transition of Fe_3O_4 crystal.

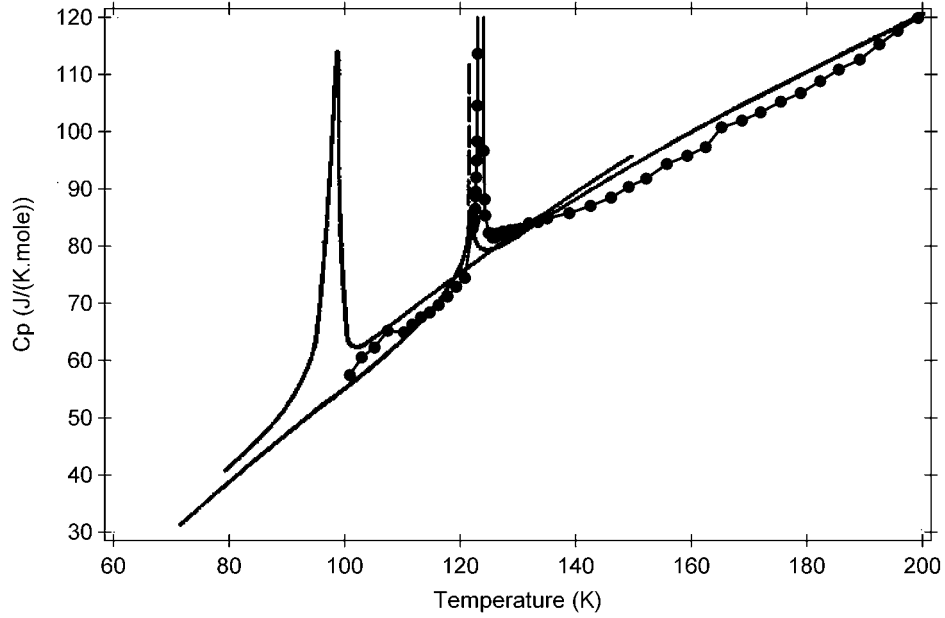


Fig. 2.11: Specific-heat of $\text{Fe}_{3(1-\delta)}\text{O}_4$ crystals. Solid lines are after J. M. Honig *et al*^{2.5} by permission [from *Phys. Rev. B* **43**, 8461-8471 (1991). Copyright (1991) by the American Physical Society]: $\delta = -0.00018$, peak at around 120 K; and $\delta = 0.0049$, peak around 100 K. The line with solid circle is our result, which overlaps the one with $\delta = -0.00018$.

2.3 RESISTIVITY MEASUREMENT

Resistivity measurements as a function of temperature were performed on single crystal specimens with a method developed by Montgomery.^{2.7} The crystal specimens are cut into rectangular prisms. The three dimensions of the rectangular specimen are labeled as a , b , and c . The c , which is the shortest, is about 0.5mm ~ 1mm. The a or b is several mm.

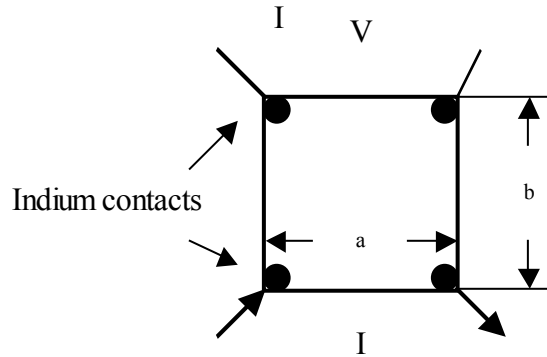


Fig. 2.12:

Current and voltage contacts on specimen in resistivity measurement.

Choose an ab face and let a current I flow into the block at one of the corners of the face and out at an adjacent corner of the same face. The voltage V measured between the two remaining corners of the face is:^{2,8}

$$V = (4/\pi)MI\rho, \quad (2.11)$$

where ρ is the resistivity of the material, M is a geometry factor, which depends only on the block dimensions a , b , and c and has the dimension of 1/length. Theoretical calculation shows that the M can be expressed in terms of a series:

$$M = (2/ac) \sum_{l=0}^{\infty} \sum_{n=0}^{\infty} [\varepsilon_n / (s \sinh(\pi bs))], \quad (2.12)$$

in it,

$$s = \left\{ \left[(2l+1)/a \right]^2 + (n/c)^2 \right\}^{1/2} \quad (2.13)$$

$$\varepsilon_0 = 1, \quad \varepsilon_n = 1 \text{ for } n > 0. \quad (2.14)$$

Present-day computer technology allows us to calculate the series by a numerical method. The three dimensions of the specimen, a , b , and c , were measured on a Diamond Wheel Saw Machine (South Bay Technology Model 650). Because the size of the specimen is very small, the size of the indium contact points can introduce some errors to the measurement. However, in this work, what we care about is the relative values of the single-crystal resistivity. The errors introduced by the contact points apply to all the measurements. In fact, our results are quite consistent with those of others.

In practice, the specimen is mounted on a small piece of mica glass with a very small amount of thermal compound. Four pieces of copper wire are attached to the surface of the specimen via an Indium pad. The whole assembly is put on a round copper thin sheet with a copper cap to shield them. The cooling system is a refrigerator with He as refrigerant. A Lakeshore Cernox temperature sensor is put on the cooling head. Temperature is monitored and controlled by a Lakeshore temperature controller. Current is provided with a Keithley Model 224 Current Source and voltage is recorded with a Keithley 181 nano-voltage meter. Data are recorded under GPIB control of these instruments with a personal computer. To eliminate the contribution of the bias voltage, opposite direction currents are applied at each measuring point. Suppose the absolute value of the current is denoted as I , and the resistance of the specimen is R , which equals to V/I in the previous formula. When the current flows in the positive direction, the measured voltage is:

$$V_+ = V_{bias} + IR, \quad (2.15)$$

while for current flows in the negative direction, the measured voltage is:

$$V_- = V_{bias} - IR. \quad (2.16)$$

Thus we have

$$R = \frac{V}{I} = \frac{V_+ - V_-}{2I}. \quad (2.17)$$

Finally, we have the resistivity of the material

$$\rho = \frac{\pi V}{4IM} = \frac{\pi(V_+ - V_-)}{8IM}. \quad (2.18)$$

2.4 THERMOELECTRIC POWER MEASUREMENTS

Thermoelectric power measurements were performed on a laboratory-built system diagramed in Fig. 2.13. Specimens are mounted between two brass heater stages, each controlled independently by a Lakeshore Model 304 Temperature Controller with DT-470 sensing diodes. The stage is sheltered in a styrofoam canister and submerged into a liquid-nitrogen dewar. Computer control commands the temperature controllers to a target temperature, and a measure of voltage across the brass stages ΔV_0 and temperature difference ΔT_0 are made. The controllers are then programmed to values differing about the target by $\pm 1\text{K}$, and again the voltage of the metallic stage ΔV_1 and the temperature difference ΔT_1 are

measured. Without considering the contribution to the thermoelectric power from copper leads, the thermoelectric power of the specimen is:

$$\alpha = \frac{\Delta V}{\Delta T} = \frac{\Delta V_1 - \Delta V_0}{\Delta T_1 - \Delta T_0}. \quad (2.19)$$

However, after making correction by considering that contribution, the thermoelectric power of the specimen becomes

$$\alpha = \alpha_{Cu} - \frac{\Delta V}{\Delta T} = \alpha_{Cu} - \frac{\Delta V_1 - \Delta V_0}{\Delta T_1 - \Delta T_0}. \quad (2.20),$$

in which α_{Cu} is the thermoelectric power of the copper lead.

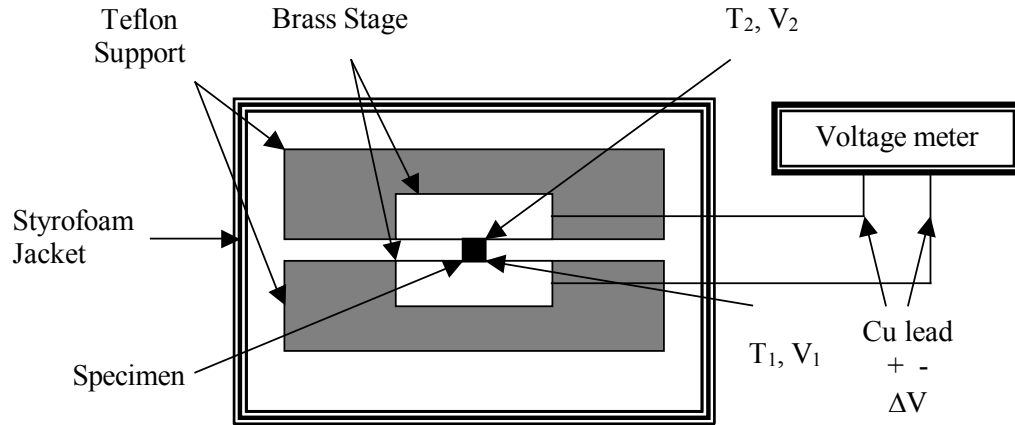


Fig. 2.13 Diagram of Seebeck apparatus sample stage.

Let us see how this happens. Fig. 2.13 is a diagram of the Seebeck apparatus sample stage. The heaters and temperature sensors are in two brass stages (not shown in the picture). Suppose there is a small temperature difference

between the two brass stages, i.e. $\Delta T = T_2 - T_1$ with ΔT greater than zero. If the thermoelectric power of the specimen is denoted as α , then we have

$$V_2 - V_1 = -\alpha(T_2 - T_1). \quad (2.21)$$

However, $V_2 \neq V_+$ and $V_1 \neq V_-$ because the voltage is measured at room temperature T_{room} and there is a contribution from the thermoelectric power of the copper lead. The relations are:

$$V_+ = V_2 + \int_{T_2}^{T_{\text{room}}} -\alpha_{Cu}(T) dT, \quad (2.22)$$

and

$$V_- = V_1 + \int_{T_1}^{T_{\text{room}}} -\alpha_{Cu}(T) dT. \quad (2.23)$$

The measured voltage is

$$\Delta V = V_+ - V_- = V_2 - V_1 - \int_{T_2}^{T_1} \alpha_{Cu} dT \approx -\alpha(T_2 - T_1) + \alpha_{Cu}(T_2 - T_1) = -\alpha\Delta T + \alpha_{Cu}\Delta T \quad (2.24)$$

Finally, we have

$$\alpha = \alpha_{Cu} - \frac{\Delta V}{\Delta T}. \quad (2.25)$$

2.5 Magnetic measurements

Magnetic measurements were performed with a Magnetic Properties Measurement System (MPMS) manufactured by Quantum Design. This system performs an automated measurement of the magnetic properties of materials under varying conditions of temperature, magnetic field, and time. The basic system operates between temperatures 1.7 to 800 K and magnetic field $-55,000$ to $55,000$ Oe.

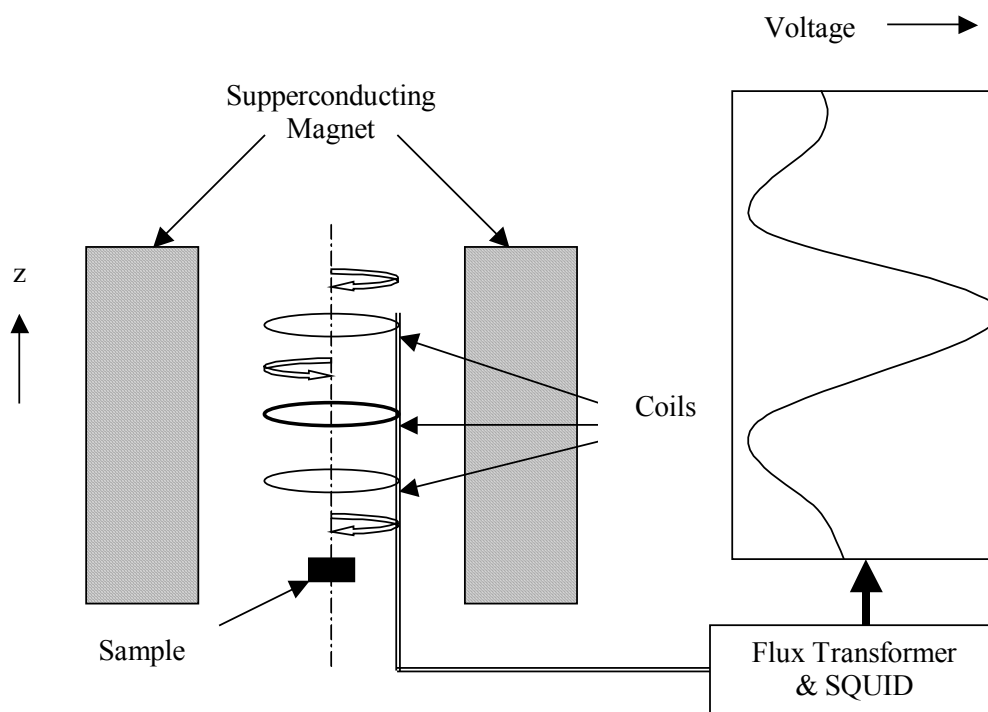


Fig. 2.14: Core components and geometry of the Quantum Design MPMS SQUID magnetometer.

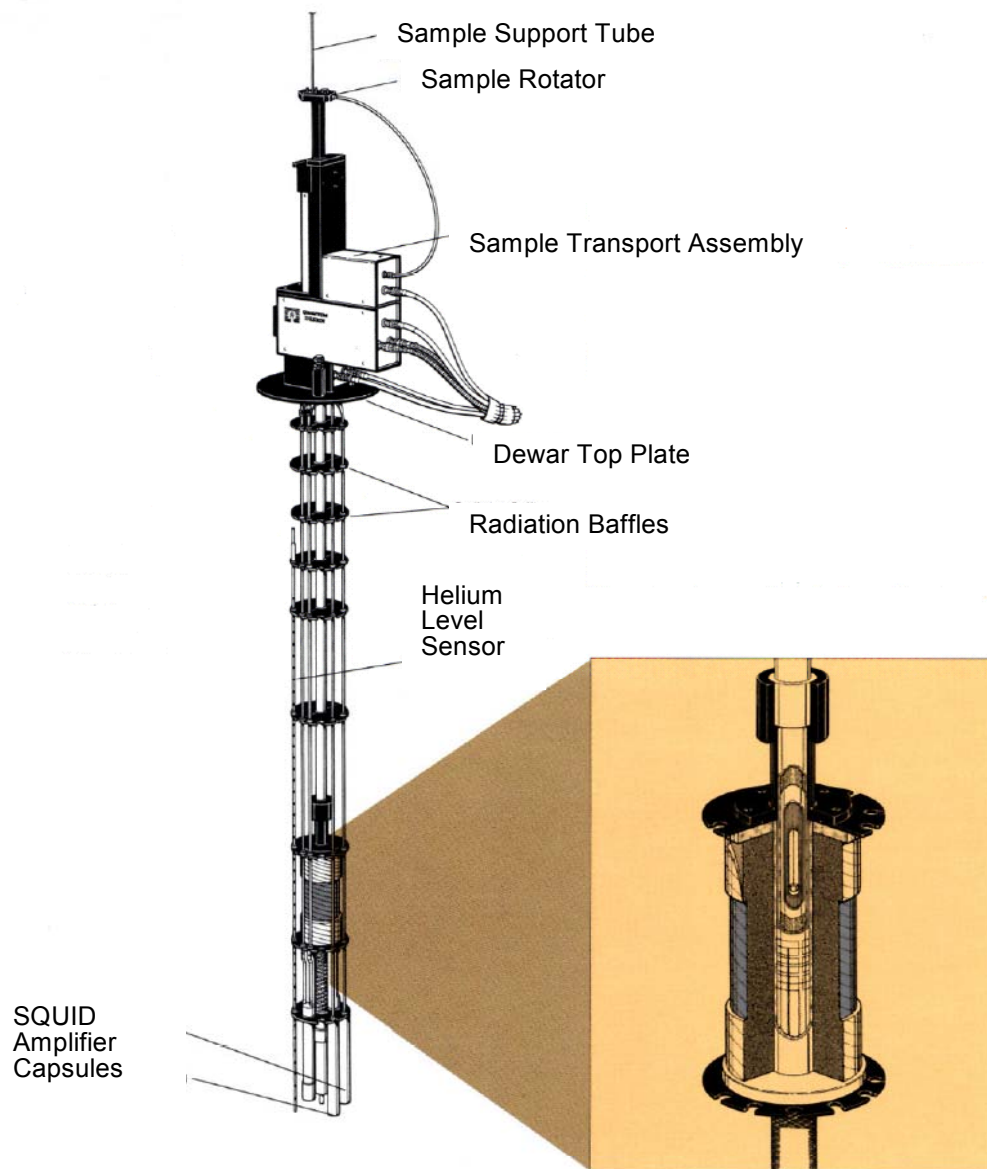


Fig. 2.15: Sample supporting assembly, superconducting magnet and SQUID amplifier capsules of the MPMS. [From *Magnetic Property Measurement Systems Brochure*, Copyright by Quantum Design, www.qdusa.com]

As a SQUID (Superconducting Quantum Interference Device)-based instrument, the fundamental quantity measured by the system is the magnetic flux produced by a sample's magnetic moment. The moment is induced by the application of an external magnetic field derived from a superconducting magnet.

The sample space is located within the winding of a superconducting coil and of a superconducting magnet capable of producing a large, uniform, DC magnetic field over the coil region. The magnet and coil are wound coaxial to the z -axis of the system. In the course of the measurement, the sample is mechanically scanned along the z -axis from positions well below to well above the primary coil. The sample's moment induces current in the primary coil proportional to the sum of the flux penetrating each of the coil loops. The current is passed to the secondary windings of the flux transformer, which are coupled to an RF SQUID. The flux produced at the SQUID is converted to a signal that produces a DC voltage proportional to the flux sum through the primary coil.^{2,9}

As the diagram indicates, the primary coil is wound in three sections, all series connected. The upper and lower sections are spaced about the central section by equal amounts and wound about the z -axis in a direction opposite to the central coil section. The central section is wound with twice the number of turns as either of the outer sections, and the total number of positive and negative turns is zero. This configuration is used to reduce noise in the detection circuit caused by fluctuation in the large magnetic field of the superconducting magnet. The coil set also minimizes background drifts in the SQUID detection system caused by relaxation in the magnetic field of the superconducting magnet. Ideally if the

magnetic field is relaxing uniformly, the flux change in the two-turn center coil will be exactly canceled by the flux change in the single-turn top and bottom coils. On the other hand, the magnetic moment of a sample can still be measured by moving the sample through the detection coils because the counter-wound coil set measures the local changes in the magnetic flux density produced by the dipole field of the sample.

A small sample with an induced moment passed through these coils will produce a voltage vs. z -position plot as shown on the right of Fig. 2.14. The MPMS software converts this plot to a magnetic moment by the application of a curve-fitting algorithm.

Chapter 3: The $\text{La}_{1-x}\text{Sr}_x\text{MnO}_3$ system¹

In this chapter, we are going to study the $\text{La}_{1-x}\text{Sr}_x\text{MnO}_3$ system. The evolution with x of the complex phase diagram below 310 K of $\text{La}_{1-x}\text{Sr}_x\text{MnO}_3$ in the range $0 \leq x \leq 0.35$ (Fig. 3.1) was mapped out with measurements on a series of melt-grown single crystal samples of resistivity $\rho(T)$, thermoelectric power $\alpha(T)$, specific-heat $C_p(T)$, magnetization $M(T)$ in applied magnetic fields $H = 20$ Oe, 5 kOe, and magnetization at 5 K up to 50 kOe. Between the canted-spin antiferromagnetic insulator (CAFI) and ferromagnetic metal (FM) phases, an unusual interplay between charge, orbital, and magnetic ordering is revealed. In the paramagnetic range $T_c < T < T_{JT}$ the electrons of e -orbital parentage are preferentially ordered into (001) planes to give an O' -orthorhombic ($c/a < \sqrt{2}$) structure. As the temperature decreases to T_c the system exhibits a colossal magnetoresistance (CMR). At temperatures below a $T_{oo} < T_c$, a different orbital order is found in a ferromagnetic insulator (FI) phase. In a narrow temperature interval $T_{oo} < T < T_c$, the system is conductive and a spin glass in an applied magnetic field $H = 20$ Oe is transformed by $H = 50$ kOe into a ferromagnetic vibronic (FV) phase. As the cooperative orbital-ordering temperature T_{JT} decreases with increasing x , the transition at T_{JT} changes from second-order to first-order. In $H = 50$ kOe at 5 K, the magnetization of the FI phase exceeds the theoretical spin-only value of $(4-x) \mu_B/\text{Mn}$, reaching $4.4 \mu_B/\text{Mn}$ at $x = 0.15$; the

¹ Part of the materials in this chapter was published on Phys. Rev. B **64**, 144414 (2001). Copyright (2001) by the American Physical Society

magnetization of the FM phase has the spin-only value. Discontinuous changes in T_c occur where it crosses T_{JT} , a transition from vibronic to metallic ferromagnetism (FV to FM), and the O^* -orthorhombic phase to rhombohedral (R) phase transition temperature T_{OR} showing that all these transition are first order.

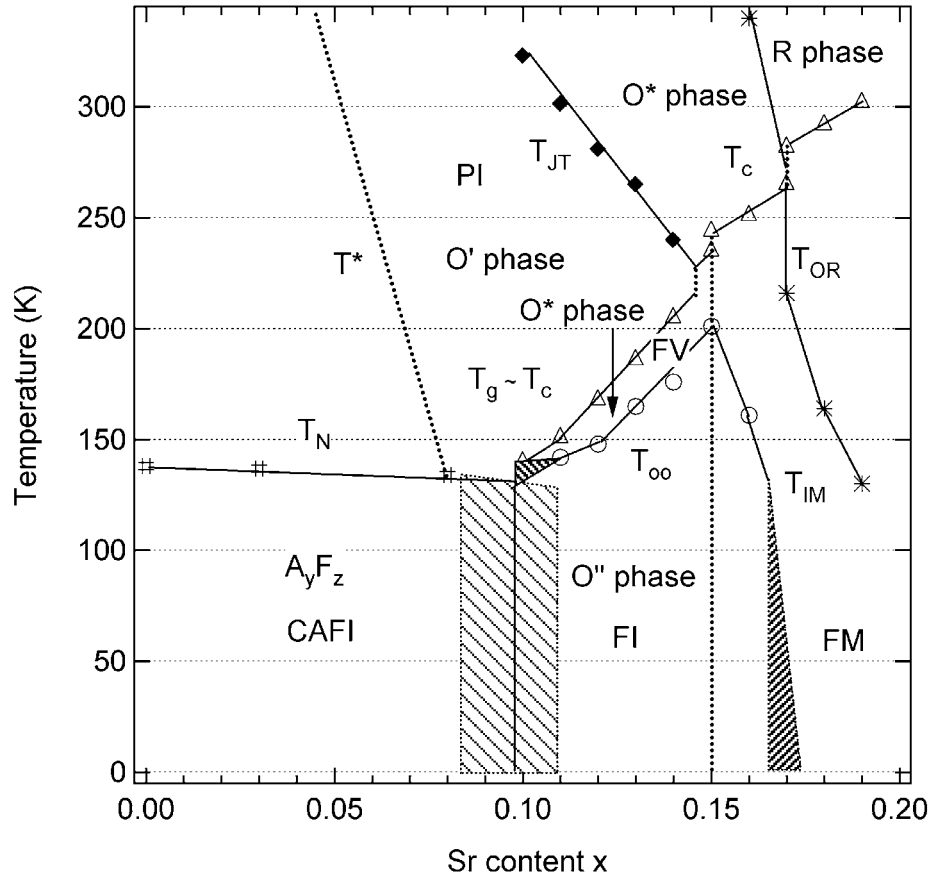


Fig. 3.1: Phase diagram for $\text{La}_{1-x}\text{Sr}_x\text{MnO}_3$, $0 < x < 0.20$. Experimental points above 310 K taken from the literature; T_N and two values of T_c for $x = 0.17$ taken from $M(T)$; two values of T_c for $x = 0.15$ taken from $C_p(T)$; all other points taken from Fig. 3.2. The shade zones are two-phase regions.

3.1 INTRODUCTION

The $Ln_{1-x}A_x\text{MnO}_3$ (Ln = lanthanide, A = alkaline-earth) perovskites have been studied intensively in recent years because they exhibit such unusual properties as a colossal magnetoresistance (CMR) and spin-glass behavior. These unusual properties are found at a crossover from antiferromagnetic to ferromagnetic order where the σ -bonding $3d$ electrons change from a localized to an itinerant character, while the π -bonding $3d$ electrons remain localized with a spin $S = 3/2$ on every Mn atom. In addition, the σ -bonding electrons have an orbital degeneracy that results in cooperative Jahn-Teller orbital ordering where the σ -bonding electrons are localized. The interplay between spin, charge, and orbital degrees of freedom has provided an important challenge to existing theories of electronic states in solids.

Because the atomic radii are different for different alkaline elements, in $\text{La}_{1-x}A_x\text{MnO}_3$, substitution of $A = \text{Ca}$ or Sr gives different tolerance factors t . For a specific A , the concentration of A can also change the tolerance factor. In this chapter we are going to study a systematic series of measurements, including specific-heat, on melt-grown crystals of $\text{La}_{1-x}\text{Sr}_x\text{MnO}_3$ across the compositional range $0 \leq x \leq 0.35$ with special emphasis on the range $0.08 \leq x \leq 0.19$, where the phase diagram has been shown to be particularly complex; a crossover from canted-spin antiferromagnetic insulator to ferromagnetic metal occurs with increasing x in this compositional range.

LaMnO_3 contains a localized t^3e^1 $3d$ -electron configuration at the octahedral-site Mn^{3+} ions. The e -orbital degeneracy is removed by locally

cooperative oxygen displacements that fluctuate in three dimensions (3D) at temperatures $T > T_{JT}$; the fluctuations allow breathing-mode distortions that induce the disproportionation reaction $2\text{Mn}^{3+} = \text{Mn}^{2+} + \text{Mn}^{4+}$ on a fraction of the Mn sites and a partial disproportion sets in above T^* ($T^* \approx 600$ K, $T_{JT} \approx 750$ K); on cooling below T^* , the cooperative oxygen displacements are static.^{3.1} The disproportionation reaction introduces an equal number of mobile holes (Mn^{4+}) and electrons (Mn^{2+}). Therefore, there is a transition from an insulator to a conductive phase at T_{JT} . Moreover, ordering of the occupied e orbitals into the (001) planes below T_{JT} confines the dominant ferromagnetic σ -bond superexchange interactions to the (001) planes; the π -bond superexchange interactions dominate along the [001] axis to give an antiferromagnetic coupling between the ferromagnetic (001) planes.^{3.2} A Dzialosinskii anti-symmetric super-exchange term cants the anti-ferromagnetic spins to give a weak ferromagnetic component below the Néel temperature $T_N = 145$ K; the canted-spin antiferromagnetic (CAF) order is classified as A_yF_z in space group $Pbnm$.^{3.3}

In the range $0 < x < 0.10$, the canted-spin Type-A antiferromagnetic component is oriented along the b -axis and the weak ferromagnetic component is along the c -axis; the Dzialoshinskii vector D_{ij} is along the a -axis in space group $Pbnm$. A ^{139}La study^{3.4} has revealed the presence below T_N of a second phase in the $x = 0.05$ sample similar to what is found in the system $\text{La}_{1-x}\text{Ca}_x\text{MnO}_3$.

The system $\text{La}_{1-x}\text{Sr}_x\text{MnO}_3$ retains localized t^3 configurations with spin $S = 3/2$ on all the Mn atoms; in the compositional range $0.08 \leq x \leq 0.18$, the x holes/Mn atom in the σ bonding states of e -orbital parentage undergo a transition

from polaronic behavior in the canted-spin antiferromagnetic insulator phase (CAFI) to itinerant behavior in a ferromagnetic metallic (FM) phase. A combination of (1) transport measurements (thermoelectric power $\alpha(T)$ and resistivity $\rho(T)$) under hydrostatic pressure on selected single crystals^{3,5}, (2) structural studies with neutron diffraction^{3,6}, and (3) magnetic data^{3,7} in and across this compositional range have revealed that the transition from polaronic to itinerant behavior of the holes of e -orbital parentage proceeds by a series of distinguishable phases, which gives rise to a complex phase diagram. We will show here transport, magnetic, and specific-heat measurements on a series of melt-grown crystals that confirm the complex evolution of phases in the range $0.08 \leq x \leq 0.19$ and establish the atmospheric-pressure phase boundaries shown in Fig. 3.1. Extrapolation between the experimental points in Fig. 3.1 is based on the pressure studies^{3,5} that have shown discontinuous jumps in T_c where it crosses T_{JT} , a vibronic-to-metallic transition at $x \approx 0.15$, and the orthorhombic-rhombohedral transition at T_{OR} . The first order insulator-metal transition at T_{IM} was found^{3,5} to descend with increasing x to about 130 K where it ended in a phase segregation.

A colossal magnetoresistance (CMR) found^{3,8} above T_c in the compositional range $0.10 \leq x \leq 0.15$ has been modeled as a dynamic phase segregation within a paramagnetic matrix of a ferromagnetic metal (FM) phase having a T_c higher than an antiferromagnetic ordering temperature T_N of the matrix. In this model, the ferromagnetic conductive phase of higher T_c grows above T_N of the matrix in an applied magnetic field H to beyond a percolation

threshold.^{3,9} This model calls for an antiferromagnetic ordering of the matrix below T_N as in the CAFI phase and therefore a spin-glass behavior below a T_g if the orbital ordering of the matrix remains that of the O' structure.

We have measured the specific-heat and magnetization in an applied field $H = 20$ kOe in order to determine whether the spin system orders as a spin glass below a $T_g \approx T_c$ in low applied magnetic fields H and is globally transformed to ferromagnetic order in higher H fields. The specific-heat data have also allowed investigation of the prediction^{3,10} that the orbital order-disorder transition would change from second-order to first-order as T_{JT} decreases towards T_c as well as verification of the first-order character of the orbital ordering transition at T_{oo} in a narrow compositional range about $x = 0.115$.

3.2 EXPERIMENTAL PROCEDURES

Crystals of $\text{La}_{1-x}\text{Sr}_x\text{MnO}_3$ ($0 \leq x \leq 0.19$) were grown by the floating-zone method in an IR-radiation image furnace. The polycrystalline feed rods were prepared from a stoichiometric mixture of La_2O_3 , SrCO_3 , and Mn_2O_3 that had been calcined three times at 1050°C with inter-anneal grinding. The resulting powder was pressed into a rod and sintered at 1350°C for 24 h. Crystals with $0 < x \leq 0.10$ were grown in Ar; those with $x > 0.10$ were grown in flowing air. This process has been shown to yield oxygen-stoichiometric crystals close to the nominal composition.^{3,7, 3.11} As one oxygen deficiency will yield two holes while doping one Sr just gives one hole, hole concentration, which directly relates to Curie temperature T_c , is more sensitive to oxygen content than Sr doping x . If the oxygen content is expressed as $3-\delta$, a $\delta = 0.005$ has the same effect on T_c with a

change of x by 0.01, which could increase T_c by 30 K. Since the T_c vs x for our samples agreed with that of the Tokura group^{3,7}, who characterized the oxygen stoichiometry by thermogravimetric analysis (TGA), the oxygen stoichiometry in our crystals is close to nominal composition. The melt-grown rods tend to contain numerous large crystals, but independent measurements on single-crystal specimens showed no difference in the temperature dependence of the resistivity in different crystallographic directions, only a small difference in magnitude. Of interest in this study is the temperature dependence of the resistivity; it was obtained on cooling and warming by four-probe measurements made on bars cut from the melt-grown samples. The critical temperatures are more sharply defined in the melt-grown samples than in polycrystalline samples.

The specific-heat $C_p(T)$ was measured with the relaxation method.^{3,12} The instrument was calibrated by measuring $C_p(T)$ for sapphire and a high-quality single crystal of Fe_3O_4 . The DC magnetization was obtained with a SQUID (Quantum Design) magnetometer.

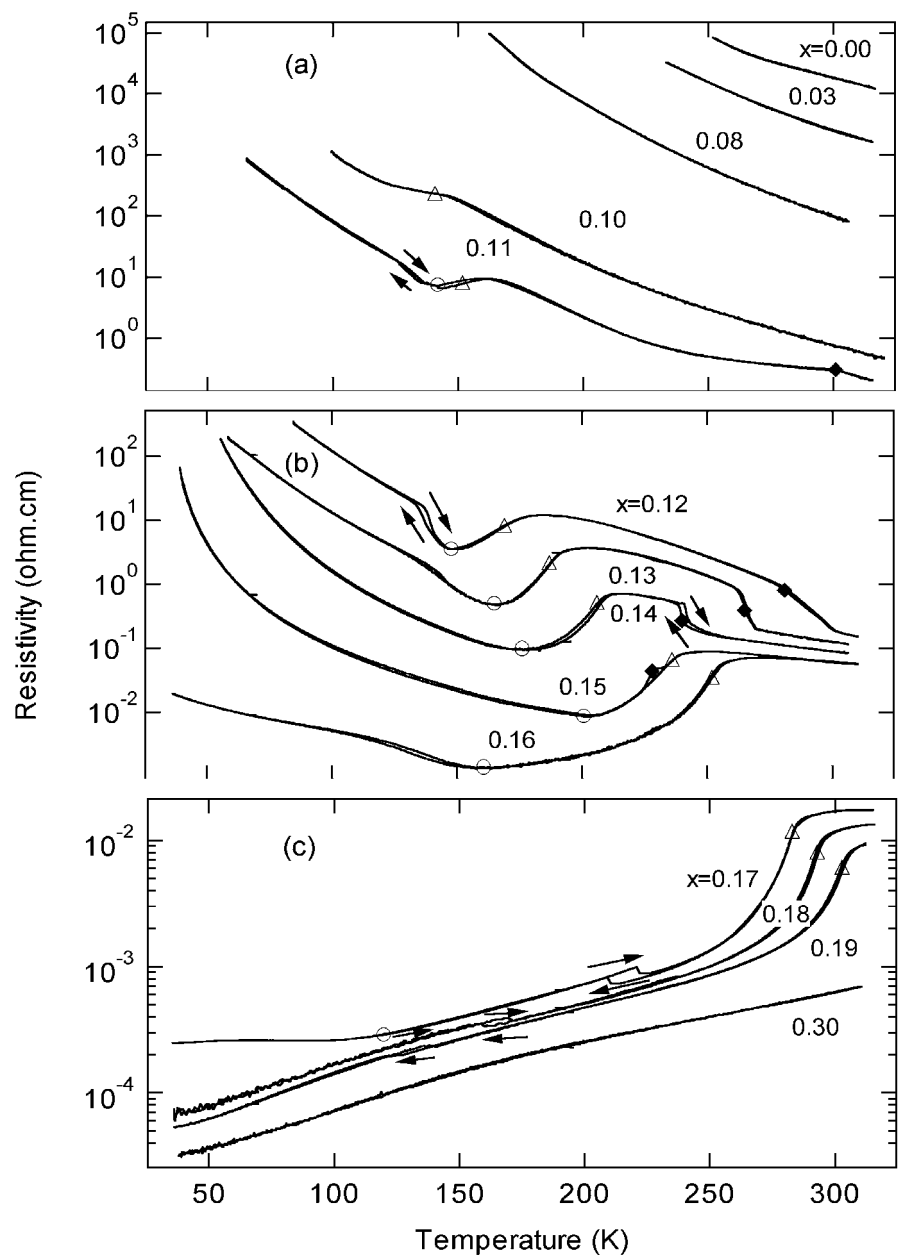


Fig. 3.2.

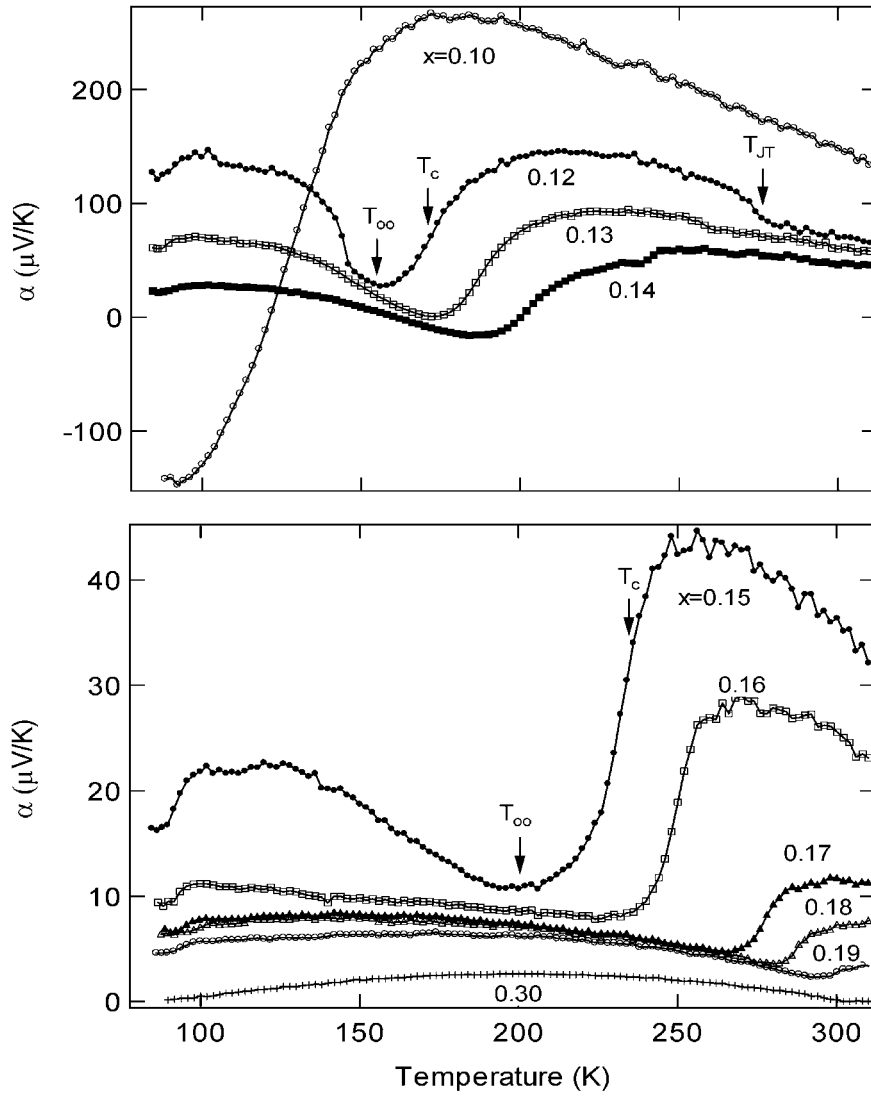


Fig. 3.2:

Resistivity $\rho(T)$ and thermoelectric power $\alpha(T)$ for melt-grown samples of $\text{La}_{1-x}\text{Sr}_x\text{MnO}_3$. Critical points: $\blacklozenge = T_{JT}$ where $|d\rho/dT|$ is a maximum; $\Delta = T_g \approx T_c$ where $d\rho/dT$ is a maximum; $\circ = T_{\infty}$ where $\rho(T)$ is a local minimum; T_{OR} = midpoint of thermal hysteresis below T_c for $0.17 \leq x \leq 0.19$. Arrows indicate heating and cooling at thermal hysteresis loops.

3.3 RESISTIVITY AND THERMOELECTRIC POWER

Fig. 3.2 shows the temperature dependence of the resistivity $\rho(T)$ and the thermoelectric power $\alpha(T)$ of the melt-grown samples. The data are consistent with those reported in the literature^{3.5, 3.7, 3.13} for melt-grown samples, but they represent finer steps in x over the entire range $0.08 \leq x \leq 0.19$. Data taken on polycrystalline samples in this range^{3.6} show no major discrepancies from those taken on melt-grown samples. The critical temperatures marked on these curves were obtained as described in the caption of Fig. 3.2. The transition from insulator to metallic conduction at low temperature in the interval $0.15 < x < 0.18$ shows that the holes are more mobile below T_{IM} than below T_{oo} and that a metallic phase dominates the low-temperature $\rho(T)$ data in the $x = 0.17$ sample, which is shown below to be electrically two-phase.

For $x = 0.12$, the $\alpha(T)$ curve shows, on cooling, a marked increase setting in below $T_{JT} \approx 280$ K, a sharp decrease occurring in the interval $T_{oo} < T < T_c$, and an abrupt increase on the crossing T_{oo} that is followed by a continued, more gradual increase to a maximum at lower temperatures. With no visible T_{JT} in the $x = 0.15$ sample, the $\alpha(T)$ curve drops abruptly on cooling through T_c but it increases on cooling through T_{oo} as in the $x = 0.12$ crystal. For the other samples, the T_{JT} , T_c , and T_{oo} temperatures on $\alpha(T)$ curves are consistent with the resistivity measurements.

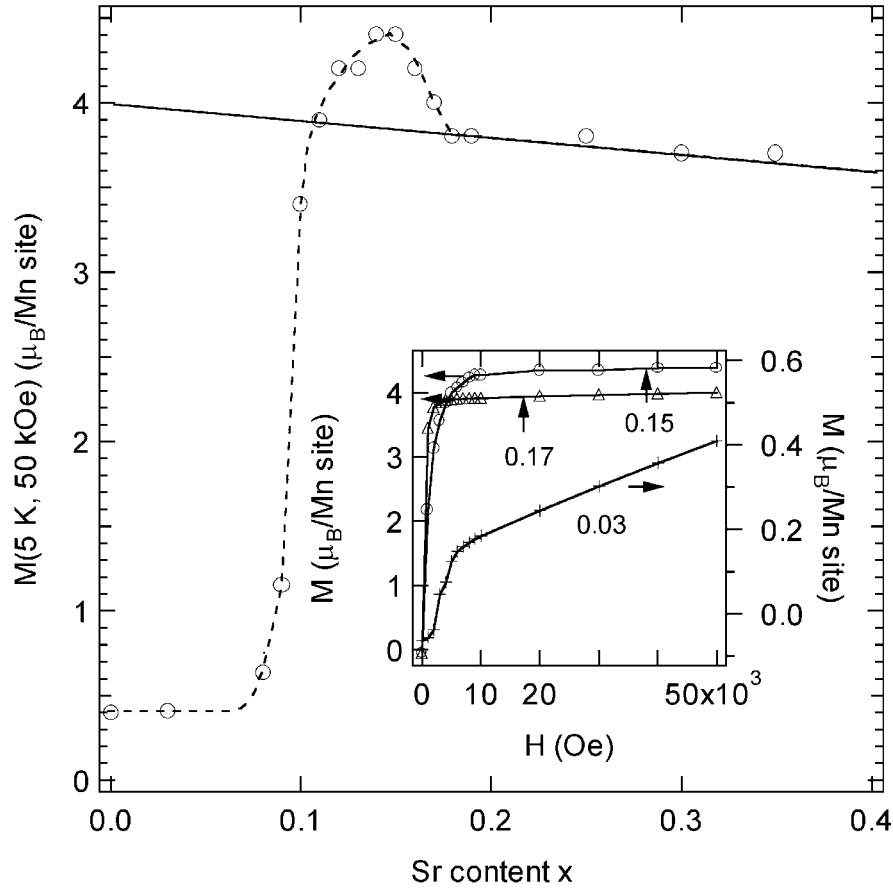


Fig. 3.3: Magnetization at 5 K in 50 kOe for $\text{La}_{1-x}\text{Sr}_x\text{MnO}_3$, $0 \leq x \leq 0.35$. Solid line: $(4-x) \mu_B/\text{Mn}$. Inset: $M(5 \text{ K})$ versus applied field H . Dashed line is a guide to the eye.

3.4 SATURATION MAGNETIZATION AT 5 K

The magnetization data of Fig. 3.3 were obtained at 5 K in a magnetic field $H = 50 \text{ kOe}$. The inset of Fig. 3.3 shows typical $M(H)$ curves. The straight line in the main figure corresponds to the theoretical spin-only value $(4-x) \mu_B/\text{Mn}$ of the magnetization for collinear-spin ferromagnetism. The rapid rise of $M(5 \text{ K}, 50 \text{ kOe})$ from that of a weak canted-spin ferromagnet below an antiferromagnetic

Néel temperature T_N to collinear-spin ferromagnetism in a modest applied field H in the interval $0.08 < x < 0.11$ represents the coexistence of ferromagnetic and antiferromagnetic regions as will become clear below; the rise in $M(5 \text{ K}, 50 \text{ kOe})$ does not represent a continuous increase in the cant angle as was predicted by de Gennes^{3,14} on the basis of a homogeneous magnetic system with itinerant e electrons in a narrow σ^* band. In the range $x > 0.18$ where the system is a ferromagnetic metal, the saturation magnetization at 5 K and 50 kOe has the theoretical spin-only value $M_s = (4-x) \mu_B/\text{Mn}$. However, an $M(5 \text{ K}, 50 \text{ kOe}) > (4-x) \mu_B/\text{Mn}$ is observed in the intermediate range $0.11 < x < 0.18$ of the orbitally ordered O'' phase, reaching a maximum value of $4.4 \mu_B/\text{Mn}$ at $x = 0.15$. A high magnetic moment ($4.2 \mu_B/\text{Mn}$) for $x = 0.15$ has also been reported without comment by others.^{3,7} This enhancement of the saturation magnetization is unique to the O'' phase of the $\text{La}_{1-x}\text{Sr}_x\text{MnO}_3$ system; it has not been observed in the $\text{La}_{1-x}\text{Ca}_x\text{MnO}_3$ system where the insulator O'' phase does not occur. Although the orbital angular momentum is quenched in lowest-order perturbation theory at both Mn^{3+} and Mn^{4+} in octahedral sites, the data indicate that where the $\text{Mn}^{3+} e$ electrons are localized, an orbital contribution to the atomic moment is introduced by higher-order terms; where the electrons of e -orbital parentage are itinerant, the orbital contribution is suppressed. The orbital contribution appears to be progressively suppressed as the hole mobility in the O'' phase increases with x in the range $0.15 < x < 0.18$.

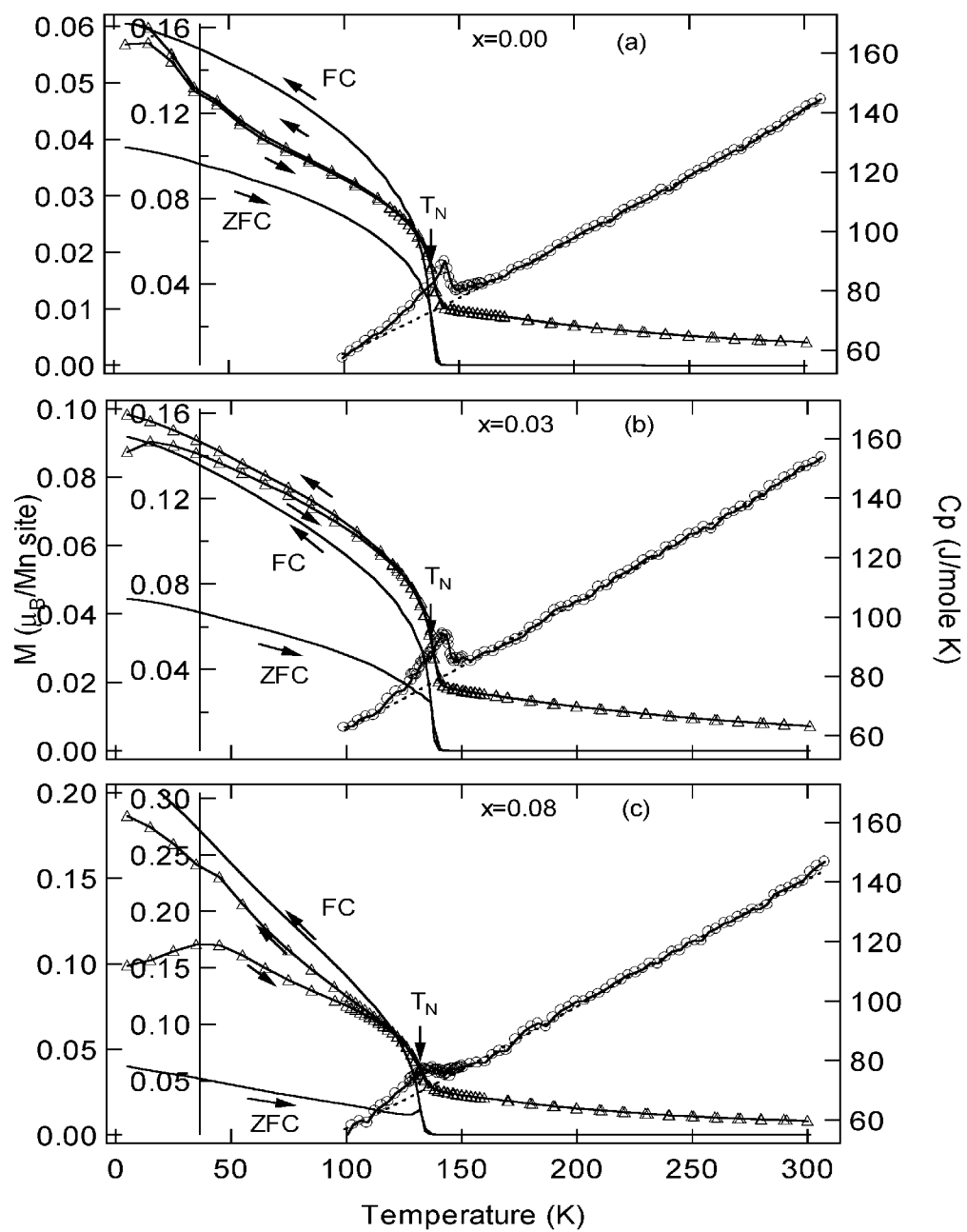


Fig. 3.4.

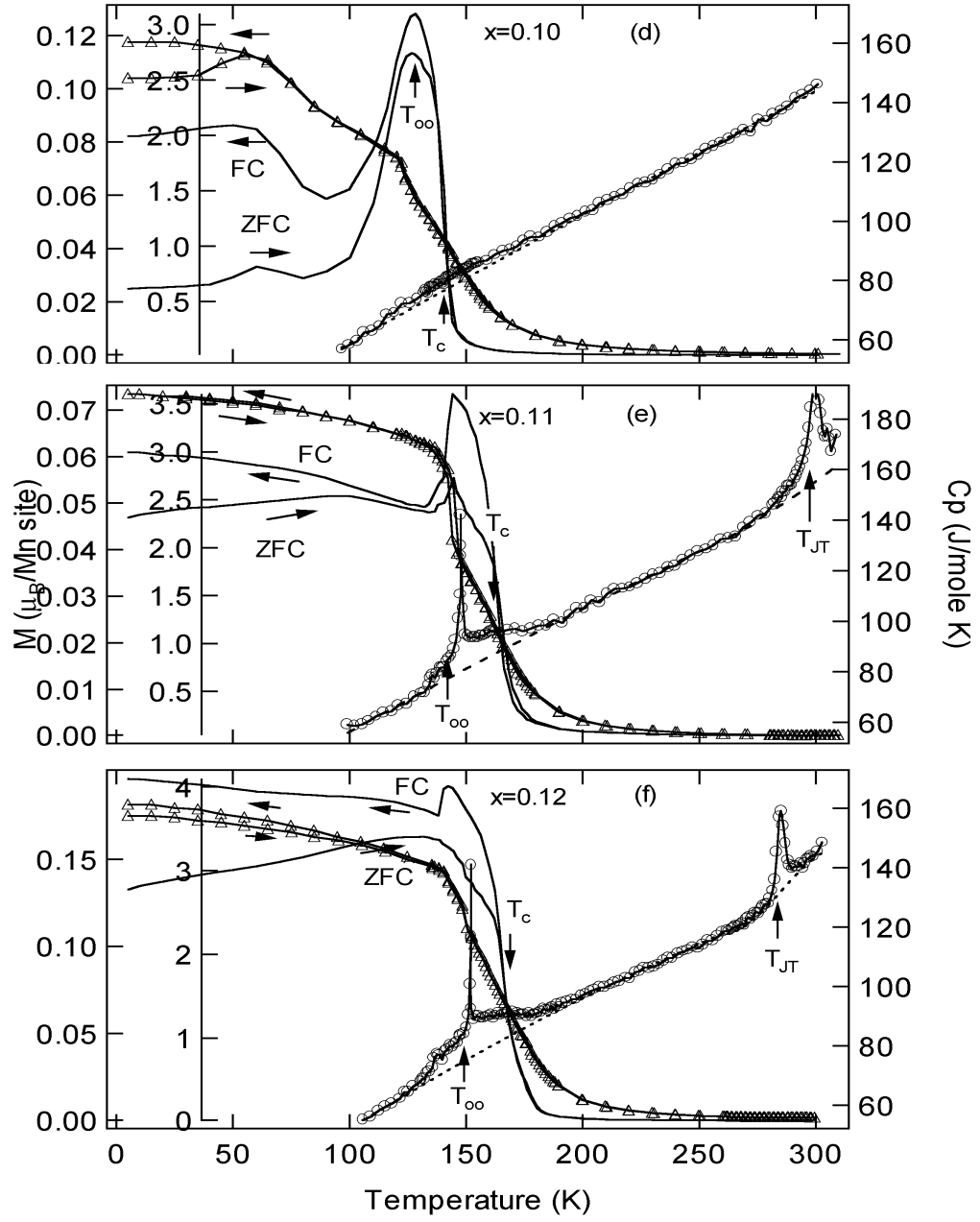


Fig. 3.4. (Continued)

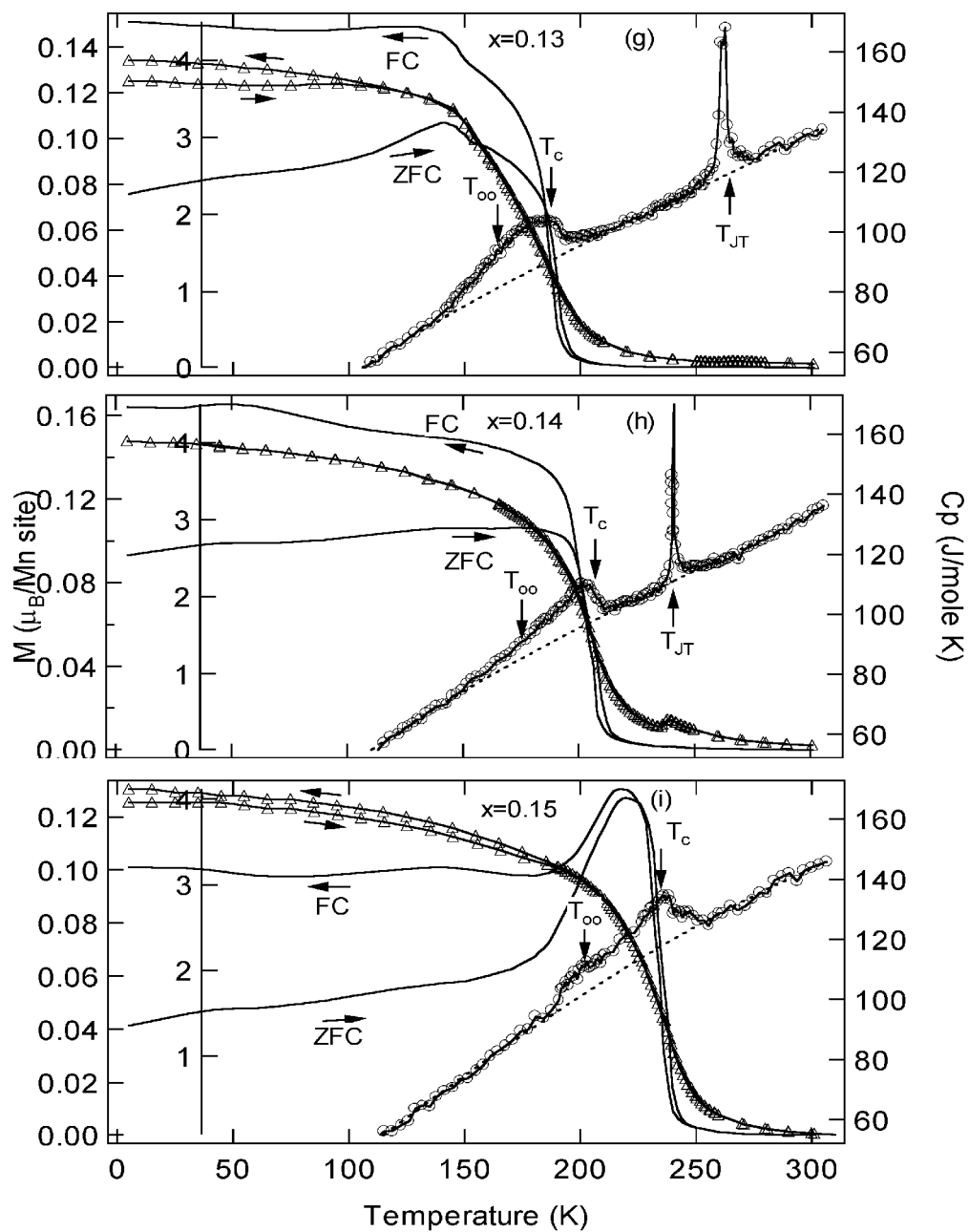


Fig. 3.4. (Continued)

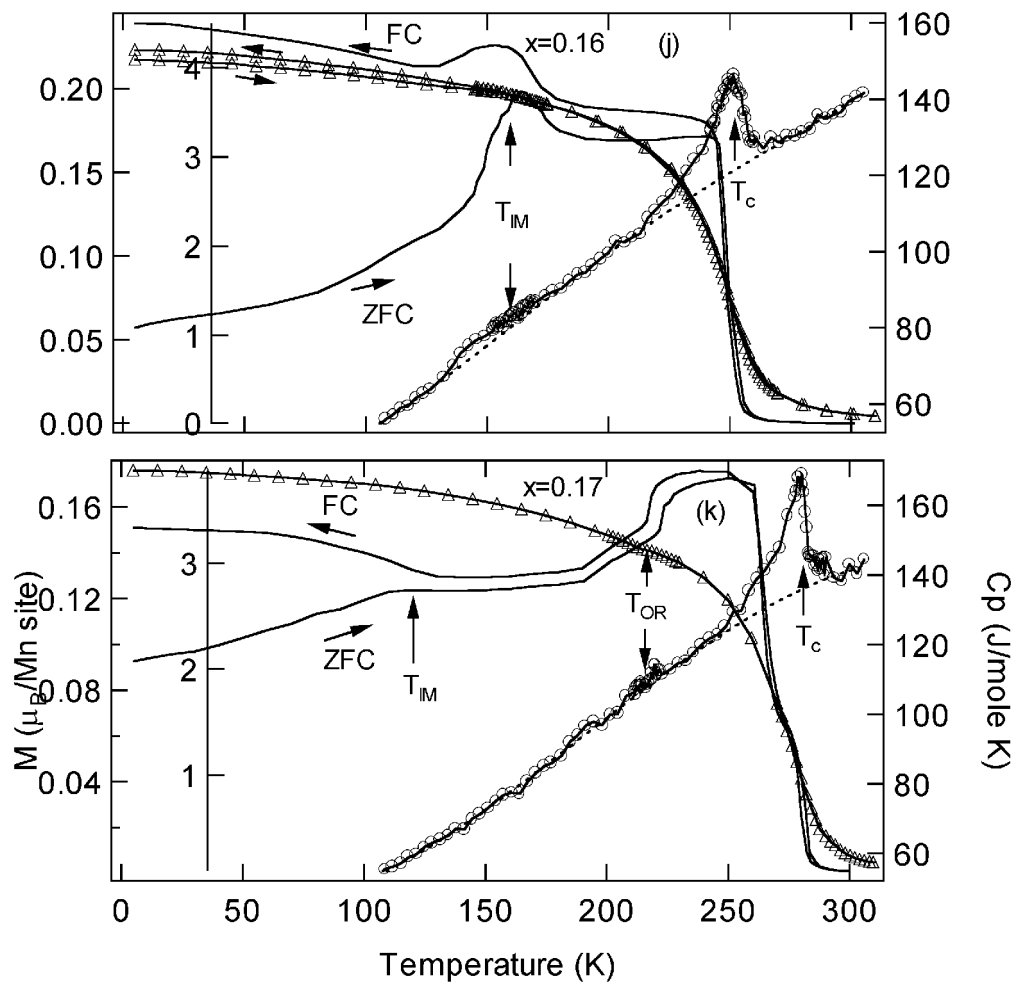


Fig. 3.4. (Continued)

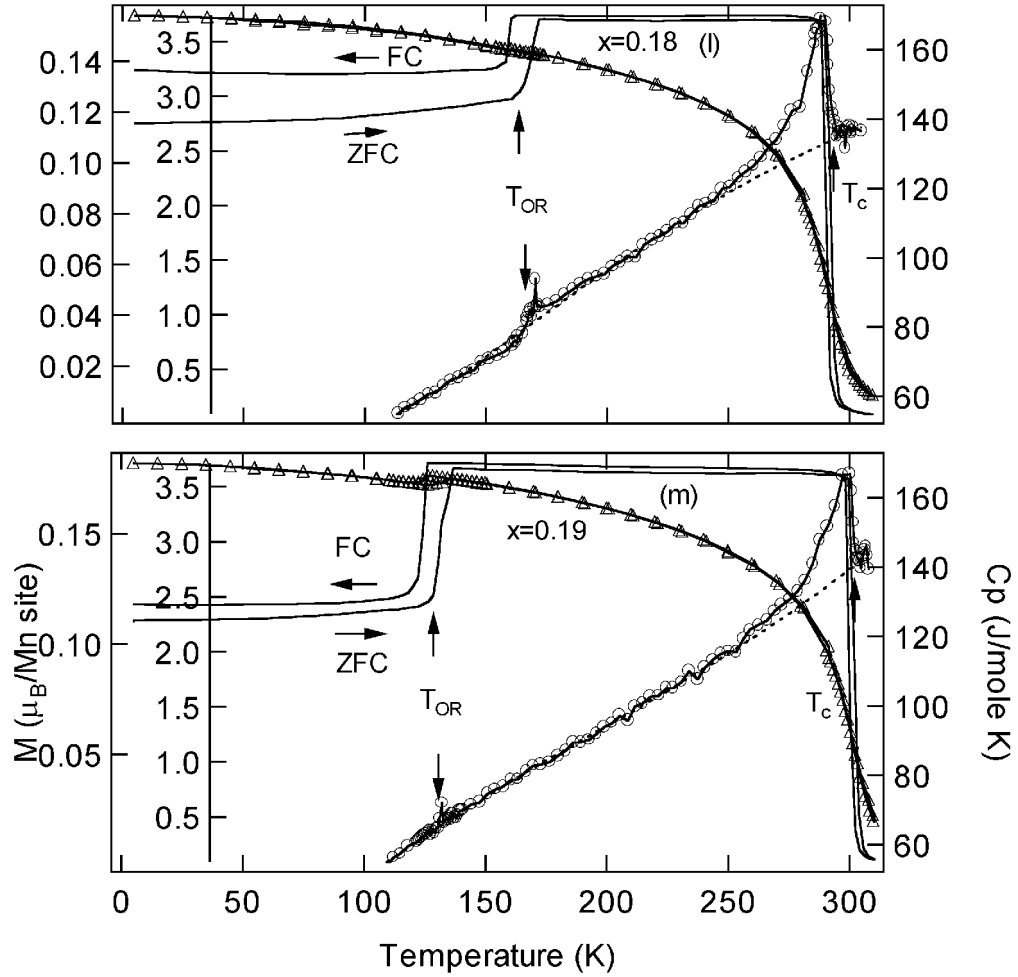


Fig. 3.4: Magnetization $M(T)$ in $H = 20$ Oe and 5 kOe; specific-heat $C_p(T)$ for $\text{La}_{1-x}\text{Sr}_x\text{MnO}_3$. O = C_p , $\Delta = M(T)$ in 5 kOe; simple solid line = $M(T)$ in 20 Oe. Arrows indicate warming vs cooling curves.

3.5 SPECIFIC-HEAT $C_p(T)$ AND MAGNETIZATION $M(T)$

Fig. 3.4 compares the specific-heat $C_p(T)$ with the magnetization $M(T)$ obtained in fields $H = 20$ Oe and 5 kOe either on heating after cooling in zero field (ZFC) or on cooling in the measuring field (FC). A correction for the

remanent field in the SQUID magnetometer was made to obtain $M(T)$ in a field as low as $H = 20$ Oe. The several critical temperatures of Fig. 3.1 are also marked by arrows in these figures; they correspond well with transitions indicated in the $C_p(T)$ and $M(T)$ data.

3.5.1 Suppressed Entropy Change at Magnetic Transition

For sample $x = 0.0$ and 0.03 of Fig. 3.4, a $T^* > 300\text{K}$ is not crossed as measurements were made for $T < 310$ K; the $x = 0.08$ sample appears to have a $T^* \approx T_N$. Therefore, the only critical temperature appearing in Figs. 3.4(a) – 3.4(c) is T_N . The $C_p(T)$ data for the $x = 0.0$ and 0.03 samples show a typical second-order anomaly at T_N , and the magnetization may be understood with a canted-spin antiferromagnetic model. However, $C_p(T)$ for the $x = 0.08$ sample has a suppressed entropy change at T_N and an anomaly characteristic of a higher-order transition. Considerable short-range magnetic order far above T_N and/or a freezing of the spins at T_N without much change in the long-range order is evident.

The $C_p(T)$ data of Fig. 3.4(d) show a suppressed entropy change at the transition temperature $T_c \geq T_{oo}$ in the $x = 0.10$ sample, and the $M(T)$ data in $H = 20$ Oe are typical of a spin glass. The enhancement of $M(T)$ below 100 K in the FC data indicates the coexistence of the CAFI phase having $T_N \approx 135$ K. In $H = 5$ kOe, the spin-glass phase is transformed into a ferromagnetic phase with a Curie temperature $T_c \approx T_g$, but the CAFI phase remains unchanged to give an enhancement of $M(T)$ below 100 K. The coexistence of the CAFI phase keeps $M(5\text{ K}, 50\text{ kOe})$, Fig. 3.3, below the theoretical spin-only value. The data thus provide clear evidence of the coexistence of two magnetic phases, one

corresponding to the CAFI phase and the other to a peculiar phase that is a spin glass in low magnetic fields and is transformed into a ferromagnetic phase in an applied field $H = 5$ kOe. Evidence for the CAFI phase does not appear in the $H = 20$ Oe $M(T)$ data of Fig. 3.4(e) for $x = 0.11$, but a spin glass appears below $T_g \approx T_c$ as in the $x = 0.10$ sample; the transition at $T_{oo} < T_c$ is clearly first order.

A spin glass would occur where an antiferromagnetic matrix ordering below its $T_N = T_g$ contains within it a volume of FM phase that is below its percolation limit and has a $T_c(FM) > T_g$. In the manganese-oxide perovskites, the FM phase is hole-rich, the matrix is hole poor.^{3,9} The concentration of holes within a FM volume exceeds $x = 0.15$. Interpretation of the magnetic and transport data requires a distinction be made between what happens when a field H is applied above T_g where the samples are paramagnetic and the phase transition that occurs on application of a modest $H = 5$ kOe below T_g . At paramagnetic temperatures $T_g < T < T_c(FM)$, the FM phase grows beyond its percolation threshold in a large H , and the CMR phenomenon reflects the greater conductivity of the FM phase. The application of an H below T_g , on the other hand, induces a global transformation of the antiferromagnetic matrix of the spin glass to a ferromagnetic phase in which the holes trapped in the FM clusters become released as two-manganese Zener polarons.^{3,5}

3.5.2 O' Phase – O^* Phase Transition

We can understand such a global magnetic phase transition if we recognize that 3D ferromagnetic Mn^{3+} -O- Mn^{3+} superexchange interactions occur where the cooperative, local Jahn-Teller deformations fluctuate;^{3,15} static Jahn-

Teller deformations give rise to antiferromagnetic t^3 -O- t^3 superexchange interactions in at least one direction, as occurs in the O' phase along the c -axis. Stabilization of 3D relative to 2D ferromagnetic interactions in an applied magnetic field H would involve transforming orbital ordering in an O' matrix into 3D orbital fluctuations in an O^* matrix. Orbital disorder introduces a ferromagnetic vibronic Mn^{3+} -O- Mn^{3+} superexchange interaction in which the dominant virtual electron transfer is from a half-filled e orbital on one atom to an empty e orbital on neighbor. Evidence that an applied H stabilizes an O^* relative to an O' matrix in the interval $T^* < T < T_{JT}$ even in the paramagnetic phase is found in a report by Uhlenbruck *et al*^{3,16} that T_{JT} is lowered and T_c is raised in an $H = 140$ kOe in an $x = 0.125$ sample. Our data show similar, but smaller, shifts of T_{JT} and T_c in an $H = 50$ kOe.

The O^* - O' transition at T_c is unusual in another respect since the higher-temperature phase has the greater orbital order along with a greater magnetic disorder. In a magnetic field, magnetic ordering below T_c is accompanied by long-range orbital disorder in the narrow temperature interval $T_{oo} < T < T_c$; in this interval, there is a transition to a different long-range orbital ordering below T_{oo} . Therefore, it should not be surprising that the application of an H below T_c is able to disrupt the long-range orbital ordering with 2D orbital fluctuations that occurs in the O' phase above T_c .

3.5.3 Transition at T_{JT}

In the compositional range $0.11 \leq x \leq 0.14$, a $T_c < T_{JT} < 310\text{K}$ gives a conspicuous anomaly in $C_p(T)$ at T_{JT} . The data of Figs. 3.4(e) – 3.4(h) show a

clear evolution from a second-order to a first-order transition as T_{JT} is lowered. Rozenberg *et al*^{3,10} have predicted a similar change should occur at a transition from localized to itinerant electronic behavior; the e electrons are localized or confined to two-manganese polarons for $T < T_{JT}$, but they approach an itinerant character at $T > T_{JT}$ as x approaches $x = 0.15$; for $x = 0.15$, a first-order vibronic-metal transition occurs.

3.5.4 O^* Phase – O'' Phase Transition

In agreement with the conductivity data of Fig. 3.2, $C_p(T)$ shows that the transition at T_{oo} is first-order in the $x = 0.11$ and $x = 0.12$ samples, but is similar to a glass transition in the other compositions. Apparently long-range order of the occupied e orbitals sets in at T_{oo} in only a narrow range of compositions $0.11 \leq x \leq 0.12$; in the O'' compositions away from this range, the orbital ordering that occurs on cooling through T_{oo} consists of considerable short-range order in the spin-glass or FV phase and retains short-range fluctuations well below the long-range orbital-ordering temperature T_{oo} . Fig. 3.4(f), 3.4(g) show a peculiar enhancement of $M(T)$ in a finite temperature interval below T_{oo} in a field $H = 20$ Oe. From the $C_p(T)$ data, the enhancement occurs where the entropy is changing sharply with temperature on crossing an order-disorder transition. A similar enhancement of $M(T)$ in $H = 20$ Oe can be seen in Fig. 3.4(j) at T_{IM} of the $x = 0.16$ sample. The transitions at both T_{oo} and T_{IM} are from one magnetic phase to another, and the crystalline anisotropy can be expected to decrease in the two-phase transition region. A reduced crystalline anisotropy would give a stronger response of the magnetic system to a weak $H = 20$ Oe applied field.

The $M(T)$ curves for $H = 5$ kOe in Figs. 3.4(d)–3.4(f) show a sharp increase on cooling through the orbital order-disorder transition at T_{oo} ; this increase is particularly marked at the first-order transition in the $x = 0.11$ sample. The orbital ordering of the O'' phase clearly favors 3D ferromagnetic interactions in lower magnetic fields. Moreover, as x increases, the concentration and mobility of the ferromagnetically coupled Zener polarons increases near T_c , which strengthens the ferromagnetic double-exchange component of the magnetic interactions. Consequently, T_c increases and the transition at T_c becomes less glasslike; by $x = 0.16$, a typical second-order anomaly in $C_p(T)$ is found at T_c . The $x = 0.15$ sample is at the cross-over from vibronic to itinerant electronic behavior below T_c and near the convergence of T_{JT} and T_c . Consequently the entropy change at T_c suggests the coexistence of a vibronic and a metallic ferromagnetic phase.

3.5.5 O^* Phase – R Phase Transition

Fig 3.4(k) shows two distinguishable Curie temperatures for the $x = 0.17$ phase; they appear to represent the coexistence of the O^* and R phases and the discontinuity in T_c that occurs at the transition from the O^* to the R phase. The O^* - R transition at $T_{OR} < T_c$ within the phase of higher T_c is only weakly visible in the $C_p(T)$ trace; it is more clearly marked by a drop in $M(T)$ taken with $H = 20$ Oe. The step in the $H = 20$ Oe $M(T)$ curves, which show a thermal hysteresis in $M(T)$ for FC and ZFC in $H = 20$ Oe as in the resistivity curves of Fig. 3.2, is clearly associated with a weakly first-order transition at $T_{OR} < T_c$ in the $x = 0.18$ and 0.19 samples in Figs. 3.4(l), 3.4(m). In Figs. 3.4(k) – 3.4(m), the $C_p(T)$ anomalies at T_c

are typical of second-order magnetic transitions. On the other hand, a small thermal hysteresis at T_c suggests some first-order character may accompany a transition from itinerant character below T_c to polaronic conduction above T_c (see Fig. 3.2). It is interesting that the ZFC and FC $M(T)$ curves for $H = 20$ Oe in Fig. 3.4(k) for $x = 0.17$ diverge below T_{IM} . This divergence is consistent with a glassy character of the spins in zero applied field in the O'' phase.

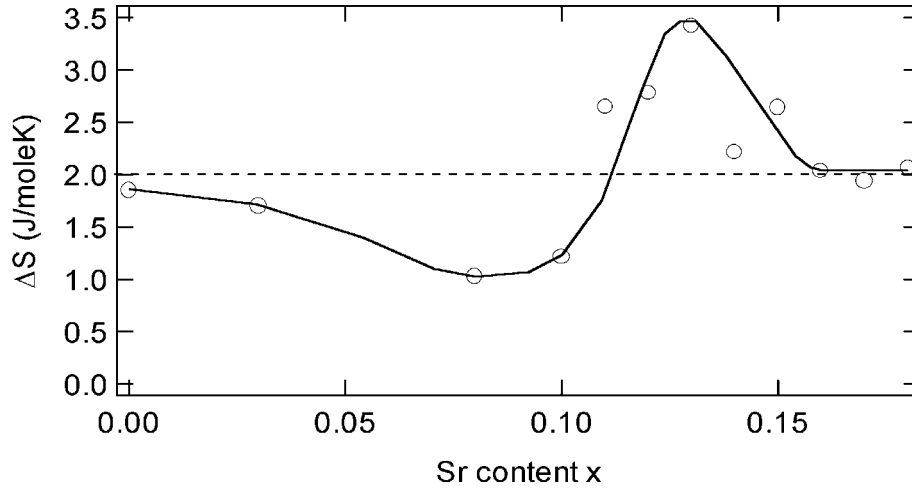


Fig. 3.5: Entropy change ΔS at T_N , T_c and T_{oo} , or T_c obtained from area of $C_p(T)/T$ after subtraction of background. Solid line is guide to the eye.

3.5.6 Calculated Entropy Change at T_N and T_c

Fig. 3.5 shows a plot of the entropy change ΔS obtained for T_N and T_c , T_{oo} after subtracting out the background (dashed line in Fig. 3.4) determined by fitting with polynomials. The value of ΔS obtained for T_N in the $x = 0.00$ and 0.03 samples approaches the value of 2 J/mole K typically found^{3,17} for a second-order transition in these perovskites, as does also ΔS at T_c for $0.16 \leq x \leq 0.18$.

However, ΔS is suppressed to half this value at $x = 0.08$, which is indicative of a considerable volume of ferromagnetic short-range order far above T_N and of spins freezing without much change in the long-range order at T_N ; the ferromagnetic volume is manifest in a larger $M(5\text{ K}, 50\text{ kOe})$ than expected for canted-spin ferromagnetism alone (Fig. 3.3). A contribution from the orbital order-disorder transition at $T_{oo} < T_g$ prevents observation of an even lower ΔS for the magnetic transition at T_g in the $x = 0.10$ sample. The orbital order-disorder and disorder-order transitions at T_{oo} and T_c , respectively, make major contributions to ΔS in samples $0.12 \leq x \leq 0.15$.

3.4 SUMMARY AND CONCLUSION

Measurements of resistivity $\rho(T)$, thermoelectric power $\alpha(T)$, specific-heat $C_p(T)$, magnetization $M(T)$ in applied magnetic fields $H = 20\text{ Oe}$, 5 kOe and magnetization at 5 K up to 50 kOe have confirmed the complex phase diagram below 310 K of the system $\text{La}_{1-x}\text{Sr}_x\text{MnO}_3$ in the range $0.0 \leq x \leq 0.35$ that has been deduced from magnetic and high-pressure transport data, structural experiments, and measurements made on individual samples by several groups. In the compositional range $0.08 \leq x \leq 0.18$, the electrons in σ -bonding orbitals undergo a transition from localized behavior in a canted-spin antiferromagnetic insulator (CAFI) with a static, cooperative Jahn-Teller orbital ordering to itinerant-electron behavior in a ferromagnetic metal (FM). We have identified a spin-glass phase appearing in low applied magnetic fields between the CAFI and FM phases where the CMR phenomenon is found. The data allow a distinction to be made between growth in an applied field H of a FM minority phase in a

paramagnetic matrix in the interval T_g (or T_c) $< T < T_{JT}$ and the phase transformation from a spin-glass to a ferromagnetic vibronic (FV) phase on application of an $H = 5$ kOe below $T_g \approx T_c$. The former is responsible for the CMR phenomenon; the latter represents stabilization in a magnetic field of an orbital disordering that is compatible with 3D ferromagnetic interactions relative to an orbital ordering that gives some antiferromagnetic interactions. As the Weiss molecular field of the ferromagnetic phase increases with T_c in the compositional range $0.10 \leq x \leq 0.15$, the glassy character of the transition at $T_g \approx T_c$ decreases. Steps in T_c occur at the first-order vibronic-itinerant electronic transition at $x = 0.15$ and the $O^* - R$ transition at $x = 0.17$. Moreover, the orbital disorder to order transition on cooling through T_{JT} was shown to change from second-order to first-order as T_{JT} decreases to T_c at the transition from vibronic to itinerant electronic behavior at $x = 0.15$. The magnetization $M(5 \text{ K}, 50 \text{ kOe})$ is greater than the spin-only value $(4-x) \mu_B/\text{Mn}$ in the FI phase below T_{oo} , reaching $4.4 \mu_B/\text{Mn}$ at $x = 0.15$, but it has the spin-only value in the FM phase. An orbital moment adds to $M(T)$ where the e electrons are localized; itinerant electrons do not contribute an orbital component to the atomic magnetic moment.

The first-order transition at T_{IM} in the narrow range $0.15 \leq x \leq 0.17$ appears to be an extension of T_{JT} , paramagnetism giving the orbital order of the O' phase below T_{JT} and ferromagnetism giving the orbital order of the O'' phase below T_{IM} . At the transition from localized to itinerant behavior of the electrons of e -orbital parentage, the system exhibits two intermediate configurations: one is a dynamic segregation of a FM phase within a CAFI matrix and the other is the

retention of dispersed two-manganese Zener polarons that preferentially order their axes along an $[001]$ axis in the O'' phase. Below T_{IM} the Zener polarons are more mobile than below T_{oo} . In the narrow temperature range $T_{oo} < T < T_g \approx T_c$, the orbital ordering in the matrix of the O' phase gives antiferromagnetic interactions along the $[001]$ axis and, therefore, frustrates the interactions between the ferromagnetic clusters to a spin glass. Dispersal of the Zener polarons favors 3D ferromagnetic interactions and a short-range orbital ordering that becomes progressively long-range ordered on cooling through T_{oo} . As T_c increases and T_{JT} decreases with increased hole concentration x , stabilization of orbital order in the matrix below T_c is reduced, so the glassy character of the transition at $T_g \approx T_c$ is reduced. The polaronic-itinerant electronic transition at T_{IM} occurs below T_c , a polaronic-polaronic transition at T_{JT} occurs in the paramagnetic phase above T_c . This peculiar competition between orbital, charge, and magnetic order occurs in the compositional range between where T^* falls below T_N in Fig. 3.1 and T_{JT} , T_{IM} .

Chapter 4: The $\text{La}_{1-x}\text{Ca}_x\text{MnO}_3$ system

In the previous chapter, we discussed the properties of the $\text{La}_{1-x}\text{Sr}_x\text{MnO}_3$ (LSMO) system; in this chapter, we will study a similar system, $\text{La}_{1-x}\text{Ca}_x\text{MnO}_3$ (LCMO). They have similar structure, transport and magnetic properties. However, because Ca^{2+} has a smaller ionic radius than Sr^{2+} , $\text{La}_{1-x}\text{Ca}_x\text{MnO}_3$ has a smaller tolerance factor, which causes these two systems to differ in several aspects. For a deeper understanding of $\text{Ln}_{1-x}\text{A}_x\text{MnO}_3$ family in which Ln is a lanthanide and A an alkaline-earth atom, a comparison between them is needed.

4.1 EXPERIMENTAL PROCEDURES

Crystals of $\text{La}_{1-x}\text{Ca}_x\text{MnO}_3$ were grown by the floating-zone method in an IR-radiation image furnace. The polycrystalline feed rods were prepared from a stoichiometric mixture of La_2O_3 , CaCO_3 , and Mn_2O_3 that had been calcined three times at 1050 °C with inter-anneal grinding. The resulting powder was pressed into a rod and sintered at 1350 °C for 24 hours. With x less than 0.25, the rod could be melted congruently in a flow of air; with x greater than 0.25, it was melted in a flow of O_2 . This process has been shown to yield oxygen-stoichiometric crystals close to the nominal composition. The melt-grown rods tend to contain numerous large crystals, but independent measurements on single-crystal specimens showed no difference in the temperature dependence of the resistivity in different crystallographic directions, only a small difference in magnitude. Of interest in this study is the temperature dependence of the

resistivity; it was obtained on cooling and warming by four-probe measurements made on bars cut from the melt-grown samples. The critical temperatures are more sharply defined in the melt-grown samples than in polycrystalline samples.

The specific-heat $C_p(T)$ was measured with the relaxation method. The instrument was calibrated by measuring $C_p(T)$ for sapphire and a high-quality single crystal of Fe_3O_4 . The DC magnetization was obtained with a SQUID (Quantum Design) magnetometer.

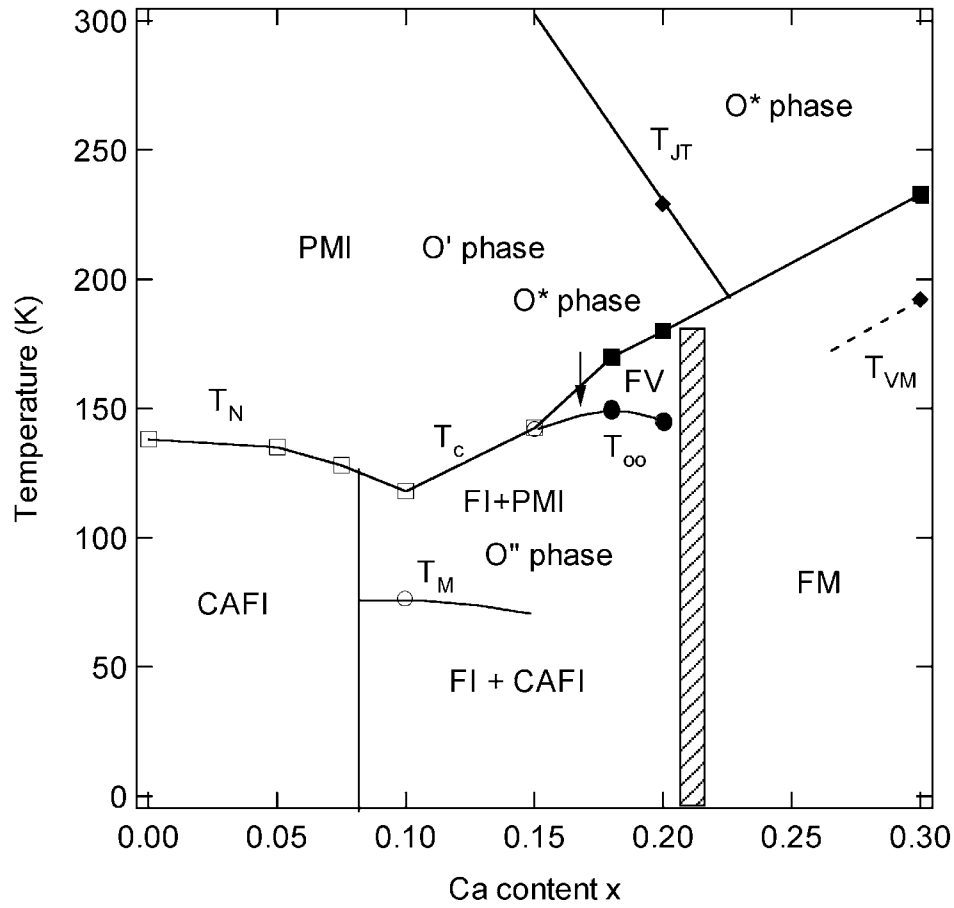


Fig. 4.1: Phase diagram of $\text{La}_{1-x}\text{Ca}_x\text{MnO}_3$ system. The open rectangle and circle are from low field (20 Oe) magnetization; the filled rectangle and circle are from resistivity; the filled diamond is from a specific-heat measurement. The T_c and T_{oo} are after reference.^{4,6} The shade zone is two phase region.

4.2 PHASE DIAGRAM

At present, the phase diagram of the $\text{La}_{1-x}\text{Ca}_x\text{MnO}_3$ system is still quite controversial among researchers.^{4.1, 4.2, 4.3} The property of some phase transitions has remained unclear. Fig. 4.1 shows a tentative phase diagram of the $\text{La}_{1-x}\text{Ca}_x\text{MnO}_3$ system. The $O'-O^*$ transition temperature T_{JT} decreases sharply from

750 K (LaMnO_3) with increasing x in the range $0 \leq x \leq 0.21$. The O' phase ($c/a < \sqrt{2}$) has cooperative orbital ordering of the occupied e orbital at the Mn^{3+} ions into the (001) planes; the O^* phase has $c/a \approx \sqrt{2}$ and is pseudocubic, but the MnO_6 octahedra are rotated 20° about the b -axis relative to the ideal cubic-perovskite structure; locally cooperative, dynamic Jahn-Teller distortions sustain a ($c/a \approx \sqrt{2}$). On cooling through T_c in the range $0.1 \leq x \leq 0.15$, there is a phase transition from paramagnetic insulator (PI) to ferromagnetic insulator (FI); in the range $0.15 \leq x \leq 0.21$, the transition at T_c is from a PI to a ferromagnetic vibronic (FV) phase in which the conductivity shows bad metallic behavior. In the $\text{La}_{1-x}\text{Sr}_x\text{MnO}_3$ system, the FV phase is found in the range $0.1 \leq x \leq 0.15$ (see LSMO phase diagram in Chapter 3). If x falls between 0.2 and 0.3, the material is in a ferromagnetic metallic (FM) phase below T_c . The metal-insulator (MI) transition below T_c is around $x_c = 0.22$. This value is larger than that in the $\text{La}_{1-x}\text{Sr}_x\text{MnO}_3$ system in which the x_c is about 0.15. In the range $0.1 \leq x \leq 0.2$, a transition from FI to a mixture of FI and canted anti-ferromagnetic insulator (CAFI) happens at about $T_M \approx 80$ K (open circle). This transition corresponds to a minimum point of the zero-field-cooled (ZFC) low-field magnetization vs temperature curve. This minimum point was also observed in $\text{La}_{0.8}\text{Ca}_{0.2}\text{MnO}_3$ by other researchers.^{4,4} On this phase diagram, we can not see the R phase. This is because the temperature of the transition from the R phase to the O^* phase is 700 K to 1000 K,^{4,5} which is beyond the range of this phase diagram. This T_{OR} temperature is different from that of the $\text{La}_{1-x}\text{Sr}_x\text{MnO}_3$ system in which T_{OR} is below 300 K for $x > 0.17$. Discontinuities in T_c and T_{JT} probably occur at their crossover as in the La_{1-x}

$x\text{Sr}_x\text{MnO}_3$ system, but this crossover was not examined in the $\text{La}_{1-x}\text{Ca}_x\text{MnO}_3$ system.

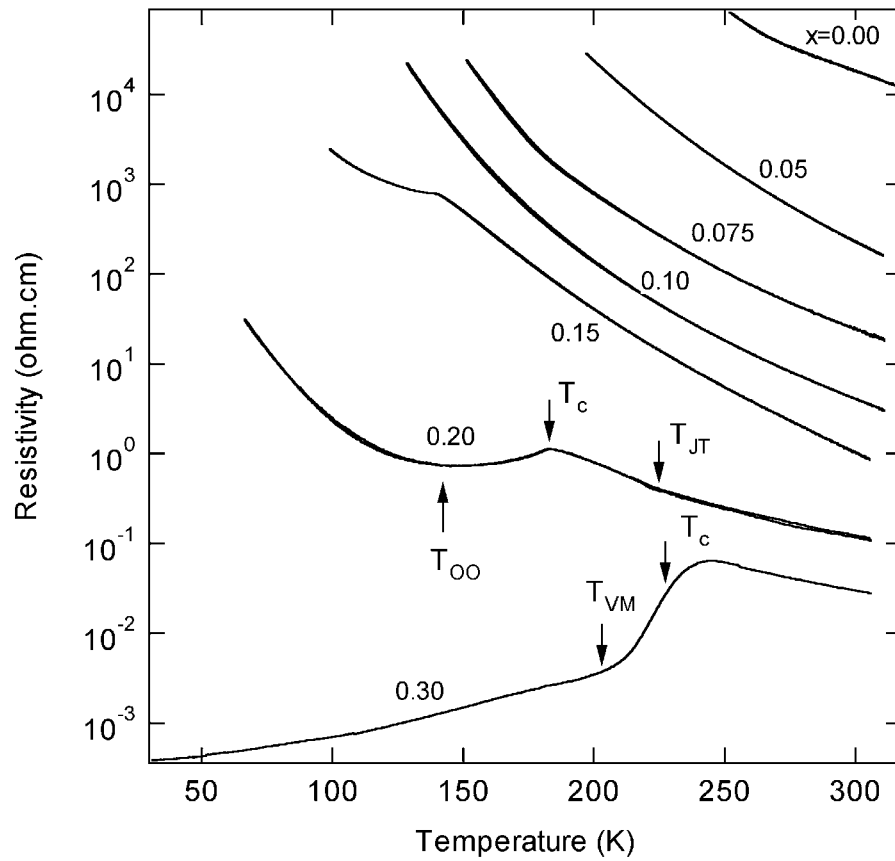


Fig. 4.2: Resistivity versus temperature for melt-grown samples of the $\text{La}_{1-x}\text{Ca}_x\text{MnO}_3$ system.

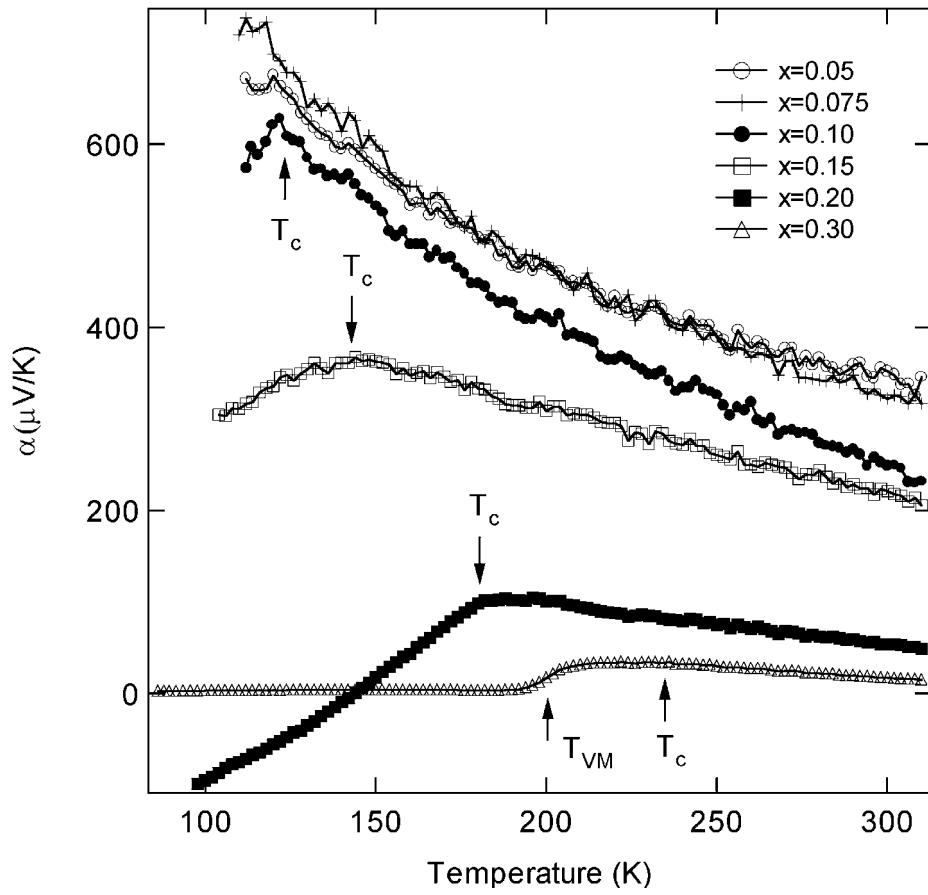


Fig. 4.3: Thermoelectric power versus temperature for melt-grown samples of the $\text{La}_{1-x}\text{Ca}_x\text{MnO}_3$ system.

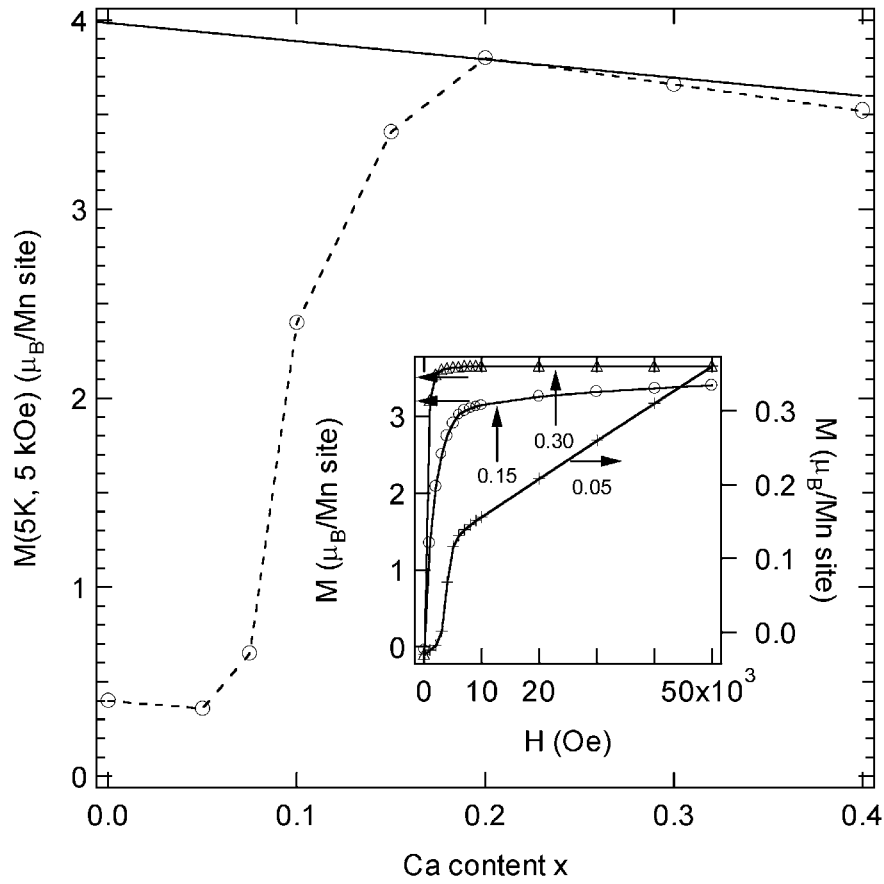


Fig. 4.4: Magnetization at 5 K in 50 kOe for $\text{La}_{1-x}\text{Ca}_x\text{MnO}_3$, $0 \leq x \leq 0.4$. Solid line: $(4-x) \mu_B/\text{Mn}$. Inset: $M(5 \text{ K})$ versus applied field. Dashed line is a guide to the eye.

4.3 RESISTIVITY, THERMOELECTRIC POWER, AND MAGNETIZATION

Fig. 4.2 shows the resistivity vs. temperature for $\text{La}_{1-x}\text{Ca}_x\text{MnO}_3$. Fig. 4.3 shows the thermoelectric power $\alpha(T)$ curve. The data are consistent with those reported in the literature.^{4.4, 4.6-4.9} In the range $0.0 \leq x \leq 0.10$, the resistivity shows insulator behavior over the entirely measured temperature range and the thermoelectric power shows a progressive trapping out of the polaronic charge

carriers with decreasing temperature with no change at T_N , Néel temperature. For $x = 0.30$, the resistivity shows metallic behavior below T_c . The thermoelectric power of Fig. 4.3 shows no change on cooling through T_c , but a drop to a small value, varying linearly with T occurs on cooling through T_{VM} , which appears to mark a transition from vibronic to metallic behavior. Samples $x = 0.15$ and 0.20 , on the other hand, show a decrease in the resistivity $\rho(T)$, followed by a smooth rise on cooling through T_c . The upturn in $\rho(T)$ on cooling below T_c is consistent with a transition from ferromagnetic vibronic (FV) to a FI phase at a T_{oo} as found in the $\text{La}_{1-x}\text{Sr}_x\text{MnO}_3$ system for $0.10 \leq x \leq 0.12$.^{4,10, 4.11} In these samples, the thermoelectric $\alpha(T)$ of Fig. 4.3 has a maximum value at T_c characteristic of a change from polaronic to vibronic conductivity in a percolating ferromagnetic phase coexisting with the CAFI phase. Evidence for the co-existence of two magnetic phases in the range $0.075 \leq x \leq 0.20$ comes from several sources. For example, Dai *et al*^{4.8} concludes from neutron-scattering data that the resistivity in this compositional range is controlled by a competition between short-range localized-electron fluctuations and long-range ferromagnetic double-exchange interactions. The magnetization data of Fig. 4.4 provide further evidence for the coexistence of a CAFI phase within a percolating ferromagnetic phase. The magnetization data of Fig. 4.4 were obtained at 5 K in a magnetic field of $H = 50$ kOe. The inset of Fig. 4.4 shows typical $M(H)$ curves. The straight line in the main figure corresponds to the theoretical spin-only value $M_s = (4 - x) \mu_B/\text{Mn}$ of the magnetization for collinear-spin ferromagnetism. The rise of $M(5 \text{ K}, 50 \text{ kOe})$ from that of a weak canted-spin ferromagnet below an anti-ferromagnetic Néel

temperature T_N to collinear-spin ferromagnetism in an applied field H in the interval $0.075 < x < 0.2$ represents the coexistence of ferromagnetic and anti-ferromagnetic regions. In the range $x \geq 0.2$ where the system is a ferromagnetic metal, the saturation magnetization at 5 K and 50 kOe has the theoretical spin-only values $M_s = (4 - x) \mu_B/\text{Mn}$. There is no magnetic moment higher than the spin-only values observed in this $\text{La}_{1-x}\text{Ca}_x\text{MnO}_3$ system. However, a magnetization higher than the spin-only value is observed in the $\text{La}_{1-x}\text{Sr}_x\text{MnO}_3$ system in a single FI phase. The insulating $\text{La}_{0.85}\text{Ca}_{0.15}\text{MnO}_3$ and $\text{La}_{0.80}\text{Ca}_{0.20}\text{MnO}_3$ samples do not develop single-phase orbital ordering as occurs in $\text{La}_{0.88}\text{Sr}_{0.12}\text{MnO}_3$ where the extra magnetic moment is attributed to the orbital contribution.

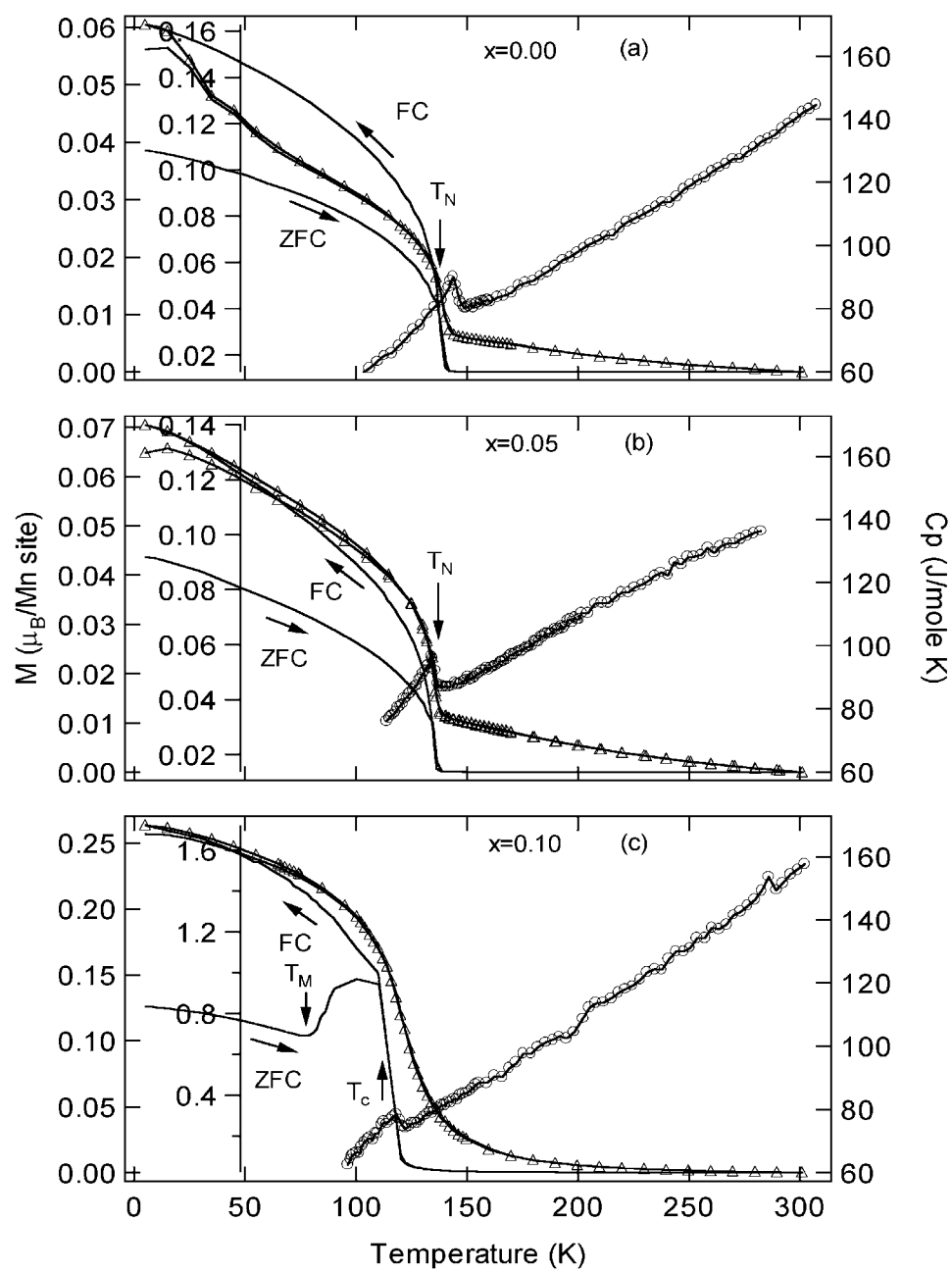


Fig. 4.5.

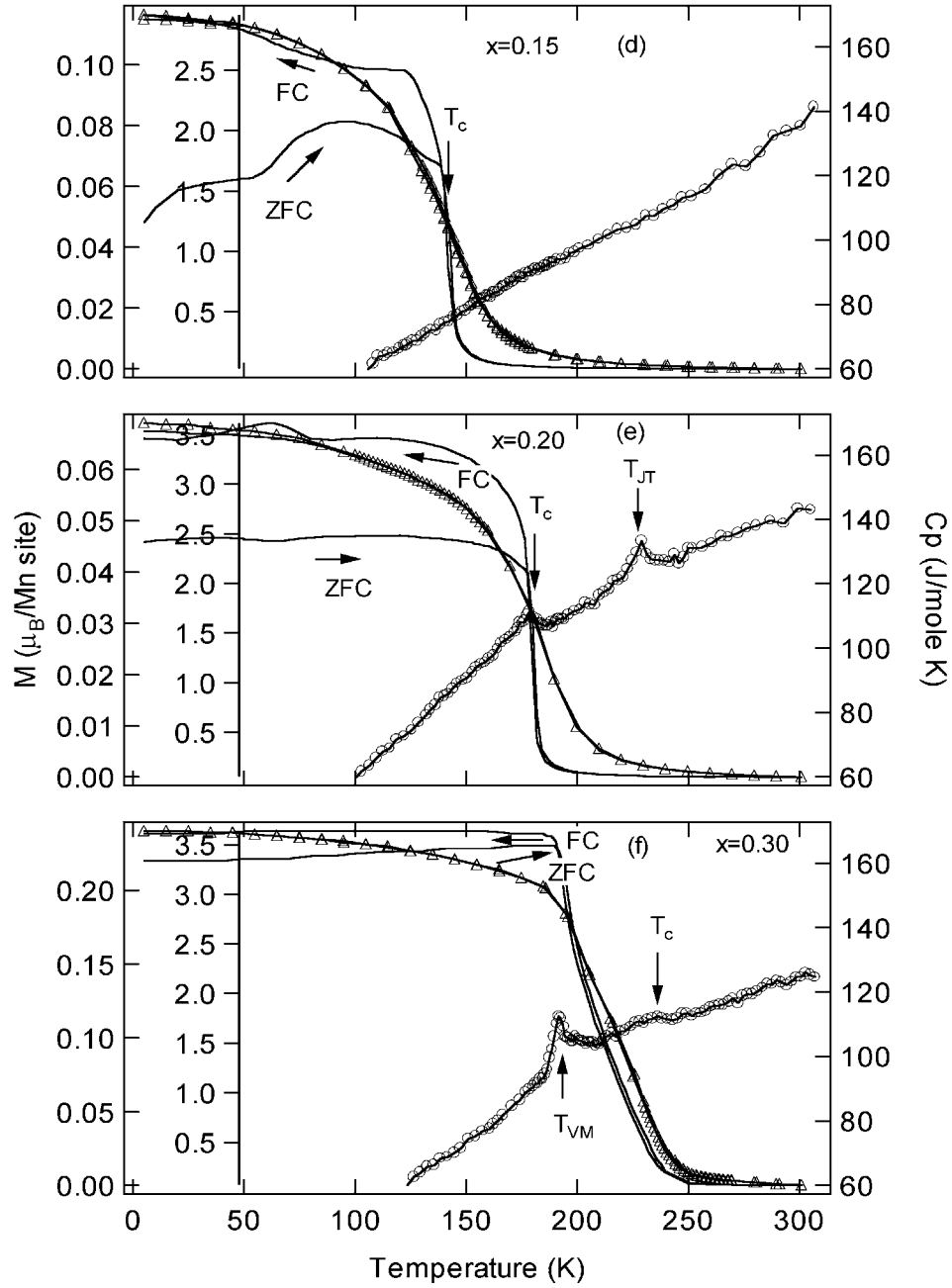


Fig. 4.5: Magnetization $M(T)$ in $H = 20$ Oe and 5 kOe; specific-heat $C_p(T)$ for $\text{La}_{1-x}\text{Ca}_x\text{MnO}_3$. $\circ = C_p(T)$, $\Delta = M(T)$ in 5 kOe; simple solid line = $M(T)$ in 20 Oe. Arrows indicate warming vs. cooling curves.

4.4 SPECIFIC-HEAT

Fig. 4.5 compares the specific-heat $C_p(T)$ with the magnetization $M(T)$ obtained in fields $H = 20$ Oe and 5 kOe either on heating after cooling in zero field (ZFC) or on cooling in the measuring field (FC). A correction for the remanent field in the SQUID magneto-meter was made to obtain $M(T)$ in a field as low as $H = 20$ Oe. The several critical temperatures of Fig. 4.1 are also marked by arrows in these figures; they correspond well with transitions indicated in $C_p(T)$ and $M(T)$ data.

For samples $x = 0.0$ and 0.05, the $C_p(T)$ data show a typical second-order anomaly at T_N , and the magnetization may be understood with a canted-spin anti-ferromagnetic model. However, $C_p(T)$ for the $x = 0.10$ sample has a suppressed entropy change at T_N and an anomaly characteristic of a higher-order transition. Considerable short-range magnetic order far above T_N and/or a freezing of the spins at T_N without much change in the long-range order is evident. A step increase in $M(T)$ on heating the ZFC sample in $H = 20$ Oe occurs at T_M .

The $C_p(T)$ data of Fig. 4.5(d) show a suppressed entropy change at the transition temperature $T_c \geq T_{oo}$ in the $x = 0.15$ sample, and the $M(T)$ data in $H = 20$ Oe are typical of a spin glass. The enhancement of $M(T)$ below 75 K in the FC data indicates the coexistence of the CAFI phase having $T_N \approx 100$ K. In $H = 5$ kOe, the spin-glass phase is transformed into a ferromagnetic phase with a Curie temperature $T_c \approx T_g$, but the CAFI phase remains unchanged to give an enhancement of $M(T)$ below 75 K. The coexistence of the CAFI phase keeps the magnetization $M(5\text{ K}, 50\text{ kOe})$, Fig. 4.3, below the theoretical spin-only value.

The data thus provide clear evidence of the coexistence of two magnetic phases, one corresponding to the CAFI matrix responsible for a spin glass in low magnetic fields and is transformed into a ferromagnetic phase in an applied field $H = 5$ kOe. The existence of a spin glass phase in the system $\text{La}_{1-x}\text{Ca}_x\text{MnO}_3$ has also been observed by other researchers by measurements of the *ac* susceptibility and the relaxation of the thermoremanent magnetization.^{4,12}

A spin glass occurs where an anti-ferromagnetic matrix ordering below its $T_N \approx T_g$ contains within it a volume of FM phase that is below its percolation limit and has a $T_c(\text{FM}) > T_g$. In the manganese-oxide perovskites, the FM phase is hole-rich, while the matrix is hole poor.^{4,13} The concentration of holes within a FM volume exceeds $x = 0.22$ in the $\text{La}_{1-x}\text{Ca}_x\text{MnO}_3$ system. Interpretation of the magnetic and transport data requires a distinction be made between what happens when a field H is applied above T_g where the samples are paramagnetic and the phase transition that occurs on application of a modest $H = 5$ kOe below T_g . At paramagnetic temperatures $T_g < T < T_c(\text{FM})$, the FM phase grows beyond its percolation threshold in a large H , and the CMR phenomenon reflects the greater conductivity of the FM phase. The application of an H below T_g , on the other hand, aligns the FM regions and induces a progressive transformation of the anti-ferromagnetic matrix of the spin glass to a ferromagnetic phase in which the holes trapped in the FM clusters become released to give a vibronic, bad-metal conductor.^{4,14}

For $x = 0.20$ and 0.30 , an anomaly in $C_p(T)$ appears at T_{JT} above T_c and at T_{VM} below T_c . Different from that of $\text{La}_{1-x}\text{Sr}_x\text{MnO}_3$, the transition at T_{JT} in La_{1-x}

$x\text{Ca}_x\text{MnO}_3$ is second order in the $C_p(T)$ curve. This observation is consistent with the resistivity result, which shows no obvious anomaly indicating a change in the character of the charge carriers at either T_{JT} or T_{VM} .

4.5 SUMMARY

Measurements of resistivity $\rho(T)$, specific-heat $C_p(T)$, magnetization $M(T)$ in applied magnetic fields $H = 20$ Oe, 5 kOe and magnetization at 5 K up to 50 kOe have confirmed the complex phase diagram below 310 K of the system $\text{La}_{1-x}\text{Ca}_x\text{MnO}_3$ in the range $0.00 \leq x \leq 0.30$ that has been deduced from magnetic and high-pressure transport data, structural experiments, and measurements made on individual samples by several groups. In the compositional range $0.075 \leq x \leq 0.22$, the electrons in σ -bonding orbitals undergo a transition from localized behavior in a canted-spin anti-ferromagnetic insulator (CAFI) with a static, cooperative Jahn-Teller orbital ordering to itinerant-electron behavior below T_c in a ferromagnetic metal (FM). We have identified the coexistence of an antiferromagnetic matrix and a FM phase with $T_c > T_N$, a spin-glass appearing in low applied magnetic fields between the CAFI and FM phases where the CMR phenomenon is found. The data allow a distinction to be made between growth in an applied field H of a FM minority phase in a paramagnetic matrix in the interval $T_g < T < T_{JT}$ and the phase transformation from a spin-glass to a ferromagnetic vibronic (FV) phase on application of an $H = 5$ kOe below $T_g \approx T_c$. The former is responsible for the CMR phenomenon; the latter represents stabilization of an orbitally disordered FV relative to an orbitally ordered anti-ferromagnetic matrix. However, both phenomena depend on the existence of ferromagnetic vibronic

superexchange interactions, which is responsible for stabilization in an applied magnetic field of an orbitally disordered ferromagnetic phase relative to an orbitally ordered phase that orders antiferromagnetically below T_N .

Chapter 5: The $R_{0.7}A_{0.3}\text{MnO}_3$ system

In the previous two chapters, the properties of the $\text{La}_{1-x}\text{Sr}_x\text{MnO}_3$ (LSMO) system and $\text{La}_{1-x}\text{Ca}_x\text{MnO}_3$ (LCMO) system were discussed. In these two systems, the hole doping level varies with the Sr or Ca concentration x . The properties of the materials experience a transition from localized to itinerant electronic behavior. This chapter reports a study of $R_{0.7}A_{0.3}\text{MnO}_3$ compounds in which A is one or two divalent alkaline earth and R is one or more of the trivalent rare earth ions (La, Pr, Nd, or Y). Although the oxidation state of the MnO_3 array remains fixed, its properties vary with the tolerance factor in a manner similar to their variation in LSMO and LCMO.

5.1 INTRODUCTION

In the $R_{0.7}A_{0.3}\text{MnO}_3$ perovskites, the Mn atoms occupy corner-shared oxygen octahedral sites of a simple cubic array and the larger $R_{0.7}A_{0.3}$ ions occupy the body center position. The Mn-3d states located in a large, empty gap between the filled O-2p bands and empty R-5d bands are hybridized with the O-2p orbitals to give 3d electron $(180^\circ - \phi)$ Mn-O-Mn interactions. The interatomic interactions between π -bonding 3d electrons of the high-spin $\text{Mn}^{4+}/\text{Mn}^{3+}$ ions are weaker than the intraatomic interactions,^{5,1} so the Mn t_{2g}^3 manifold is localized with a spin $S = 3/2$. The σ -bonding 3d electrons, on the other hand, may be localized or itinerant depending on the bending angle ϕ of the $(180^\circ - \phi)$ Mn-O-Mn bonds; the smaller the bending angle ϕ , the stronger the interatomic interactions. Below the

magnetic-ordering temperature T_c , $\text{La}_{0.7}\text{Ca}_{0.3}\text{MnO}_3$ is a metallic ferromagnet with itinerant σ^* electrons of e -orbital parentage, but decreasing the mean ionic radius of the $R_{0.7}A_{0.3}$ ions increases ϕ , and for ϕ greater than a critical value ϕ_c , the σ^* electrons become localized to a twofold-degenerate e -orbital of an Mn^{3+} : $t_{2g}^3 e_g^1$ configuration. The angle ϕ varies with the tolerance factor

$$t \equiv \langle A-O \rangle / \sqrt{2} \langle Mn-O \rangle$$

where $\langle A-O \rangle$ and $\langle Mn-O \rangle$ are the mean equilibrium bond lengths; t is a measure of the mismatch of the equilibrium bond lengths, and a $t < 1$ is accommodated by a cooperative rotation of the MnO_3 octahedra that bends the Mn-O-Mn bond angle from 180° . Substitution of the smaller Pr^{3+} for La^{3+} in the $\text{La}_{0.7-x}\text{Pr}_x\text{Ca}_{0.3}\text{MnO}_3$ was found to decrease a ferromagnetic Curie temperature T_c by nearly 175 K over the range $0 \leq x \leq 0.6$, and the colossal magnetoresistance (CMR) above T_c was found to increase as T_c decreased.^{5,2}

The tight-binding bandwidth of a narrow σ^* band varies as $W_\sigma \propto \cos \phi$, but the variation of $\cos \phi$ is too small to account for the dramatic changes found with increasing x in $\text{La}_{0.7-x}\text{Pr}_x\text{Ca}_{0.3}\text{MnO}_3$ system, Goodenough and Zhou^{5,3} have proposed that on the approach to crossover from itinerant to localized electronic behavior from the itinerant electron side, localized-electron clusters are first introduced by locally cooperative band-length fluctuations, in which case the bandwidth becomes $W = W_\sigma \exp(-\lambda \varepsilon_a / \hbar \omega_O)$, where ε_a is an activation energy to convert from one phase to the other and the frequency of the locally cooperative bond-length fluctuation $\omega_O = \omega_O(\phi)$ decreases with increasing bending angle ϕ . In order to further clarify the role of the tolerance factor in modulating the physical

properties of the MnO_3 array for a fixed oxidation state, we have expanded a large range of $\langle A-O \rangle$ by studying several additional $\text{R}_{0.7}\text{A}_{0.3}\text{MnO}_3$ compounds.

5.2 EXPERIMENTAL PROCEDURES

For this study, 8 single-crystal samples and 2 ceramic samples were grown. Table 5.1 lists the sample composition and stoichiometric mixture. Sample #1 ($\text{La}_{0.2}\text{Y}_{0.5}\text{Ca}_{0.3}\text{MnO}_3$) and sample #10 ($\text{La}_{0.7}\text{Ba}_{0.3}\text{MnO}_3$) are ceramic; all the other 8 samples are single crystals. All samples were shown to be oxygen stoichiometric by comparison of T_c with the literature values.

Table 5.1: Sample Composition and Stoichiometric Mixture for $\text{R}_{0.7}\text{A}_{0.3}\text{MnO}_3$

No.	Composition	Stoichiometric Mixture
1	$\text{La}_{0.2}\text{Y}_{0.5}\text{Ca}_{0.3}\text{MnO}_3$	La_2O_3 , Y_2O_3 , CaCO_3 , Mn_2O_3
2	$\text{Nd}_{0.7}\text{Ca}_{0.3}\text{MnO}_3$	Nd_2O_3 , CaCO_3 , Mn_2O_3
3	$\text{Nd}_{0.35}\text{Pr}_{0.35}\text{Ca}_{0.3}\text{MnO}_3$	Nd_2O_3 , Pr_6O_{11} , CaCO_3 , Mn_2O_3
4	$\text{Pr}_{0.7}\text{Ca}_{0.3}\text{MnO}_3$	Pr_6O_{11} , CaCO_3 , Mn_2O_3
5	$\text{La}_{0.5}\text{Pr}_{0.2}\text{Ca}_{0.3}\text{MnO}_3$	La_2O_3 , Pr_6O_{11} , CaCO_3 , Mn_2O_3
6	$\text{La}_{0.6}\text{Pr}_{0.1}\text{Ca}_{0.3}\text{MnO}_3$	La_2O_3 , Pr_6O_{11} , CaCO_3 , Mn_2O_3
7	$\text{La}_{0.7}\text{Ca}_{0.3}\text{MnO}_3$	La_2O_3 , CaCO_3 , Mn_2O_3

8	$\text{La}_{0.7}\text{Sr}_{0.15}\text{Ca}_{0.15}\text{MnO}_3$	La_2O_3 , SrCO_3 , CaCO_3 , Mn_2O_3
9	$\text{La}_{0.7}\text{Sr}_{0.3}\text{MnO}_3$	La_2O_3 , SrCO_3 , Mn_2O_3
10	$\text{La}_{0.7}\text{Ba}_{0.3}\text{MnO}_3$	La_2O_3 , BaCO_3 , Mn_2O_3

Crystals were grown by the floating-zone method in an IR-radiation image furnace. The polycrystalline feed rods were prepared from a stoichiometric mixture that had been calcined three times at 1050 °C with interanneal grinding. The resulting powder was pressed into a rod and sintered at 1350 °C for 24 hours. The rod could be melted congruently in a flow of air or in a flow of O_2 , depending on the composition of the samples. This process has been shown to yield oxygen-stoichiometric crystals close to the nominal composition.^{5,4} The melt-grown rods tend to contain numerous large crystals; independent measurements on single-crystal specimens showed no difference in the temperature dependence^{5,4} of the resistivity in different crystallographic directions, only a small difference in magnitude. Of interest in this study is the temperature dependence of the resistivity; it was obtained on cooling and warming by four-probe measurements made on bars cut from the melt-grown samples. The critical temperatures are more sharply defined in the melt-grown samples than in the polycrystalline samples.

The ceramic sample $\text{La}_{0.2}\text{Y}_{0.5}\text{Ca}_{0.3}\text{MnO}_3$ was prepared from a stoichiometric mixture of La_2O_3 , Y_2O_3 , CaCO_3 , and Mn_2O_3 that had been calcined three times at 1050 °C with interanneal grinding. The resulting powder was

pressed into a rod and sintered at 1350 °C for 24 hours. The rod was then cut into several slices with a thickness of 0.5 mm. For $\text{La}_{0.7}\text{Ba}_{0.3}\text{MnO}_3$, the calcine temperature and sintering temperature were 900 °C and 1200 °C, respectively, due to its low melting point.

The specific heat $C_p(T)$ was measured with the relaxation method.^{5.5} The instrument was calibrated by measuring $C_p(T)$ for sapphire and a high-quality single crystal of Fe_3O_4 . The DC magnetization was obtained with a SQUID (Quantum Design) magnetometer.

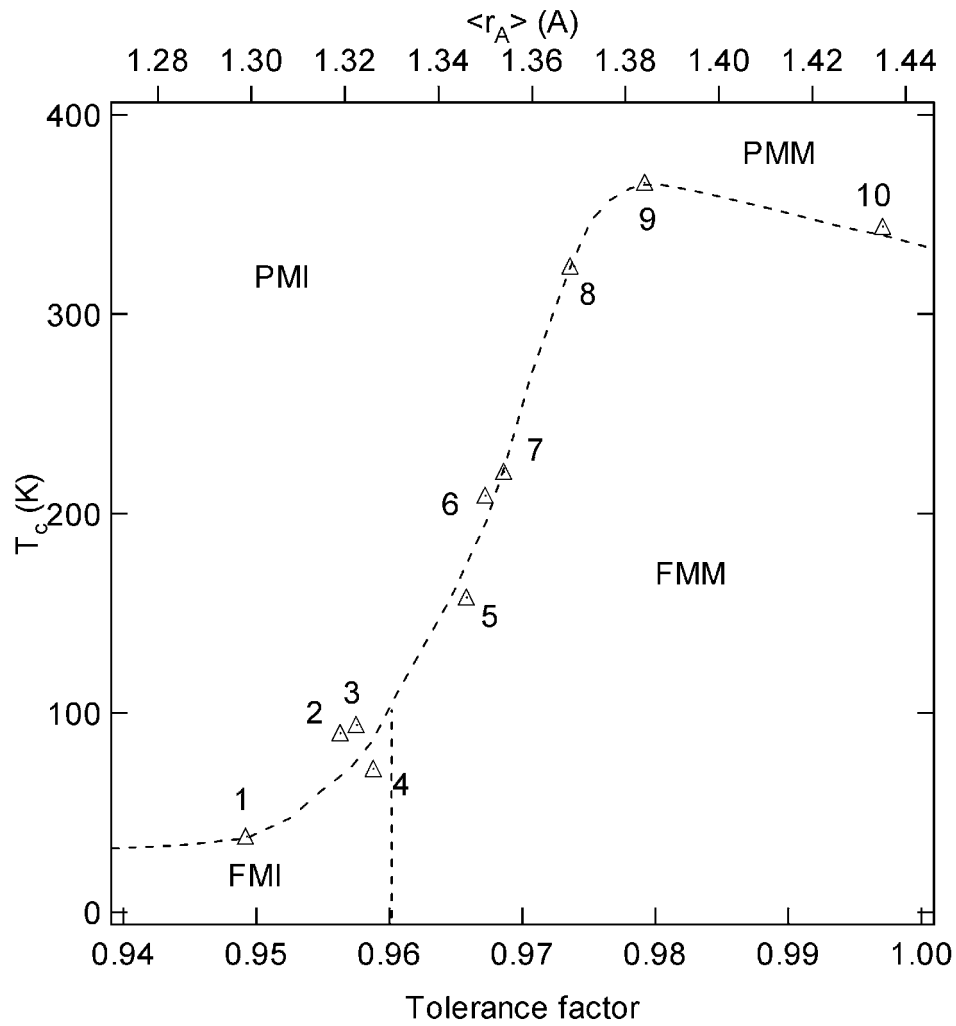


Fig. 5.1: Phase diagram of Curie temperature T_c vs. tolerance factor for the system $R_{0.7}A_{0.3}\text{MnO}_3$; R is one or more trivalent rare-earth ions such as La, Y, Nd, or Pr and A is a divalent alkaline earth ion. The T_c values are from magnetization data. The vertical line at $t = 0.96$ separates the ferromagnetic insulator and metallic (FMI and FMM) phases, as determined by resistivity measurements. Refer to Table 5.1 for sample numbers.

5.3 PHASE DIAGRAM

Fig. 5.1 shows the Curie temperature T_c vs. tolerance factor and A -site average ionic radius $\langle r_A \rangle$. In order to calculate the tolerance factor and $\langle r_A \rangle$, we use the tabulated ionic radii for 12-fold oxygen coordination of the A -site cations given by Shannon and Prewitt:^{5,6} $|La^{3+}| = 1.36 \text{ \AA}$, $|Pr^{3+}| = 1.32 \text{ \AA}$, $|Ca^{2+}| = 1.34 \text{ \AA}$, $|Mn^{3+}| = 0.645 \text{ \AA}$, $|Mn^{4+}| = 0.53 \text{ \AA}$ and $|O^{2-}| = 1.40 \text{ \AA}$. For example, the A -site average radius for $La_{0.6}Pr_{0.1}Ca_{0.3}MnO_3$ is $\langle r_A \rangle = 0.6 \times |La^{3+}| + 0.1 \times |Pr^{3+}| + 0.3 \times |Ca^{2+}| = 1.35 \text{ \AA}$; therefore the $\langle A-O \rangle$ bond length is $\langle r_A \rangle + |O^{2-}| = 2.75 \text{ \AA}$. Because the Mn^{3+}/Mn^{4+} ratio is 7/3, the $\langle Mn-O \rangle$ bond length $= 0.7 \times |Mn^{3+}| + 0.3 \times |Mn^{4+}| + |O^{2-}| = 2.01 \text{ \AA}$. The tolerance factor is $t = \langle A-O \rangle / \sqrt{2} \langle Mn-O \rangle = 2.75 / (\sqrt{2} \times 2.01) = 0.967$. The Curie temperature T_c is, from magnetization measurement, where the magnetization $M(T)$ has the maximum slope with decreasing temperature.

In this phase diagram, four principal regions are delineated: a paramagnetic insulator (PMI), a paramagnetic metal (PMM), a ferromagnetic metal (FMM), and a ferromagnetic insulator (FMI). A similar phase diagram was also obtained by Hwang *et al.*^{5,2} For $t > 0.98$, a relatively high value of T_c reflects an important ferromagnetic contribution from the dominant e_g electron double-exchange component of the Mn-O-Mn interatomic-exchange coupling between localized t^3 configurations; the weaker superexchange t^3 -O- t^3 component is anti-ferromagnetic. In the interval $0.96 < t < 0.98$, a first order transition at T_c from vibronic states to polaronic conduction occurs on heating; ferromagnetic order stabilizes double exchange coupling via extended σ^* electrons below T_c . For $t < 0.96$, the double-exchange component of the ferromagnetic coupling becomes

suppressed because the time for a polaron to hop to a neighbor is long compared to the spin-lattice relaxation time. As we have seen in the previous two chapters, the LSMO and LCMO have similar curves for T_c vs. Sr or Ca concentration x . The CMR phenomenon is found in the PMI phase above T_c in the range $0.96 \leq t \leq 0.97$.

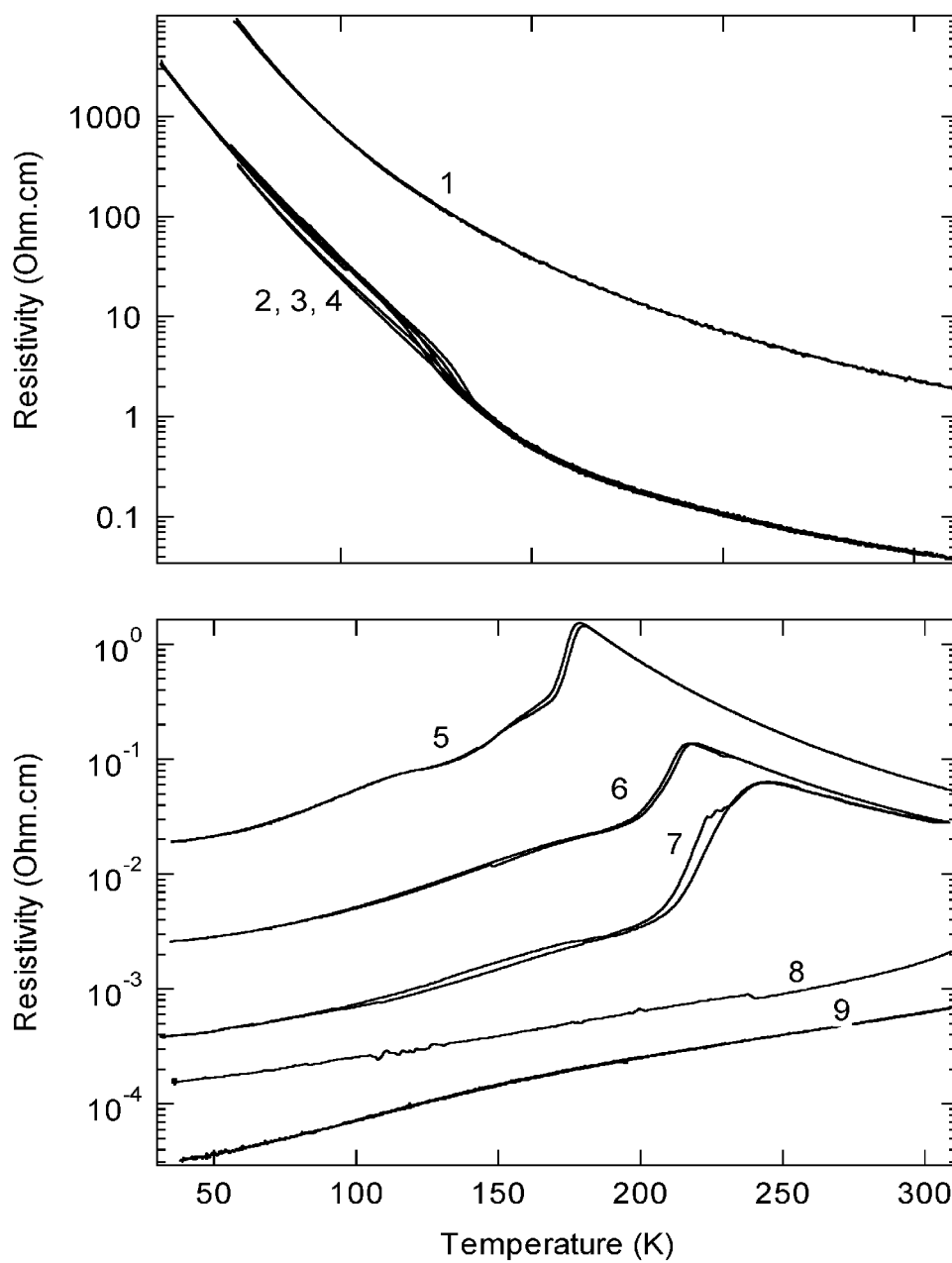


Fig. 5.2: Resistivity versus temperature for the $R_{0.7}A_{0.3}MnO_3$ system. Arrows refer to heating vs. cooling runs. Refer to Table 5.1 for sample composition.

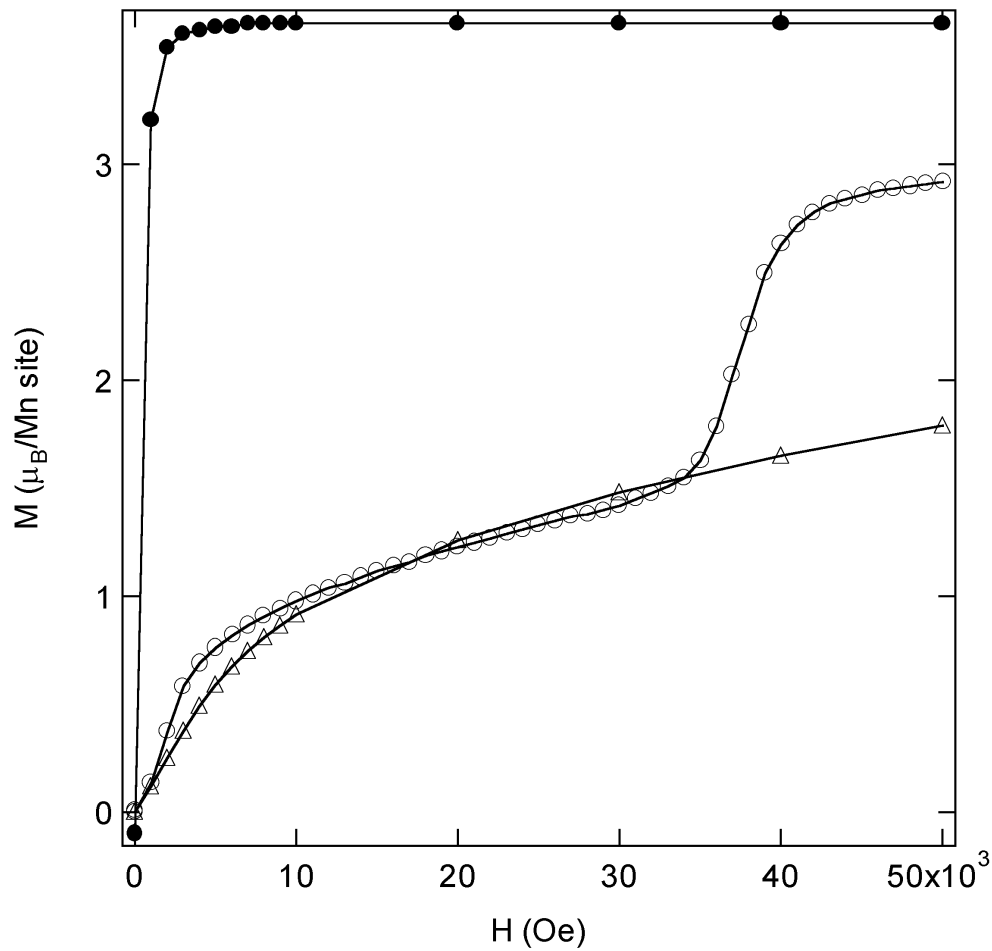


Fig. 5.3: Magnetization at 5 K versus applied field for melt-grown samples of the $\text{La}_{0.7}\text{Ca}_{0.3}\text{MnO}_3$ (solid circle), $\text{Pr}_{0.7}\text{Ca}_{0.3}\text{MnO}_3$ (open circle) and $\text{La}_{0.2}\text{Y}_{0.5}\text{Ca}_{0.3}\text{MnO}_3$ (open triangle).

5.4 RESISTIVITY AND SATURATION MAGNETIZATION

Fig. 5.2 shows the resistivity vs. temperature for several perovskites with fixed doping level, but different tolerance factors. It can be seen that sample #1 to sample #4 ($\text{La}_{0.2}\text{Y}_{0.5}\text{Ca}_{0.3}\text{MnO}_3$, $\text{Nd}_{0.7}\text{Ca}_{0.3}\text{MnO}_3$, $\text{Nd}_{0.35}\text{Pr}_{0.35}\text{Ca}_{0.3}\text{MnO}_3$,

$\text{Pr}_{0.7}\text{Ca}_{0.3}\text{MnO}_3$) are insulators over the whole temperature region. The results are consistent with previous work.^{5.2} The resistivity curves for the single-crystal samples $\text{Nd}_{0.7}\text{Ca}_{0.3}\text{MnO}_3$, $\text{Nd}_{0.35}\text{Pr}_{0.35}\text{Ca}_{0.3}\text{MnO}_3$, and $\text{Pr}_{0.7}\text{Ca}_{0.3}\text{MnO}_3$ are almost identical, indicating they have the same hole concentration. The resistivity value for $\text{La}_{0.2}\text{Y}_{0.5}\text{Ca}_{0.3}\text{MnO}_3$ is higher because this sample is a ceramic. The grain boundaries contribute to an increase of the resistivity in ceramic samples.

Sample #5 to sample #7 ($\text{La}_{0.5}\text{Pr}_{0.2}\text{Ca}_{0.3}\text{MnO}_3$, $\text{La}_{0.6}\text{Pr}_{0.1}\text{Ca}_{0.3}\text{MnO}_3$, $\text{La}_{0.7}\text{Ca}_{0.3}\text{MnO}_3$) show a transition from metallic to insulator behavior at T_c where T_c falls in the temperature range of measurement. The hysteresis shows the metallic-insulator transition is first order.^{5.2} However, the resistance change across the transition is smooth because of the coexistence of a conductive and an insulating phase across the transition with the volume fraction of the conductive phase increasing to beyond percolation in the internal molecular field on cooling through T_c . Composition #9 and #10 ($\text{La}_{0.7}\text{Sr}_{0.3}\text{MnO}_3$, $\text{La}_{0.7}\text{Ba}_{0.3}\text{MnO}_3$) show a metal-metal transition on crossing T_c .^{5.4}

Table 5.2 lists the magnetization at temperature 5 K and applied field 50 kOe. Because the $\text{Mn}^{3+}/\text{M}^{4+}$ ratio is fixed at 7/3, the theoretical value for saturated magnetization is $4 - 0.3 = 3.7 \mu_B/\text{Mn site}$. It can be seen that for most of the samples the magnetization value at 5 K and 50 kOe is close to $3.7 \mu_B/\text{Mn site}$. But there are two exceptions. One is $\text{La}_{0.2}\text{Y}_{0.5}\text{Ca}_{0.3}\text{MnO}_3$, whose value is $1.8 \mu_B/\text{Mn site}$. This value is close to that given by H. Y. Hwang *et al.*^{5.2} The other is $\text{Pr}_{0.7}\text{Ca}_{0.3}\text{MnO}_3$, which has a magnetization vs applied field curve with a pronounced step at about 35 kOe (Fig. 5.3). A similar phenomenon was also

observed in $\text{La}_{5/8-y}\text{Pr}_y\text{Ca}_{3/8}\text{MnO}_3$ with $y = 0.35$;^{5,8} the step was attributed to the inhomogeneity of the low-temperature state of this material. In fact, the step is characteristic of a spin glass.

Table 5.2: Magnetization at 5 K and 50 kOe

No.	Composition	M(5 K, 50 kOe) ($\mu_B/\text{Mn site}$)	Tolerance factor
1	$\text{La}_{0.2}\text{Y}_{0.5}\text{Ca}_{0.3}\text{MnO}_3$	1.8	0.949
2	$\text{Nd}_{0.7}\text{Ca}_{0.3}\text{MnO}_3$	3.7	0.956
3	$\text{Nd}_{0.35}\text{Pr}_{0.35}\text{Ca}_{0.3}\text{MnO}_3$	3.6	0.958
4	$\text{Pr}_{0.7}\text{Ca}_{0.3}\text{MnO}_3$	2.9	0.959
5	$\text{La}_{0.5}\text{Pr}_{0.2}\text{Ca}_{0.3}\text{MnO}_3$	3.6	0.966
6	$\text{La}_{0.6}\text{Pr}_{0.1}\text{Ca}_{0.3}\text{MnO}_3$	3.8	0.967
7	$\text{La}_{0.7}\text{Ca}_{0.3}\text{MnO}_3$	3.7	0.969
8	$\text{La}_{0.7}\text{Sr}_{0.15}\text{Ca}_{0.15}\text{MnO}_3$	3.6	0.974
9	$\text{La}_{0.7}\text{Sr}_{0.3}\text{MnO}_3$	3.7	0.979
10	$\text{La}_{0.7}\text{Ba}_{0.3}\text{MnO}_3$	3.6	0.997

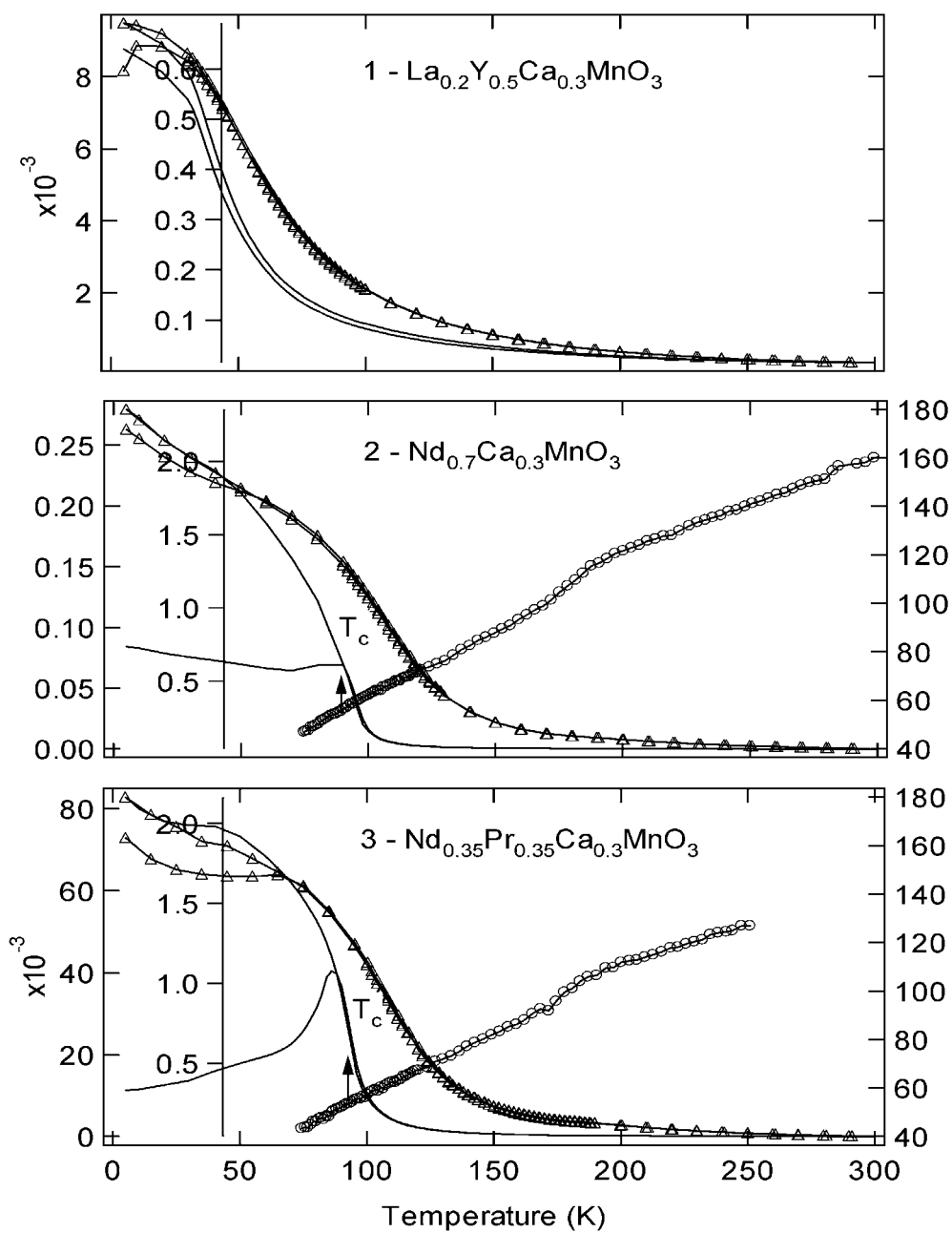


Fig. 5.4: (continued)

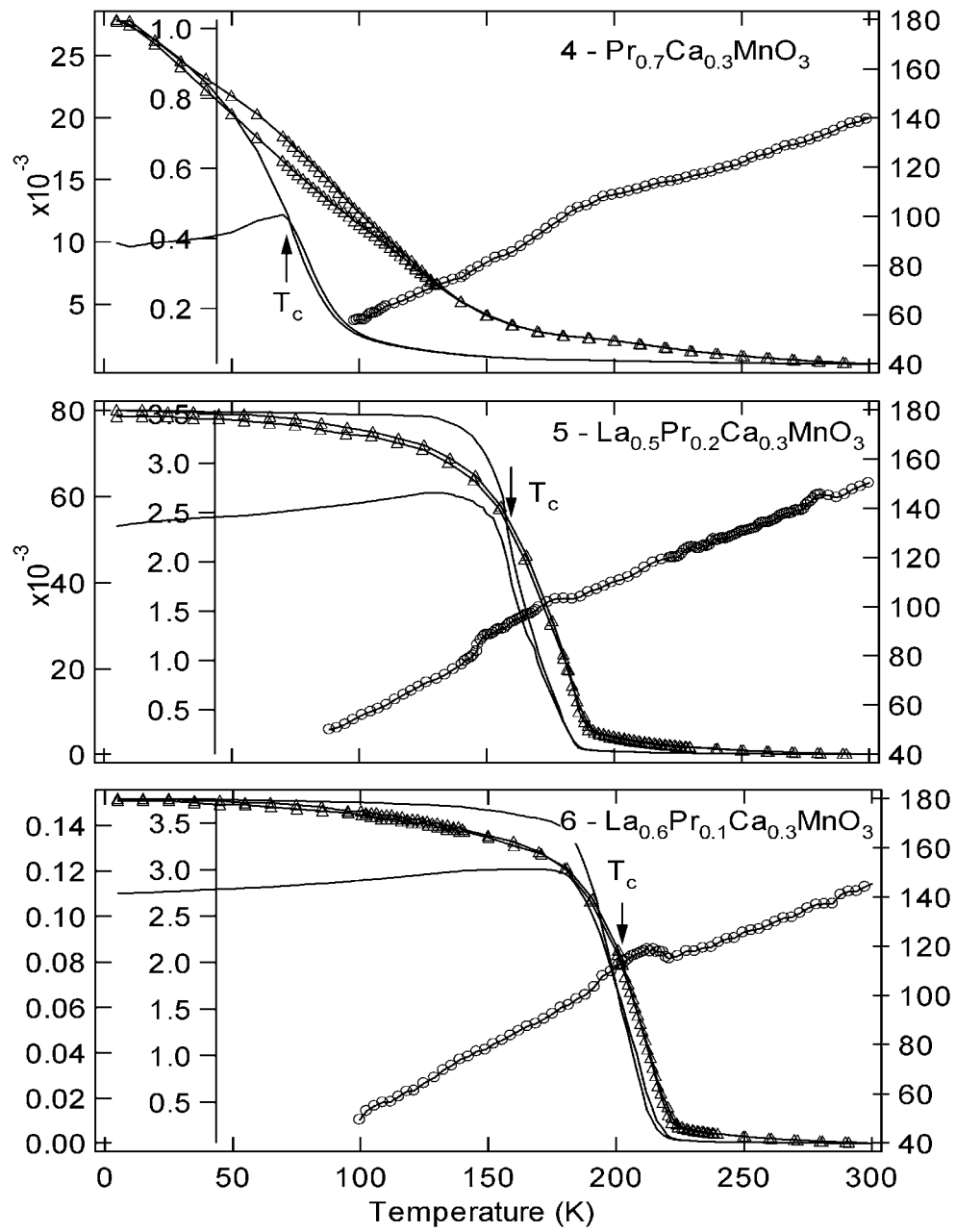


Fig. 5.4: (continued)

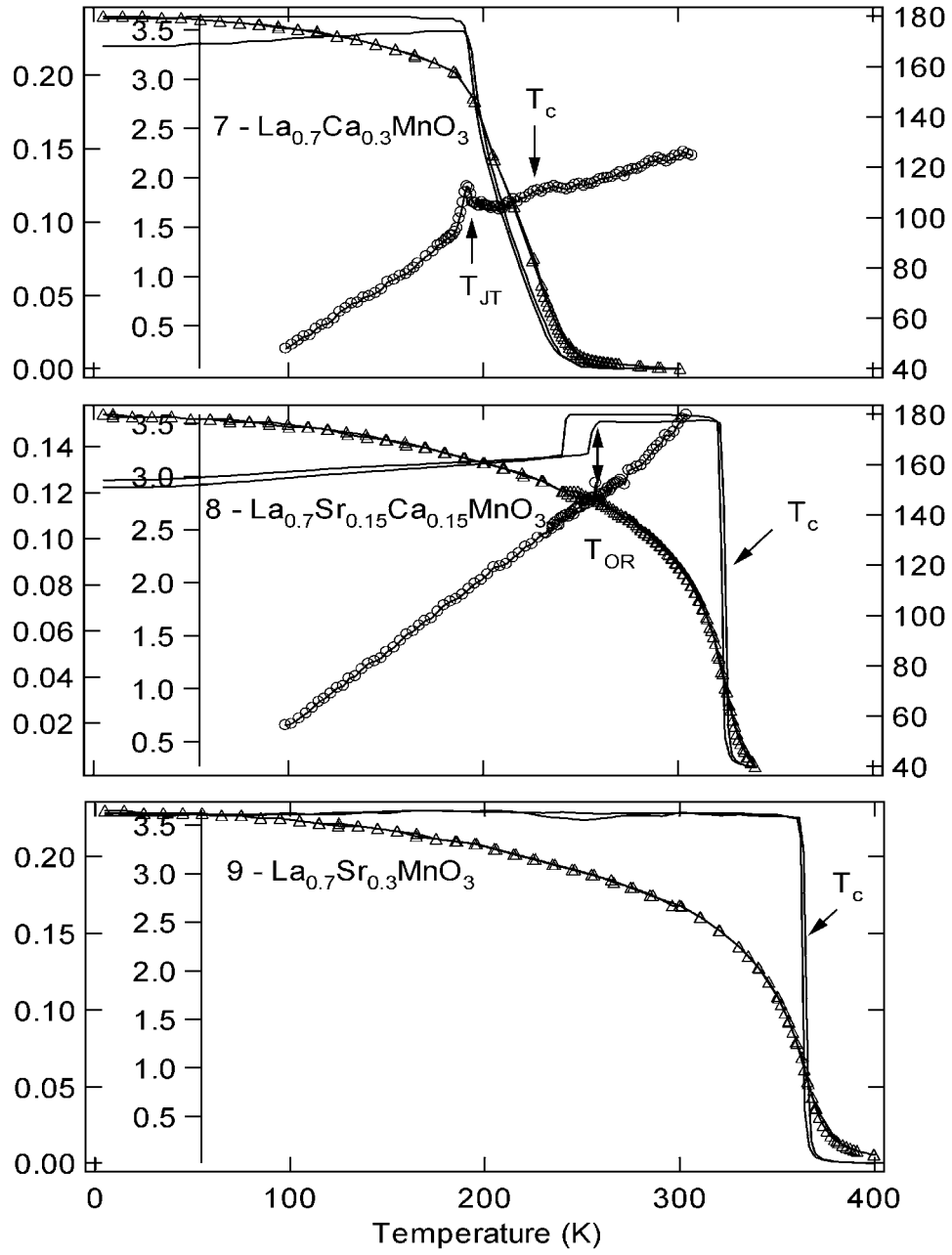


Fig. 5.4: Magnetization $M(T)$ in $H = 20$ Oe and 5 kOe; specific heat $C_p(T)$ $O = C_p$, $\Delta = M(T)$ in 5 kOe; simple solid line = $M(T)$ in 20 Oe. Arrows indicate warming vs. cooling curves.

5.5 SPECIFIC HEAT

Fig. 5.4 compares the specific heat $C_p(T)$ with the magnetization $M(T)$ obtained in fields $H = 20$ Oe and 5 kOe either on heating after cooling in zero field (ZFC) or on cooling in the measuring field (FC). A correction for the remanent field in the SQUID magnetometer was made to obtain $M(T)$ in a field as low as $H = 20$ Oe. The several critical temperatures of Fig. 5.1 are also marked by arrows in these figures.

The low magnetization $M(T)$ of sample #1 ($\text{La}_{0.2}\text{Y}_{0.5}\text{Ca}_{0.3}\text{MnO}_3$) is the ferromagnetic component of a canted-spin anti-ferromagnetism; the spin canting sets in below the Néel temperature T_N . A specific-heat measurement was not performed on this ceramic sample since ceramics generally have a poor thermal conductivity.

Samples #2 to #4 ($\text{Nd}_{0.7}\text{Ca}_{0.3}\text{MnO}_3$, $\text{Nd}_{0.35}\text{Pr}_{0.35}\text{Ca}_{0.3}\text{MnO}_3$, and $\text{Pr}_{0.7}\text{Ca}_{0.3}\text{MnO}_3$) exhibit a broad hump in the $C_p(T)$ curves above the Curie temperature T_c ; the hump reflects a small entropy change occurring well above T_c . In view of the CMR phenomenon found in these materials, it appears to reflect the Curie temperature T_c of hole-rich ferromagnetic clusters. An electron-rich, orbitally ordered paramagnetic matrix would, in this case, contain an electron-poor, orbitally disordered ferromagnetic and conductive minority phase that can grow at the expense of the orbitally ordered phase in an applied magnetic field.^{5,9} Growth beyond a percolation threshold gives the CMR phenomenon. The metamagnetic transition found in sample #4, see Fig. 5.3, suggests a growth to beyond the percolation limit. In zero applied field, a broad thermal hysteresis of the

resistivity may reflect changing volume fractions of the orbitally ordered and disordered phases.

Samples #5 ($\text{La}_{0.5}\text{Pr}_{0.2}\text{Ca}_{0.3}\text{MnO}_3$) and #6 ($\text{La}_{0.6}\text{Pr}_{0.1}\text{Ca}_{0.3}\text{MnO}_3$) become long-range ferromagnetic below a first-order transition at T_c . However, the broad anomaly in the $C_p(T)$ found at T_c does not have the typical shape of a first-order transition; it reflects the coexistence of an orbitally ordered antiferromagnetic phase and an orbitally disordered ferromagnetic phase just below T_c with the conductive ferromagnetic phase growing in the internal magnetic below T_c to beyond percolation limit. In sample #7 ($\text{La}_{0.7}\text{Ca}_{0.3}\text{MnO}_3$), on the other hand, the broad hump in the $C_p(T)$ curve near T_c is split into two features as also is the thermal hysteresis in the resistivity, Fig. 5.2. The data suggest that, in zero applied field, the compound is a “cluster glass” with an antiferromagnetic minority phase having a $T_N < T_c$ as opposed to a $T_N > T_c$ in the samples with smaller tolerance factor. In a large applied magnetic field, the antiferromagnetic minority phase is suppressed.

An O^*-R transition at $T_{OR} < T_c$ in sample #8 ($\text{La}_{0.7}\text{Sr}_{0.15}\text{Ca}_{0.15}\text{MnO}_3$) is only weakly visible in the $C_p(T)$ curve; it is more clearly marked by a drop in $M(T)$ taken at $H = 20$ Oe and in the metallic resistivity curves of Fig. 5.2. A thermal hysteresis for FC vs. ZFC $M(T)$ curves in $H = 20$ Oe signals the O^*-R transition is weakly first-order. A similar transition was found in LSMO.^{5,10}

Sample #9, LSMO, shows metallic behavior with no anomalies below T_c in $H = 5$ kOe; in zero field it has itinerant electrons of e -orbital parentage at all temperatures. Superposition of the FC and ZFC $M(T)$ curves in $H = 20$ Oe and a

constant $M(T)$ below T_c are suggestive of spin-glass behavior in low magnetic fields. Since T_c is above room temperature, the specific-heat anomaly at T_c was not measurable with my instrument.

5.6 SUMMARY

Measurements of resistivity $\rho(T)$, specific heat $Cp(T)$, magnetization $M(T)$ in applied magnetic fields $H = 20$ Oe, 5 kOe and magnetization at 5 K up to 50 kOe have confirmed the complex phase diagram below 310 K of the system $R_{0.7}A_{0.3}\text{MnO}_3$ in the tolerance factor range $0.949 \leq t \leq 0.997$ that has been deduced from magnetic and transport data made on individual samples by several groups. In the range $0.956 \leq t \leq 0.966$, the electrons undergo a transition from localized behavior in a ferromagnetic insulator (FMI) to itinerant-electron behavior below T_c in a ferromagnetic metal (FMM). We have identified a spin-glass appearing in low applied magnetic fields between the CAFI and FM phases where the CMR phenomenon is found. In an applied field H , a FM minority phase grows in a CAFI matrix. The growth is responsible to the CMR phenomenon. Similar to the composition $\text{La}_{0.82}\text{Sr}_{0.18}\text{MnO}_3$ and $\text{La}_{0.81}\text{Sr}_{0.19}\text{MnO}_3$, a transition from O^* phase to R phase is found in $\text{La}_{0.7}\text{Sr}_{0.15}\text{Ca}_{0.15}\text{MnO}_3$.

Chapter 6: Summary of the Work

In summary, the complex phase diagrams of the $\text{La}_{1-x}\text{Sr}_x\text{MnO}_3$ ($0 \leq x \leq 0.35$), $\text{La}_{1-x}\text{Ca}_x\text{MnO}_3$ ($0 \leq x \leq 0.40$), and $R_{0.7}A_{0.3}\text{MnO}_3$ ($0.949 \leq t \leq 0.997$) systems, in which R is one or more the trivalent rare earth ions, A is one or two divalent alkaline earth, and t is tolerance factor, are presented; they were mapped out with measurements of resistivity $\rho(T)$, thermoelectric power $\alpha(T)$, specific-heat $C_p(T)$, and magnetization $M(T)$ on a series of melt-grown single-crystal samples. A spin-glass behavior is identified in all of the three systems in the crossover compositions from localized to itinerant behavior of electrons of e -orbital parentage in the presence of a localized t^3 configuration with spin $S = 3/2$; the crossover compositions were shown to be characterized by an electronic phase segregation into orbitally ordered, electron-rich antiferromagnetic regions and orbitally disordered, conductive ferromagnetic regions that grow in an applied magnetic field. Particular emphasis was placed on the evolution of the specific-heat $C_p(T)$ on crossing the transition from localized to itinerant electronic behavior and the fact that $C_p(T)$ is suppressed at a spin-glass freezing temperature.

In this work, crystals were grown by the floating-zone method in a NEC infrared-ray-heating image furnace. This floating-zone method, which makes crucibles unnecessary and prevents contamination from impurities, ensures production of highly pure single crystals that can be up to 7 to 8 centimeter long and have typical radii of a half-centimeter. The single-crystal growth process,

which was after Tokura *et al*, has been shown to yield oxygen-stoichiometric crystals close to the nominal composition. *X*-ray diffraction shows that the diffraction peak is very sharp and crystal has the perovskite structure.

In this work, the specific-heat $C_p(T)$ was measured by the thermal relaxation method from around 80 K to room temperature. The measurement system was re-designed to be able to measure single-crystal samples as small as 10 ~ 20 mg. For calibration of the calorimeter, a measurement on an Fe_3O_4 single crystal was performed and the result agreed with both the literature and theoretical value.

For the system $\text{La}_{1-x}\text{Sr}_x\text{MnO}_3$ in the compositional range ($0.08 \leq x \leq 0.18$), the electrons in σ -bonding orbitals undergo a transition from localized behavior in a canted-spin antiferromagnetic insulator (CAFI) with a static, cooperative Jahn-Teller orbital ordering to itinerant-electron behavior in a ferromagnetic metal (FM). We have identified a spin-glass phase appearing in low applied magnetic fields between the CAFI and FM phase where the Colossal Magnetoresistance (CMR) phenomenon is found. As the Weiss molecular field of the ferromagnetic phase increases with T_c in the range $0.10 \leq x \leq 0.17$, the glassy character of the transition decreases. Steps in T_c occur at a first-order vibronic-itinerant electronic transition at $x = 0.15$ and at the O^*-R crystallographic phase transition at $x = 0.17$. Moreover, the orbital disorder to order transition on cooling through T_{JT} was shown to evolve from second-order to first-order as T_{JT} decreases. The magnetization M at the temperature 5 K and magnetic field $H = 50$ kOe is greater than the spin only value $(4-x) \mu_B/\text{Mn}$ in the ferromagnetic insulator

(FI) phase below the orbital-order temperature T_{oo} , reaching $4.4 \mu_B/\text{Mn}$ at $x = 0.15$, but it has the spin-only value in the FM phase. An orbital moment adds to $M(T)$ where the e electrons are localized; itinerant electrons do not contribute an orbital component to the atomic magnetic moment. A first-order transition at T_{IM} in the narrow range $0.15 \leq x \leq 0.17$ appears to be an extension of T_{JT} ; paramagnetism gives the orbital order of the O' phase below T_{JT} and ferromagnetism gives the orbital order of the O'' phase below T_{IM} . The O^*-R transition is found to be a weakly first-order.

A spin-glass behavior is also found in system $\text{La}_{1-x}\text{Ca}_x\text{MnO}_3$, in which composition $x = 0.15$ shows the most striking glassy feature at glass-transition temperature $T_g \approx T_c$. The smaller tolerance factor of the $\text{La}_{1-x}\text{Ca}_x\text{MnO}_3$ system compared to that of the $\text{La}_{1-x}\text{Sr}_x\text{MnO}_3$ retains the O^* phase at lower temperatures for all compositions and shifts the metal-insulator transition from $x \approx 0.17$ in the $\text{La}_{1-x}\text{Sr}_x\text{MnO}_3$ to $x \approx 0.22$ in $\text{La}_{1-x}\text{Ca}_x\text{MnO}_3$. Moreover, the two-phase character of the CAFI+FI in the range $0.10 \leq x \leq 0.20$ prevents identification of an orbital contribution to the magnetization in the FI phase of $\text{La}_{1-x}\text{Ca}_x\text{MnO}_3$ in which the saturation magnetization has a spin-only value of $(4-x) \mu_B/\text{Mn}$.

Although the doping level is kept the same in the $R_{0.7}A_{0.3}\text{MnO}_3$ composition, the tolerance factor t is varied over the range $0.949 \leq t \leq 0.997$. For this family, the phase diagram of Curie temperature T_c vs tolerance factor t is similar to the T_c vs x diagram in $\text{La}_{1-x}\text{Sr}_x\text{MnO}_3$ and $\text{La}_{1-x}\text{Ca}_x\text{MnO}_3$. Spin-glass behavior is found in several samples of this system, reflecting hole-rich ferromagnetic clusters in electron-rich paramagnetic matrix. An O^*-R transition is

observed in $\text{La}_{0.7}\text{Sr}_{0.15}\text{Ca}_{0.15}\text{MnO}_3$ compound. A step in the $\text{Pr}_{0.7}\text{Ca}_{0.3}\text{MnO}_3$ magnetization curve comes from the inhomogeneity of the low-temperature state of this material.

REFERENCES

- 1.1 H. Y. Hwang, S-W. Cheong, P. G. Radaelli, M. Marezio, and Batlogg, *Phy. Rev. Lett.* **75**, 914 (1995).
- 1.2 B. W. Brown, E. Banks, *Phys. Rev.* **84**, 609 (1951).
- 1.3 Jonker GH, Santen JH van, *Physica* **16**, 337 (1950).
- 1.4 Jonker GH, Santen JH van, *Physica* **19**, 120 (1953).
- 1.5 P. W. Anderson, *Phys. Rev.* **115**, 2 (1959).
- 1.6 W. C. Koehler, E. O. Wollan, *J. Phys. Chm. Solids* **2**, 100 (1957); W. C. Koehler, E. O. Wollan, M. K. Wilkinson, *Phys. Rev.* **118**, 58 (1960).
- 1.7 E. O. Wollan, W. C. Koehler, *Phys. Rev.* **100**, 545 (1955).
- 1.8 J. B. Goodenough, *Phys. Rev.* **100**, 564 (1955).
- 1.9 J. B. Goodenough, in *Magnetism and the chemical bond*, (Wiley Interscience, New York, 1961).
- 1.10 C. Zener, *Phys. Rev.* **82**, 403 (1951).
- 1.11 P-G de Gennes, *Phys. Rev.* **118**, 141 (1960).
- 1.12 P. W. Anderson, H. Hasegawa, *Phys. Rev.* **100**, 675 (1955).
- 1.13 J. B. Goodenough, *Mat. Res. Bull.* **6**, 967 (1971).
- 1.14 J. B. Goodenough, *Buul. Soc. Chem. France*, No. **4**, 1200 (1965).
- 1.15 J. B. Goodenough, *Progress in Solid State Chemistry* **5**, 145 (1972).
- 1.16 J. E. Bednorz, K. A. Müller, *Z. Physik B* **64**, 189 (1986).
- 1.17 J. B. Goodenough, International Workshop on the Colossal Magnetoresistance (CMR) Effect, Melbourne, Australia, 8-11 June 1998.

- 1.18 J. B. Goodenough, J. A. Kafalas, J. M. Longo, in *Preparative methods in solid state chemistry*, edited by P. Hagenmuller, (Academic Press, New York, 1972).
- 1.19 J. Rodriguez-Carvajal, M. Hennion, F. Moussa, A. H. Moudden, L.. Pinsard, A. Revcolevschi, Phys. Rev. B **57**, R3189 (1998).
- 1.20 Y. Murakami, J. P. Hill, D. Gibbs, M. Blume, I. Koyama, M. Tanaka, H. Kawato, T. Arima, K. Hirota, Y. Endoh, Phys. Rev. Lett. **81**, 582 (1998).
- 1.21 J. E. Dzialoshinskii, J. Phys. Chem. Solids **4**, 214 (1958).
- 1.22 H. Kawano, R. Kajimoto, M. Kubota, and H. Yoshizawa, Phys. Rev. B **53**, 2202 (1996).
- 1.23 P. G. Radaelli, D. E. Cox, M. Marezio, and S-W. Cheong, Phys. Rev. B **55**, 3015 (1997).
- 1.24 S. Mori, C. H. Chen, S-W. Cheong, Phys. Rev. Lett. **81**, 3972 (1998).
- 1.25 S. Mori, C. H. Chen, S-W. Cheong, Nature **392**, 473 (1998).
- 1.26 A. Moreo, S. Yunoki, E. Dagotto, Science **283**, 2034 (1999).

- 2.1 T. H. K. Barron, G. K. White, in *Heat Capacity and Thermal Expansion at Low Temperatures*, (Kluwer Academic/Plenum Publishers, 1999, New York).
- 2.2 E. Gmelin, Thermochemica Acta **110**, 183 (1987).
- 2.3 P. F. Sullivan, G. Seidel, Phys. Rev. **173**, 679 (1968).
- 2.4 D. Djurek, J. Baturic-Rubcic, and K. Franulovic, Phys. Rev. Lett. **33**, 1126 (1974); H. Yao, K. Ema, C. W. Garland, Rev. Sci. Instrum. **69** (1), 172 (1998).
- 2.5 A. Kozlowski, Z. Kakol, D. Kim, R. Zalecki, and J. M. Honig, Phys. Rev. B **54**, 12093 (1996).
- 2.6 J. P. Shepherd, J. W. Koenitzer, R. Aragon, J. Spalek, and J. M. Honig, Phys. Rev. B **43**, 8461 (1991).

- 2.7 H. C. Montgomery, J. App. Phys. **42**, 2971 (1971).
- 2.8 B. F. Logan, S. O. Rice, and R. F. Wick, J. App. Phys. **42**, 2875 (1971).
- 2.9 J. C. Gallop, in *SQUIDS, the Josephson Effects and Superconducting Electronics*, (Adam Hilger, 1991, New York)

- 3.1 J.-S. Zhou and J. B. Goodenough, Phys. Rev. B 60, R15002 (1999).
- 3.2 J. B. Goodenough, Phys. Rev. 100, 564 (1955).
- 3.3 E. F. Bertaut, in Magnetism: A Treatise on Modern Theory and Materials, edited by G. T. Rado and H. Suhl (Academic Press, New York, 1963), Chap. 4.
- 3.4 K. Kumagai, A. Iwai, Y. Tamioka, H. Kuwahara, Y. Tokura, A. Yakubovskii, Phys. Rev. B **59**, 97 (1999).
- 3.5 J.-S. Zhou, J. B. Goodenough, Phys. Rev. B 62, 3834 (2000); J.-S. Zhou, G.-L. Liu, J. B. Goodenough, *ibid.* 63, 172416 (2001).
- 3.6 B. Dabrowski, X. Xiong, Z. Bukowski, R. Dybziński, P. W. Klamut, J. E. Siewenie, O. Chmaissem, J. Shaffer, C. W. Kimball, J. D. Jorgensen, and S. Short, Phys. Rev. B 60, 7006 (1999).
- 3.7 A. Urushibara, Y. Moritomo, T. Arima, A. Asamitsu, G. Kido, and Y. Tokura, Phys. Rev. B 51, 14103 (1995).
- 3.8 S. Jin, T. H. Tiefel, M. McCormack, R. A. Fastnacht, R. Ramesh, and L. H. Chen, Science 264, 413 (1994).
- 3.9 E. Dagotto, S. Yunoki, A. L. Malvezzi, A. Moreo, J. Hu, S. Capponi, D. Poilblanc, and N. Furukawa, Phys. Rev. B 58, 6414 (1998); J. B. Goodenough, Aust. J. Phys. 52, 155 (1999).
- 3.10 M. J. Rozenberg, G. Kotliar, and X. Y. Zhang, Phys. Rev. B 49, 10 181 (1994).
- 3.11 Y. Moritomo, A. Asamitsu, and Y. Tokura, Phys. Rev. B 51, 16491 (1995).

- 3.12 G. R. Stewart, Rev. Sci. Instrum. 54, 1 (1983).
- 3.13 T. Okuda, A. Asamitsu, Y. Tomioka, T. Kimura, Y. Taguchi, and Y. Tokura, Phys. Rev. Lett. 81, 3203 (1998).
- 3.14 P.-G. de Gennes, Phys. Rev. 118, 141 (1960).
- 3.15 J. B. Goodenough, A. Wold, R. J. Arnett, and N. Menyuk, Phys. Rev. 124, 373 (1961); J.-S. Zhou, H.-Q. Yin, and J. B. Goodenough, Phys. Rev. B 63, 184423 (2001).
- 3.16 S. Uhlenbruck, R. Teipen, R. Kingeler, B. Buchner, O. Friedt, M. Hucker, H. Kierspel, T. Niemoller, L. Pinsard, A. Revcolevschi, and R. Gross, Phys. Rev. Lett. 82, 185 (1999).
- 3.17 M. R. Lees, O. A. Petrenko, G. Balakrishnan, and D. Mck. Paul, Phys. Rev. B 59, 1298 (1999).
- 4.1 P. Schiffer, A. P. Ramirez, W. Bao, and S.-W. Cheong, Phys. Rev. Lett. 75, 3336 (1995).
- 4.2 F. Moussa, M. Hennion, G. Biotteau, and J. Rodriguez-Carvajal., Phys. Rev. B 60, 12299 (1999).
- 4.3 G. Biotteau, M. Hennion, F. Moussa, J. Rodriguez-Carvajal, L. Pinsard, A. Revcolevschi, Y. M. Mukovskii, and D. Shulyatev, Phys. Rev. B 64, 104421 (2001).
- 4.4 Chang Seop Hong , Wan Seop Kim, and Nam Hwi Hur, Phys. Rev. B 63, 92504 (2001).
- 4.5 J. B. Goodenough, in *Localized to Itinerant Electronic Transition in Perovskite Oxides*, Springer-Verlag, Berlin Heidelberg 2001.
- 4.6 V. Markovich, E. Rozenberg, A. I. Shames, G. Gorodetsky, I. Fita, K. Suzuki, R. Puzniak, D. A. Shulyatev, and Ya. M. Mukovskii, Phys. Rev. B 65, 144402 (2001).
- 4.7 T. Okuda, Y. Tomioka, A. Asamitsu, and Y. Tokura, Phys. Rev. B 61, 8009 (2000).

- 4.8 Pengcheng Dai, J. A. Fernandez-Baca, N. Wakabayashi, E. W. Plummer, Y. Tomioka, and Y. Tokura, Phys. Rev. Lett. **85**, 2553 (2000).
- 4.9 Guo-meng Zhao, H. Keller, W. Prellier, and D. J. Kang, Phys. Rev. B **63**, 172411 (2001).
- 4.10 J.-S. Zhou, J. B. Goodenough, A. Asamitsu, and Y. Tokura, Phys. Rev. Lett. **79**, 3234 (1997).
- 4.11 G.-L. Liu, J.-S. Zhou, and J. B. Goodeough., Phys. Rev. B **64**, 144414 (2001).
- 4.12 R. Laiho, E. Lahderanta, J. Salminen, K. G. Lisunov, and V. S. Zakhvalinskii, Phys. Rev. B **63**, 94405 (2001).
- 4.13 J. B. Goodenough, International Workshop on the Colossal Magnetoresistance (CMR) Effect, Melbourne, Australia, 8-11 June 1998.
- 4.14 J.-S. Zhou, and J. B. Goodeough., Phys. Rev. B **62**, 3834 (2000).

- 5.1 J. B. Goodenough and J. M. Longo, *Landolt-Börnstein Tabellen* (Springer, Berlin, 1970). Vol. III/4a.
- 5.2 H. Y. Hwang, S-W. Cheong, P. G. Radaelli, M. Marezio, and Batlogg, Phy. Rev. Lett. **75**, 914 (1995).
- 5.3 J. B. Goodenough, J.-S. Zhou, Mat. Res. Soc. Symp. Proc. **494**, 335 (1998).
- 5.4 A. Urushibara, Y. Moritomo, T. Arima, A. Asamitsu, G. Kido, and Y. Tokura, Phys. Rev. B **51**, 14103 (1995).
- 5.5 G. R. Stewart, Rev. Sci. Instrum. **54**, 1 (1983).
- 5.6 R. D. Shannon and C. T. Prewitt, Acta Crystallogr. B **25**, 725 (1969); **26**, 1046 (1970).
- 5.7 W. Archibald, J.-S. Zhou, and J. B. Goodenough., Phys. Rev. B **53**, 14445 (1996).

- 5.8 V. Kiryukhin, B. G. Kim, V. Podzorov, S.-W. Cheong, T. Y. Koo, J. P. Hill, I. Moon, and Y. H. Jeong., Phys. Rev. B **63**, 24420 (2000).
- 5.9 J.-S. Zhou, H. Q. Yin, and J. B. Goodenough, Phys. Rev. B **63**, 184423 (2001).
- 5.10 G.-L. Liu, J.-S. Zhou, and J. B. Goodenough., Phys. Rev. B **64**, 144414 (2001).

Vita

Guoliang Liu was born to Jiying Wang and Yongyuan Liu on November 11, 1970 in Linqing, Shangdong Province, People's Republic of China. He attended the 1st Elementary School, the 1st Middle School, and the 1st High School, all in Linqing. Upon graduation, he pursued studies in Physics at Peking University and obtained a BS Degree in 1992 and MS Degree in 1996. From July 1992 to September 1993, he was employed as Research Associate in the Department of Physics, Peking University. He began to pursue graduate studies in Physics in 1996 at the University of Texas at Austin and switched to Electrical Engineering in 1997. He was awarded Master of Science in Engineering Degree in 2000. In April 2001, he began employment with Dallas Semiconductor – Maxim Integration Products, Inc. as an electrical engineer. During this time, he worked on the write-up of his dissertation for the Ph. D. Degree in Electrical Engineering at the University of Texas, Austin.

Permanent Address: 11 Nan Wei Zi Street, Apt. #302, Jinan, Shandong 250011,
People's Republic of China

This dissertation was typed by the author.